UNIVERSIDADE DE SÃO PAULO
INSTITUTO DE FÍSICA DE SÃO CARLOS

PAULA MARIA PINCELA LINS

Cell-derived nanoplatforms for cancer therapy

São Carlos
2021

PAULA MARIA PINCELA LINS

Cell-derived nanoplatforms for cancer therapy

Thesis presented to the Graduate Program in Physics at the Instituto de Física de São Carlos, Universidade de São Paulo to obtain the degree of Doctor of Science.

Concentration area: Applied Physics
Option: Biomolecular Physics
Advisor: Prof. Dr. Valtencir Zucolotto

Original version

São Carlos
2021

Lins, Paula Maria Pincela
Cell-derived nanoplatforms for cancer therapy / Paula Maria Pincela Lins; advisor Valtencir Zucolotto -- São Carlos 2021.
127 p.

Thesis (Doctorate - Graduate Program in Biomolecular Physics) -- Instituto de Física de São Carlos, Universidade de São Paulo - Brasil , 2021.

1. Cell-derived. 2. Nanomaterials. 3. Cancer therapy. I. Zucolotto, Valtencir, advisor. II. Title.

FOLHA DE APROVAÇÃO

Paula Maria Pincela Lins

Tese apresentada ao Instituto de Física de São Carlos da Universidade de São Paulo para obtenção do título de Doutora em Ciências. Área de Concentração: Física Aplicada - Opção: Física Biomolecular.

Aprovado(a) em: 26/03/2021

Comissão Julgadora

Dr(a). Valtencir Zucolotto

Instituição: (IFSC/USP)

Dr(a). Elson Longo da Silva

Instituição: (UFSCar/São Carlos)

Dr(a). Natalia Mayumi Inada

Instituição: (IFSC/USP)

Dr(a). Maria Vitoria Lopes Badra Bentley

Instituição: (FCFRP/USP)

Dr(a). Leticia Gomes de Pontes

Instituição: (ICB/USP)

With love,
to my families from blood and heart.

ACKNOWLEDGEMENTS

To my mother, Andrea, I have no words to describe your continuous support and providing me the best even in hard conditions.

To my father, Mario, if it wasn't for your support in providing the best and teaching me math and physics, I wouldn't enjoy science and graduate in Biomolecular Physics.

To my father, Luiz thank you for your guidance, wisdom words and always teaching me that what I need is not always what I think I deserve.

To my grandparents, Cida, Mocinha e Antonio, for all your love, prays and wisdom.

To my long distant family, Alexia, Barbara, David, Téo, Talma, Pedro, André and Guilherme for understanding my distance during these years living in São Carlos.

To my family from heart in São Carlos, Edson, Rejane, Laura, Marina and Vitor that taught me that life is not only work. In particular to Laura my best friend who always were there in the tough times and for giving me that ride to the lab in the middle of the night to see cells. Thank you.

To my boyfriend Alessandro who always takes such good care of me and even not understanding about nanorods helped me revising my presentations. Indeed, your patience and kindness are not measured in the nanoscale.

I would like to thank my supervisor Zucolotto for all the thrust and freedom you gave through those many years, and for understanding my personal difficulties and always helping.

I would deeply thank Juliana for guiding my first steps in the lab and for revising this thesis.

I deeply acknowledge Valeria for your tremendous help with the gold nanorods synthesis and always helping me even very busy.

I thank Silvana and Marco for providing the best food of São Carlos when I did not have the time to make food for myself between experiments.

I thank Soph and Rafa for your support during the pandemics always exchanging good food and masked talks.

A special thank for Laís friendship and support through those years. Your help was essential to the development of the thesis, from our lunches with Sophia Loren dish, to discussing articles.

I thank Chata for always pushing me to the boundaries of science and adding me in innovative projects from Rubberbye to cigarette filters supercapacitors.

I thank my friends from AdS that did not give up on me and always called me to the Halloweens and gameplays.

To all the members of the Nanomedicine and Nanotoxicology Group (GNano): Bianca, Luana, Edson, Lais Brazaca, Jaque (Pedro), Idelma, Nirton, Fran (Martin), Helena, Adrislaine, Leo, Marco, Renata, and a more special thank you for Bruna, Simone and Romeu for all your support.

A warm thank to Cris, Isa and Olavo for always being such great colleagues and providing the best laughs in the lab.

I acknowledge the Laboratório Nacional de Nanotecnologia – LNNano for the training and possibility to use the Transmission Electron Microscopy many times during the PhD.

I thank Fundação de Amparo a Pesquisa do Estado de São Paulo (FAPESP) for the fellowship during the PhD (2017/21869-6 and 2016/00971-4).

I thank CnpQ for the fellowship during the beginning of PhD (133317/2016-1).

Finally, I would like to express my deep gratitude to all people that have contributed direct or indirectly to my personal and professional development.

“Let universities be playgrounds for the youth.”
Bernard Feringa

ABSTRACT

LINS, P. M. P. **Cell-derived nanoplatforms for cancer therapy.** 2021. 127 p. Thesis (Doctor in Science) - Instituto de Física de São Carlos, Universidade de São Paulo, São Carlos, 2021.

Nanomaterials are promising platforms for cancer therapy due to their innate passive targeting. The success of nanomaterials into the clinics depends on their blood circulation time and accumulation in the target tissue, factors related with their ability to evade the immune system. Cell-derived nanoplatforms are an emerging technology to enhance the delivery by active targeting the tumor site, without the perks of chemical conjugations. In this thesis we report the development of biomimetic novel platforms using the cell-derived technology and their *in vitro* interaction in cells from tumor microenvironment. To understand of the cell-derived nanoplatforms, two different nanomaterials were synthesized and further coated with extracellular vesicles and cell membrane extract from two different cell lines. First, gold nanorods (AuNRs) were coated with two macrophage derived vesicles, cell membrane extract and extracellular vesicles. Cell membrane-coated AuNRs interacted more with the metastatic cancer cells and the extracellular vesicles interacted more with the source cells. The main difference evaluated among the coatings was the presence of the tetraspanin CD47, an immunosuppressive marker for phagocytosis. Furthermore, we developed a paclitaxel-loaded polymeric nanoparticle carrier coated with metastatic breast cancer cell membrane. All cell lines showed a preferential uptake for the nanoparticles coated with the cell membrane, with stronger interaction with the source cell and the fibroblasts. Our results pointed to the role of adhesion molecules in the homotypic bind to cancer cells and the interaction with stroma cells as a heritage of the tumor progression pathways. As a consequence of the enhanced interaction of the nanocarriers with fibroblasts, the nanoparticles were significantly cytotoxic. We also explored the tunability of the plasmonic band in relation to their composition and size and evaluated basic culture parameters for extracellular vesicles isolation by means of size distribution and concentration.

Keywords: Cell-derived. Nanomaterials. Cancer therapy.

RESUMO

LINS, P. M. P. **Nanoplataformas derivadas de células para o tratamento de câncer.** 2021. 127 p. Tese (Doutorado em Ciências) - Instituto de Física de São Carlos, Universidade de São Paulo, São Carlos, 2021.

Os nanomateriais são plataformas promissoras para a terapia do câncer devido ao seu inato acúmulo passivo em tumores. O sucesso dos mesmos na clinica depende do seu tempo dentro da circulação sanguínea e da sua acumulação no tecido alvo, fatores relacionados com a capacidade de escapar ao sistema imunológico. As nanoplataformas derivadas de células são uma tecnologia emergente para melhorar estas propriedades através do acúmulo ativo no local do tumor. Nesta tese relatamos o desenvolvimento de plataformas biomiméticas inovadoras avaliando suas interações *in vitro* em células modelo do microambiente tumoral. Para compreendermos melhor as nanoplataformas derivadas de células, dois nanomateriais diferentes foram sintetizados e posteriormente revestidos. Inicialmente, os *nanorods* de ouro (AuNRs) foram revestidos com duas vesículas derivadas de macrófagos, vesículas de membrana celular e vesículas extracelulares. Os AuNRs revestidos de membrana celular interagiram mais com a linha celular metastática de câncer e as vesículas extracelulares interagiram com a célula de origem (macrofágos). A principal diferença avaliada entre os revestimentos foi a presença da tetraspanina CD47, imunossupressor para a fagocitose. Além disso, desenvolvemos nanopartículas poliméricas com paclitaxel, revestidas com membrana celular metastática de câncer da mama. Todas as linhagens celulares mostraram uma interação preferencial para as nanopartículas revestidas com membrana celular, tendo uma interação mais pronunciada com a célula de origem e os fibroblastos. Este resultado indica o papel das moléculas de adesão nas interações homotípicas das nanopartículas às células cancerosas, além da herança da interação da célula tumoral com as células do estroma para a progressão do tumor. Como consequência, para uma maior interação com os fibroblastos, as nanopartículas foram significativamente citotóxicas. Os resultados da tese mostram como estas novas classes de nanomateriais são desenvolvidas e as suas interações com o microambiente tumoral. Além disso, estudamos mudanças na banda plasmonica dos *nanorods* de ouro em relação à sua composição e tamanho. Por fim,

avaliamos os parâmetros de isolamento das vesículas extracelulares por distribuição de tamanho e concentração.

Palavras-chave: Nanoplataformas. Derivado de células. Tratamento de câncer.

LIST OF FIGURES

LIST OF ABREVIATIONS

ANXA2	annexin 2
ATCC	American Type Culture Collection
AuNRs	gold nanorods
BCRJ	Bank Cell Rio de Janeiro
BSA	bovine serum albumin
CAF	cancer activated fibroblasts
CD47	integrin associated protein
CTAB	cetyltrimethylammonium bromide
DAPI	4',6-diamidino-2-phenylindole dihydrochloride
DiO	3,3-Dioctadecyloxacarbocyanine perchlorate
DLS	dynamic light scattering
DMEM	Dulbecco's Modified Eagle Medium
DMSO	dimethyl sulfoxide
ECM	extracellular matrix
EGF	epidermal growth factor
EpCAM	epithelial adhesion molecule
EPR	enhanced permeability and retention effect
EVs	extracellular vesicles
FBS	fetal bovine serum
FDA	Food and Drug Administration
FE-SEM	field-emission scanning electron microscopy
FLOT1	flotillin 1
FTIR	fourier-transform infrared spectroscopy
HS	horse serum
ICP-MS	inductively coupled plasma mass spectrometry
LSPR	localized surface plasmon resonance
MEBM	Mammary Epithelial Cell Growth Basal Medium
MEGM	MamMammary Epithelial Cell Growth Medium SingleQuots Kit
MTT	3-(4,5-dimethylthiazol-2yl)-2,5-diphenyl tetrazolium bromide
NCs	nanocarriers
NIR	near infrared

NTA	nanotracking analysis
PBS	phosphate buffer saline
PdI	polydispersity index
PEG	polyethylene glycol
PFA	paraformaldehyd
PLGA	poly lactic-co-glycolic acid
PTT	plasmonic photothermic therapy
PTX	paclitaxel
ROS	reactive oxygen species
SEM	scanning electron microscopy
SIRPα	signal regulatory protein α
TAMs	tumor associated-macrophages
TEM	transmission electron microscopy
TGF	tumor growth factors
TME	tumor microenvironment
TNF-α	tumor necrosis factor-α
TPL	two-photon luminescence
UV-Vis	ultraviolet-visivel
VEGF	vascular endothelial growth factor

CONTENTS

1 INTRODUCTION

For almost a century, cancer was considered a monocellular disease, and broad treatment strategies were developed according to this concept.[1] However, cancer mortality rates continued rising, and the established treatments showed to be non-effectives.[2-3] The spread of cells from the primary tumor to distant sites, defined as metastasis, is the major contributor to deaths from cancer.[4] Stephen Paget presented in 1889 that metastasis depended on the 'seeds and soil' hypothesis, where cancer cells (the 'seeds') only blooms on distant sites when in a favorable organ microenvironment (the 'soil').[5] Although an appealing analogy, it was discredited latter by the hypothesis that metastasis was purely a mechanical result from the vascular system.[6]

Recent findings have revisited the 'seed and soil' hypothesis, and novel concepts have been established.[4] As an example, there is the idea that circulating tumor cells have to seed regional, distant organs and also the source site, known as 'tumor self-seeding'.[7] In particular, the interaction of the cancer cells with their surroundings, as extracellular matrix (ECM), blood vessels, associated macrophages, and fibroblasts, represents a key role in tumor progression and it is known as the tumor microenvironment (TME).[8-9] These cancers associated changes towards a pro-tumorigenic environment are shown detailed in Figure 1.1.

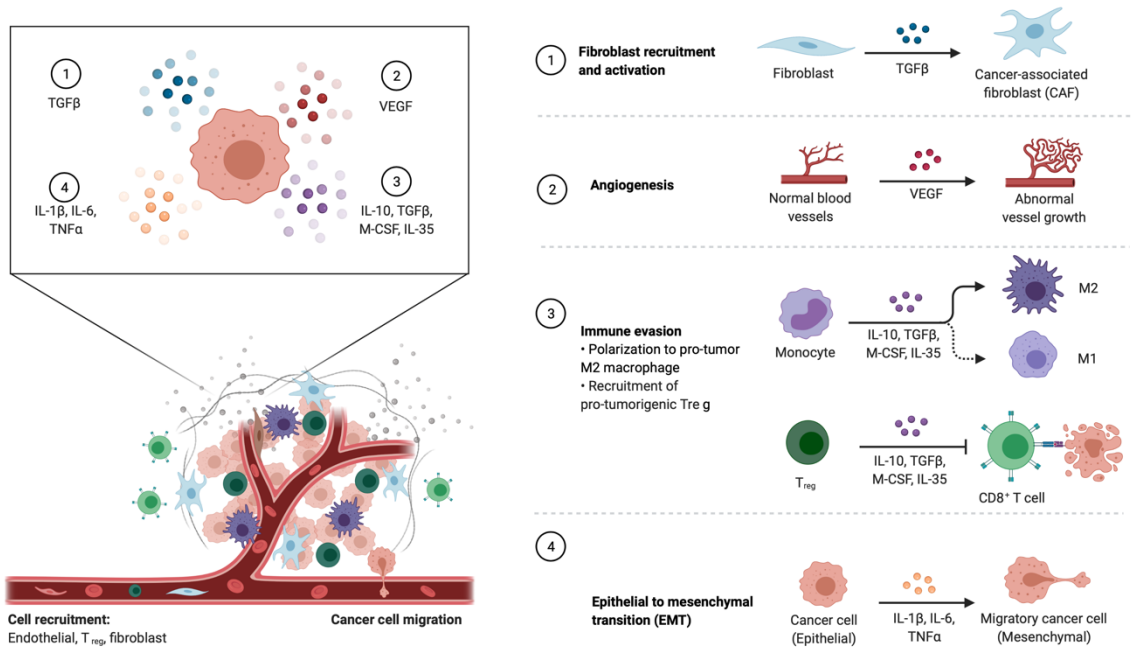

Figure 1.1 - Schematic representation the tumor microenvironment (TME) and overview of cancer-associated changes. TME is represented by tumor, immune cells, fibroblasts, epithelial cells, extracellular matrix and blood vessels. Fibroblasts and macrophages are known to suppress the cancer growth; however, these cells are further educated by tumor growth factors (TGF) to acquire pro-tumorigenic functions. 1) Fibroblasts are activated by TGF to became cancer activated fibroblasts (CAFs) that latter release vascular endothelial growth factor (VEGF) that supports 2) angiogenesis. 3) Tumor associated-macrophages (TAMs) and T-cells are educated with interleukins (IL), macrophage colony stimulation factors (M-CSF) and TGF into pro-tumorigenic states for immune evasion. 4) Finally, cancer cells lose their epithelial property to gain migratory properties towards mesenchymal cells by IL and Tumor Necrosis Factor-α (TNF-α).[4]
Source: Created with biorender.com.

TME complexity hinders the treatment by free chemotherapeutics, due to low concentration at tumor side, resulting in severe side effects.[10] In tumor formation, as shown in Figure 1.1, there is a rapid growth of new chaotic vasculature characterized by elevated interstitial fluid pressure and suppressed lymphatic drainage.[11] As a consequence, nanoscale carriers and macromolecules accumulated in the target site.[12] This sized-related accumulation in tumors is defined by enhanced permeability and retention effect (EPR) and have translated into efforts for nanomedicines development for cancer therapy.[13-14]

Despite the EPR effect, less than 1% of the administered dose of nanomedicines reaches the solid tumor.[15-16] When a nanomaterial is administered into the body, it encounters several complexes interfaces that have mechanisms to

eliminate foreign bodies.[17] For example, when in bloodstream proteins absorbs in nanoparticles surface and might compromise their performance.[18] Therefore, an efficient biointerfacing of the nanomaterials is an important step for a successful translation *in vivo*.[19]

Biomimicking nanoparticles using natural membranes-bound substrates enables applications beyond those traditionally treatments. Cell-membrane coating technology was first reported in 2011,[20] and 10 years later it still have many improvements to be reported.[21-23] The main hypothesis of the approach is that nanoparticles functionalized with cell-membrane nanoparticles inherits properties of the source cells. As an example, red blood cells-coated nanomaterials endows the prolonged circulation time[20,24] and cancer cell-based nanoparticles actively target tumor sites by homotypic binding.[22,25]

Extracellular vesicles (EVs) coating is also an valuable approach to enhance circulation time,[26-27] target tumor sites[28-30] and modulate tumor microenvironment.[31-32] EVs are known to interplay communication between cells, depending on their donor cells and origin.[27] These membrane-bound carriers are classified by their size, as small (50-200 nm), medium (200-1000 nm), and large extracellular vesicles (1-10 μm).[33] In the small class, they originate from two forms, by endosomal (exosomes) or plasma membranes (microvesicles) release.[34] A study comparing two types of EVs shows that the microvesicles delivered functional reporter molecules to recipient cells, while exosomes don't.[27]

Although the hypothesis that these nanoparticles endow the characteristics from the donor cell, there is still knowledge to accumulate on the role of proteins in the bio-nano interface.[19] It is known, for example, that integrin-associated protein CD47 has a role in regulating phagocytosis from macrophages.[35] CD47 acts as a "self-marker" on some cells[36-37] and are overexpressed in cancer cells.[30,38-39] This protein is a ligand for the signal regulatory protein α (SIRPα) and has an inhibitory role in phagocytosis.[40] When there is the interaction CD47-SIRPα the macrophages identify it as a self-cell and do not phagocyte.[36] Additionally, adhesion molecules also showed an important role in organotropism of the cell-derived nanoparticles.[41]

The aim of this study was to develop novel nanomaterials using biomimicking strategies and to investigate their behavior in cells from TME. For this, two different nanomaterials were synthesized and further coated with different cell-derived vesicles. We started our studies with the synthesis of gold nanorods due to their theranostic properties for biomedical applications and coated with two macrophages cell derived membranes: extracellular vesicles and cell membrane extract. Also, we synthesized polymeric nanocarriers and coated with metastatic cancer cell membrane extract. For all these novel cell-derived nanoplatforms, we evaluated their *in vitro* interaction with stroma and cancer cells. Based on the exposed, the thesis explores four experimental chapters (see overview in Figure 1.2).

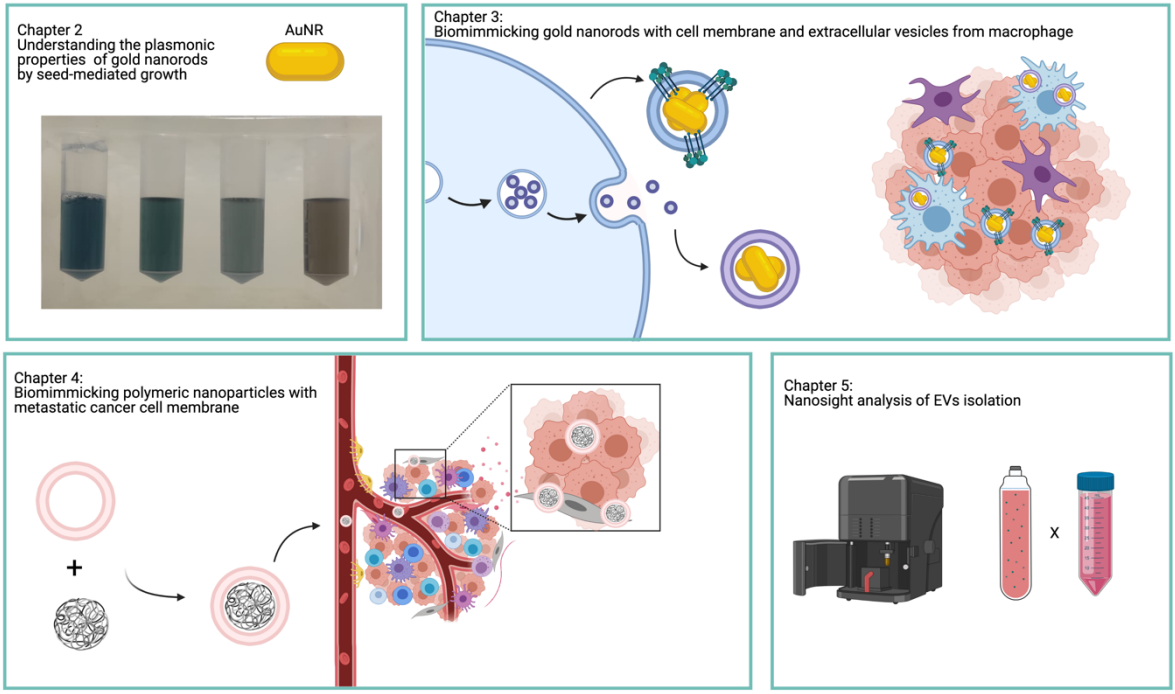

Figure 1.2 - Schematic overview of the thesis. In Chapter 2, we investigated the tunability of gold nanorods using the seed-mediated synthesis. In sequence, we functionalized the gold nanorods optimized earlier with cell membrane e extracellular vesicles from macrophages and compared their interaction with metastatic cancer and stroma cells (Chapter 3). In Chapter 4 we coated paclitaxel encapsulated polymeric nanoparticles with metastatic cancer cells and investigated their performance for cancer therapy. Finally, in Chapter 5, extracellular vesicles isolation was investigated by means of their size and concentration using Nanotracking analysis.
Source: By the author created with biorender.com.

In **Chapter 2**, we explore the dependence of the surface plasmon resonance on parameters as composition and size of gold nanorods (AuNRs). The AuNRs were synthesized by seed-mediated method and through small differences in the protocol

we could obtain regular and small sized AuNRs. All particles were characterized by electronic microscopy and spectroscopic techniques. We were able to synthesize AuNRs with strong absorption in the in the near infrared.

In **Chapter 3**, we show development of two biomimetic gold nanorods and evaluated their differences using cells that model TME. Mini Gold nanorods, previously optimized, were coated with extracellular vesicles and cell membrane from macrophage (RAW264.7). Both nanoplatforms were well characterized using spectroscopic and electron microscopies techniques. Furthermore, cellular uptake and cytotoxicity in cancer and stroma cells were analyzed.

In **Chapter 4**, we report the development of a cancer cell membrane-coated polymeric drug delivery platform for cancer therapy. The nanomaterial was characterized using spectroscopic and electron microscopies techniques. Epithelial and non-epithelial cells lines were used to assess the biointerface of the nanomaterial.

Chapter 5 brings the results from an investigation of the basic parameters of EVs isolation in a Nanosight analysis perspective. The yield of EVs isolation were evaluated by concentration and size distribution. Basic culture parameters, two isolation methods and two different cell lines were evaluated. EVs were also characterized by electron microscopy.

2 SYNTHESIS AND CHARACTERIZATION OF GOLD NANORODS

2.1 INTRODUCTION

Nanomaterials to improve drug delivery and therapy represent a growing scientific field with commercialized products in several countries.[42-43] These systems aim to reduce drug toxicity, assure drug stability, improve bioavailability and treatment efficacy.[44] An important characteristic of nanoparticles, regardless of composition, is their reduced size which favors enhanced permeation and retention (EPR) effect in tumor tissues.[45] Besides the EPR, plasmonic nanoparticles continue to stand out due to Localized Surface Plasmon Resonance (LSPR).[5-6] This phenomenon is the coherent oscillation of the free electrons of metallic nanoparticles surface when in resonance with the electromagnetic field. First described by Mie, LSPR depends on parameters as size, shape and dielectric constant of the surrounding medium.[48] Such tunable properties make them great candidates for applications in sensing, imaging and therapies.[49-50]

For certain frequencies of incident light, the system reaches the condition of resonance occurring photothermal conversion, where part of the incident energy is absorbed and dissipated in the form of heat.[51-52] This dissipation in heat is broadly applied in cancer to improve selectivity and effectiveness of treatments.[51,53] The plasmonic photothermic therapy (PTT) requires wavelengths in regions of the spectrum where light absorption by water and tissues is minimized.[54] Thus, to optimize the efficiency of the nanoparticles, they must be synthesized so that their plasmonic band is located in one of the two biological absorption windows, in the near infrared (NIR) between 650 and 980 nm or between 1000 and 1400 nm.[55]

Anisotropic gold-based nanomaterials are the most used nanomaterials for biomedical applications.[56] The most common anisotropic plasmonic nanomaterial used is the rod-shaped. Gold nanorods (AuNRs, width > 10 nm) have a trademark of two band peaks, resulted from the coherent movement of the electron conduction band along the two directions of the particle, as shown in Figure 2.1.[57] The transverse band occurs in the visible region around 525 nm, while the longitudinal band occurs in the near infrared region.[58-60] While the transverse band is not dependent on the size of the nanorods, the longitudinal band is translated from the

visible to the near infrared region, with an increase in the aspect ratio (length/width).[59]

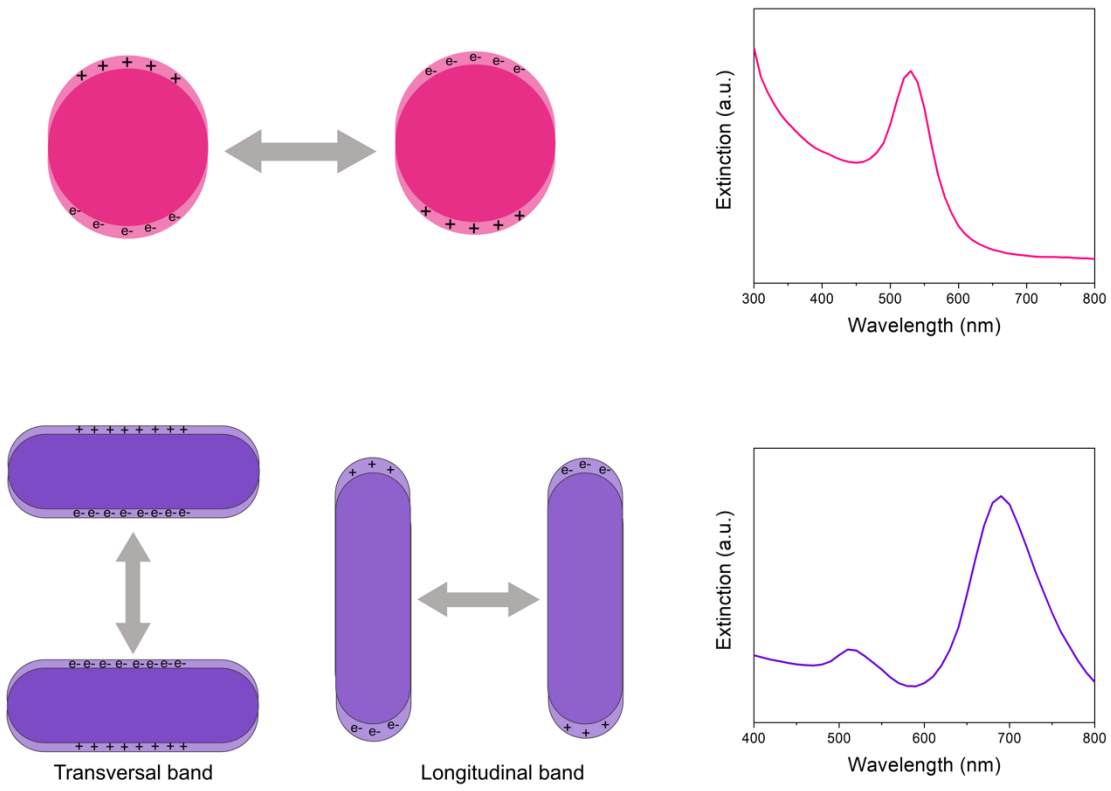

Figure 2.1 - Schematic representation of the LSPR oscillation and their extinction spectra of nanoparticles and nanorods.
Source: By the author.

AuNRs can be synthesized by several methods as photochemical[61, 62] and seed-mediated growth[58,63-64] routes. The latter is broadly used and is based on addition of small gold nanoparticles, called seeds, into a gold growth solution.[65] Although it is the common method applied, the reproducible synthesis of monodisperse nanorods is a major issue in upscaling for biomedical applications.[66] Details, as the water used to the age of the gold solution, has a major impact on the final aspect ratio of AuNRs and on the reproducibility between batches.[67] In addition to all these challenges the synthesis of gold nanorods generates particles from 10-20 nm in width and 30 to 80 nm in length,[58,68-69] which exhibits low cellular uptake and slow clearance.[70-72] Mini AuNR, with width bellow 10 nm, shows higher cellular uptake, fast clearance and better photothermal therapy efficiency.[59,64,73-74]

Here, we explored the seed-mediated growth synthesis of AuNRs and mini AuNRs. Our main goal was to evaluate how the parameters of the synthesis changed the surface plasmon resonance and size of AuNRs. Each reagent role was investigated in detail. Silver nitrate plays an important role in the anisotropic growth of AuNRs, for both synthesis, providing higher aspect ratios nanorods when increasing the concentration. Seeds concentration was also evaluated. For traditional synthesis of AuNRs, when increasing the seeds amount, there is a shift towards near infrared of the longitudinal band. For mini AuNRs the contrary is observed, a decreased in seeds amount caused a increase in the aspect ratio. Also, luminescence and photothermal conversion were evaluated. AuNRs show a non-linear luminescence close to a quadratic dependence to power. Finally, mini AuNRs showed an increase of 65 ºC, being able to increase under the hyperthermia regime in only 1.8 minutes.

2.2 METHODOLOGY

2.2.1 Materials

The aqueous solutions were prepared with ultrapure water (resistance 18.2 MΩ.cm, Mega Purity Waters). The following materials and reagents were used: dimethylsufoxide (DMSO, Synth), tetrachloroauric acid ($HAuCl_4$, #MKCJ4933 and undefined, Sigma Aldrich), silver nitrate ($AgNO_3$, #STBHS752, Sigma Aldrich), cethyltrimethylammonium bromide (CTAB, #SLBW4713 and #SLCB0191), sodium borohydride ($NaBH_4$, Sigma Aldrich #MKBK3564V and #STB7581V), L-ascorbic acid (AA, #SLB50713V and #SLBJ1088V) methyl polyethylene glycol thiol ether (mPEG-SH, Mn 5000), 3-(4,5-dimethylthiazol-2yl)-2,5-diphenyl tetrazolium bromide (MTT, Sigma Aldrich), dibasic sodium phosphate (Na_2HPO_4, Sigma Aldrich), monobasic potassium phosphate (KH_2PO_4, Sigma Aldrich). The sulfuric acid was acquired from Qhemis and hydrochloride acid from synth. All the glassware used in the synthesis was previously cleaned with aqua regia and washed several times with deionized water.

2.2.2 Synthesis of the gold nanorods

For the regular size AuNRs, the seeds were prepared as following.[53] 250 µL of $HAuCl_4$ (Undefined lot) at 0.01 mol L^{-1} were added into 7.5 mL of CTAB (#SLBW4713) at 0.1 mol L^{-1} and mixed under magnetic stirring for one minute. Then, 600 µL of 0.01 mol L^{-1} $NaBH_4$ (#MKBK3564V) was added quickly and left under stirring for 10 minutes. $NaBH_4$ solution was prepared prior to the reduction and under an ice bath. The seeds were maintained at 25 ºC before use for 2 hours, in order to release gases produced at the reaction.

The growth solution was prepared by adding 3 mL of $HAuCl_4$ (Undefined lot) at 0.01 mol L^{-1} in 47 mL of CTAB (0.1 mol L^{-1}, #SLBW4713). To evaluate the influence of silver nitrate (#STBHS752) in the aspect ratio, increasingly amounts at 0.01 mol L^{-1} were added (600, 800 and 900 µL) and 480 µL of ascorbic acid (#SLBJ1088V) 0.1 mol L^{-1} was added to the solution sequentially. Finally, 100 µL of pre-prepared gold seeds was added. Additionally, to analyze the influence of the seeds in the synthesis, the growth solution was prepared as above with a difference that the silver nitrate volume was fixed at 600 µL at 0.01 mol L^{-1}. Different concentration of seeds (50, 70, 100 and 170 µL) were added to the growth solution. The systems were kept at room temperature for at least 24 hours and then centrifuged 5x at 1,500g for 5 minutes at 4 ºC to remove the excess of CTAB.

2.2.3 Synthesis of small sized gold nanorods

For mini-AuNRs, the seeds were prepared by changing the volume of CTAB. [59] 250 µL of 0.01 mol L^{-1} $HAuCl_4$ (#MKCJ4933) was added to 9.75 mL of 0.1 mol L^{-1} CTAB (#SLCB0191) and left to stir for one minute. 600 µL of cold 0.01 mol L^{-1} $NaBH_4$ (#STB7581V) was added vigorously to the solution. The dispersion was left under magnetic stirring for 10 minutes and maintained at 25 ºC for 1.5 hours before being used to release the hydrogen produced in the reduction.

The growth solution was prepared by mixing 2 mL of 0.01 mol L^{-1} $HAuCl_4$ (#MKCJ4933) with 36 mL of 0.1 mol L^{-1} CTAB (#SLCB0191). In the sequence, 120 or 200 µL of 0.01 mol L^{-1} $AgNO_3$ (#STBHS752), 800 µL of 1mol L^{-1} HCl (Synth) and 320 µL of 0.1 mol L^{-1} ascorbic acid (#SLB50713V) were added to the solution sequentially. Finally, 8 mL of the previously prepared gold seeds were added. The system was maintained at room temperature for at least 24 hours and then centrifuged at 1500g for 5 minutes at 4 ºC to remove excess of CTAB crystals in solution, this process was repeated 6 times. For longer nanorods (longitudinal plasmon band close to 810 nm), the growth solution was the same as above, with the difference that it was used 400 µL of 0.01 mol L^{-1} $AgNO_3$ (#STBHS752). Also, only 4 mL of the seeds were added.

2.2.4 Characterization of the AuNRs

UV-Vis (ultraviolet-visible) measurements. Gold nanorods and seeds UV-Vis spectra was taken using a microplate reader SpectraMax M3 (Molecular Devices) in a deionized water 1:10 dilution using a quartz cuvette.

Dynamic light scattering (DLS). Size distribution of the seeds were performed using Zetasizer Nano ZS90 (Malvern Instruments). The seeds were loaded into a disposable cuvette without further dilution, and three independent measurements were performed.

Scanning electron Microscopy (SEM). At least 10 images in different regions were collected using ZEISS SIGMA VP FE-SEM. Samples (diluted in ddH_2O at1:10) were deposited at 10 µL onto clean silicon substrate and let it dry at room temperature. After, the samples were coated with platinum plasma spraying. To determine nanorods dimensions, 100 particles were counted and measured using Image J.

Transmission Electron Microscopy (TEM). The TEM images were obtained in JEOL 1400 or JEM-2100 TEM. Samples were prepared by drop-casting 3µL on copper grids for 60 seconds and dried with filter paper. TEM images were collected in 10 different regions and at least 100 particles were counted and measured to evaluate nanorods size distributions.

Two-photon luminescence assay. The gold nanorods were deposited in a glass slide and mounted with a cover slip. The spectra was collected using a laser

scanning microscope (Zeiss, LSM780), a femtosecond Ti:sapphire laser at 800 nm at different powers intensities, with a maximum power of 3.8W. The power of the laser was varied from 1-9%, to evaluate the dependence of the power with the intensity spectrum.

Photothermal conversion studies. 1 mL of mini AuNRs were placed a polystyrene cuvette in a dilution of 1:10 in 1x phosphate buffer saline (PBS) from stock solution (Optical density at 750 nm of 0.4) and irradiated using a 808 nm continuous pulse laser with elliptical beam of diameter close to 1.5 mm x 3.0 mm (iZi, LASERline). The power of the laser used was approximately 1.5 W cm^{-2}. The temperature changes were monitored by an optical thermometer (Luxtron).

2.3 RESULTS AND DISCUSSION

2.3.1 Characterization of the seeds

The seeds synthesis (Figure 2.2A) lies in the rapid reduction of Au^{3+} to Au^{0} by $NaBH_4$. Thus, the $NaBH_4$ reagent is an important step to produce liable seeds to be further added to the growth solution. The change of the yellow solution to a brown color (Insert in Figure 2.2B) shows the effective reduction of the nanoseeds, resulting in a low intensity plasmon band close to 500 nm, characteristic of nanoparticles with sizes bellow 10 nm (Figure 2.2B). This characteristic LSPR band is related to damping of the high collisions rate of electrons when in collective oscillation, due to the small size of the nanoparticles.[75-77] The LSPR band related to small sizes is confirmed by DLS in Figure 2.2.C,with a size distribution around 1 nm and polydispersity index (PdI) of 0.195. DLS measurements without size distortion was only possible due to low PdI index.[78] For the mini AuNRs synthesis, seeds synthesis procedure was maintained, except by adding more CTAB (Data not shown).

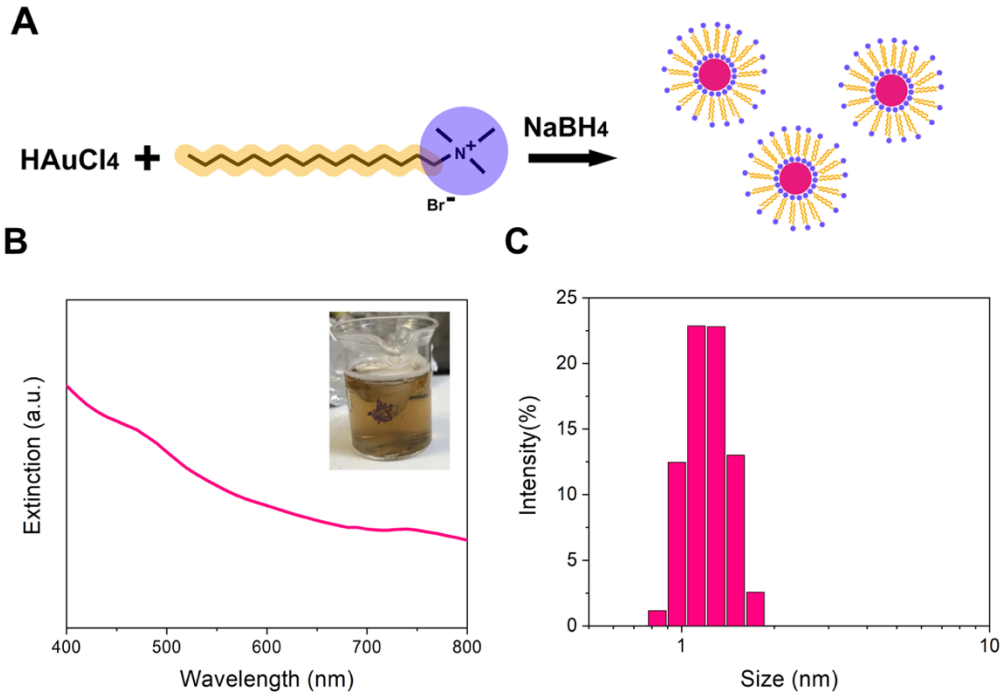

Figure 2.2 - Characterization of seeds from regular size synthesis. A) Synthesis scheme of the seeds by strong reduction with sodium borohydride. B) Extinction spectrum of the seeds and their color as insert. C) Size distribution by DLS (n=1, PdI=0.195).
Source: By the author.

2.3.2 Characterization of AuNRs growth parameters

In order to better understand the effects of the reagent in the synthesis, the concentration of silver nitrate and the seeds were varied in the growth solution, and the results are shown in Figure 2.3.

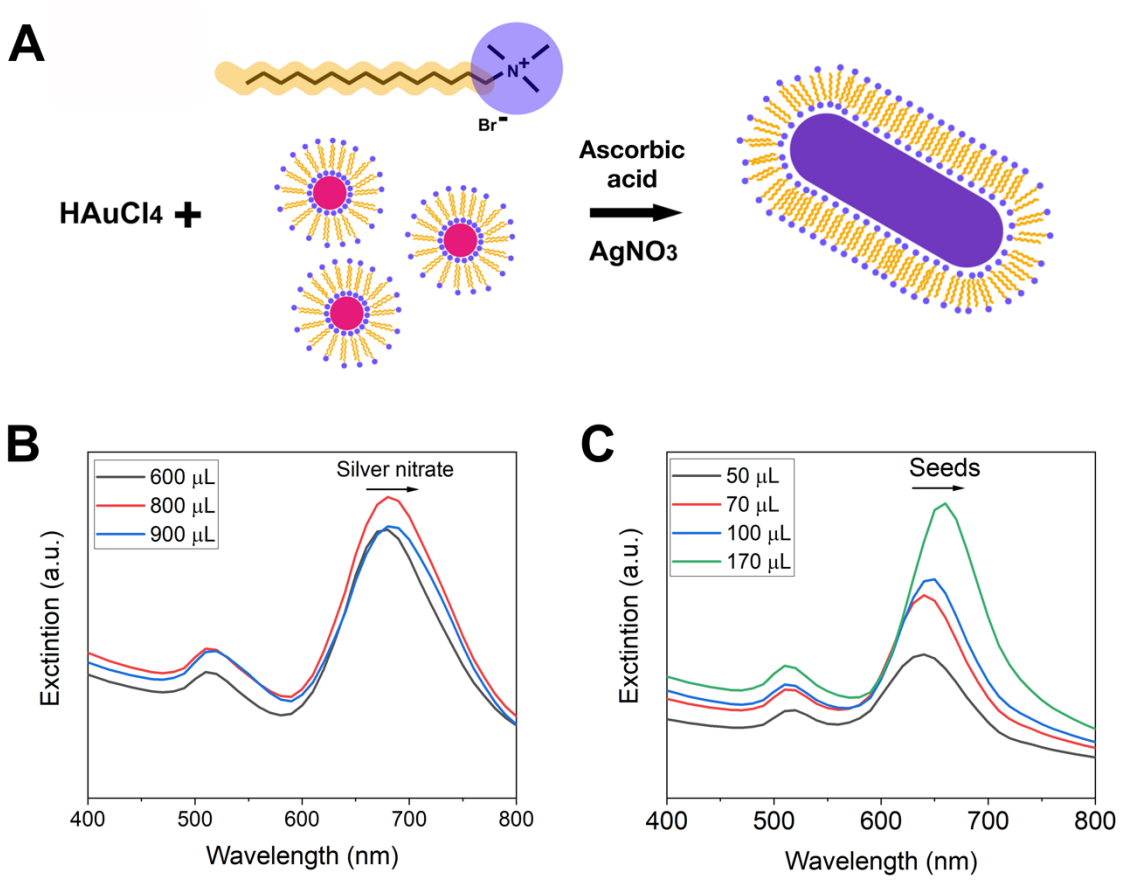

Figure 2.3 - Characterization of anisotropic growth of regular size gold nanorods. A) Synthesis scheme of the rods by ascorbic acid reduction in the presence of silver nitrate. B) Extinction spectra of nanorods synthesized adding increasing amounts of silver nitrate (600, 800 and 900 µL), using a fixed volume of seeds at 100µL. C) Extinction spectra of nanorods synthesized adding increasing amounts of seeds (50, 70, 100 and 170µL), using a fixed volume of silver nitrate at 600µL.
Source: By the author.

Figure 2.3B shows the UV-Vis spectra of the nanorods using increasing amounts of silver nitrate at fixed seeds concentration of 100 µL. Higher silver nitrate concentrations shifted the longitudinal plasmon band towards near infrared, yielding nanorods with higher aspect ratios. $AgNO_3$ plays a key role in the anisotropic growth, and when not used in the synthesis, the final suspension presents a large population of spherical shaped nanoparticles.[79] There are several proposed mechanisms on the effects of Ag^+ ions on the AuNRs synthesis. The main consideration to the use of Ag+ ions is that, at the synthesis pH, the ions are not reduced in the presence of ascorbic acid.[58] One mechanism proposed is the formation of silver bromide (AgBr) in the presence of CTAB, which adsorbs in restricted faces of the seeds, limiting the growth in one direction.[60] Another study suggested the decrease in charge density by

AgBr, and, as a consequence, the electrostatic repulsion between the headgroups of CTAB directing the AuNRs growth.[58] Liu and colleagues proposed that Ag^+ ions decrease the growth rate and increase the energy in the plane {110} of the nanorods, allowing the adsorption ions on sides with specific structures, directing the growth.[80]

Additionally, a detail investigation using atomic scale electron microscopy reported the mechanism of growth.[81-82] Seeds prepared in the presence of CTAB shows a cuboctahedral morphology, and when added to the growth solution they grew up to 4-6 nm isotropically. In the presence of silver nitrate, there is the formation of truncated surfaces at the intersection {111} facets, which are preferred sites for the deposition of silver ions, resulting in orientated growth.[81]

The aspect ratio can be also controlled by changing the concentration of seeds in the growth dispersion. By fixing the concentration of nitrate at 600 μL, different amounts of seeds were added, and the UV-Vis spectrum is shown in Figure 2.3C. As the number of seeds increases, there is a red nonlinear shift of the longitudinal band, in accordance to literature data.[83- 85]

The data above (Figure 2.3) show that by changing the concentration of seeds and silver nitrate there is a displacement of the longitudinal band towards the near infrared, however, it is still not sufficient for biomedical applications.[86] Therefore, the change in pH was evaluated in the nanorods synthesis. When the growth solution was acidified with sulfuric acid, a slow growth and increased aspect ratio occurred, as shown in the Figure 2.4A. SEM analysis (Figure 2.4B) shows a homogeneous population of rods. Histogram evaluations showed a width of 14 nm and a length of 42 nm, resulting in an aspect ratio of 3.

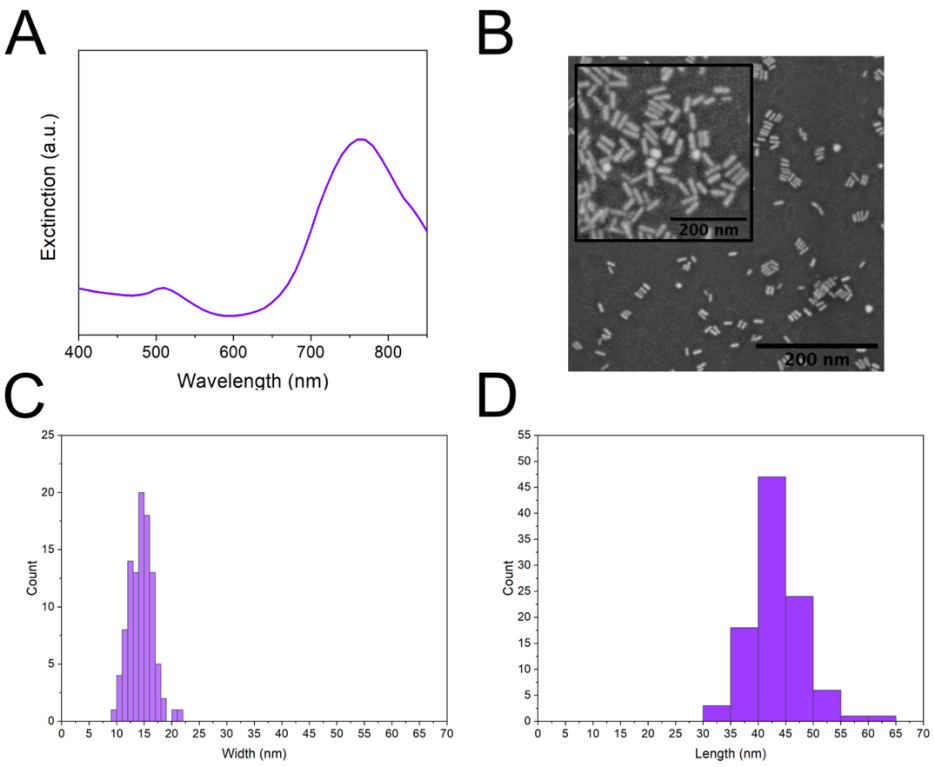

Figure 2.4 - Characterization of anisotropic growth of gold nanorods adding sulfuric acid. A) Extinction spectra of nanorods synthesized adding 1mL of sulfuric acid 0.5 mol L^{-1} with 600 µL of silver nitrate and 200 µL of seeds. B) SEM images of the synthesis. Histogram of C) width and D) length evaluating 100 particles from SEM images.
Source: By the author.

2.3.3 Two-photon fluorescence analyses

Two-photon or multi-photon luminescence are a promising tools for diagnostic because them provide greater penetration in tissues when compared to single photon fluorescence. [86] The nonlinear luminescence is based on the colocalization of two or multi photons of low energy (usually near infrared) in one molecule. This fluorescence is shown to be similar than single photon luminescence, however, with a weaker signal. Metallic nanoparticles can be used as agents to amplify this signal by resonant coupling with localized surface plasmons. Gold nanorods are appealing as agent once their longitudinal plasmon band are resonant at near infrared, exploiting the biological window. Additionally, their anisotropy holds the LSPR without damping phenomenon. [87] It is known that the anisotropy of AuNRs systems favors the excitation by two photons, the higher aspect ratio, the higher the fluorescence intensity.[88] Thus, the characterization of the AuNRs by two-photon luminescence

(TPL) is a paramount step for biomedical applications. Figure 2.5 shows the characterization of the TPL of the gold nanorods before optimization with sulfuric acid.

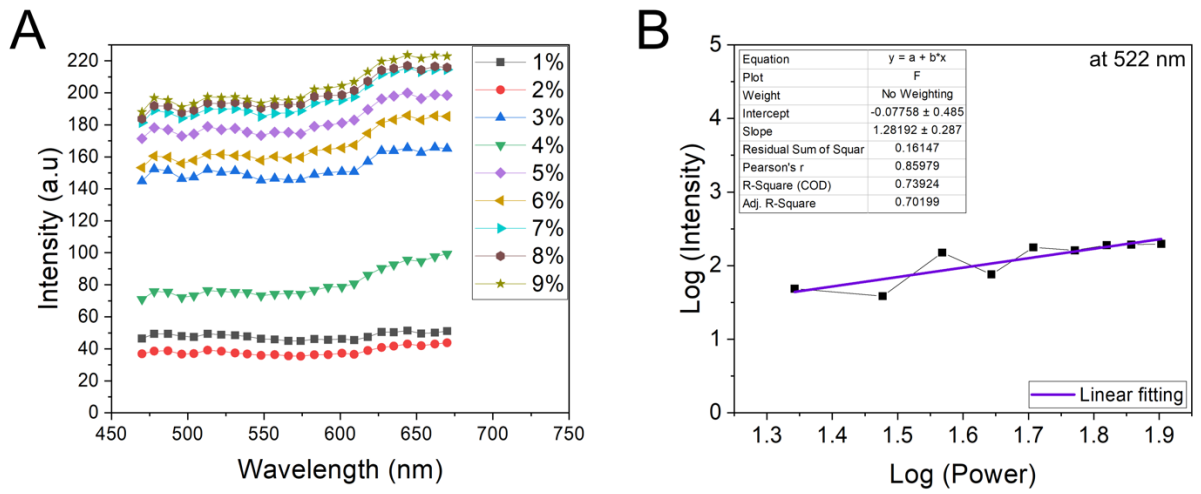

Figure 2.5 - Two-photon luminescence from gold nanorods. A) Photoluminescence spectra of AuNRs at different powers of laser Ti:sapphire at 800 nm of excitation. B) Dependence of the luminescence intensity as a function of the excitation power at 522 nm.
Source: By the author.

The TPL intensity has a quadratic dependence on the laser power (Figure 2.5A). Therefore, the logarithm graph it is expected to present a slope close to 2.[86] The linear fitting confirmed the non-linear nature of the TPL, once the slope is higher than 1. However, the value was in 1.3 ± 0.3 and more data points and batches analysis are required or elongating more the AuNRs is needed to increase this phenomenon.

2.3.4 Reproducibility challenges in the AuNRs synthesis

Although the synthetic route employed here is widely used for AuNRs fabrication, some aspects were evaluated during the optimization process.[67] The main problems faced during the synthesis will be highlighted in this section.

The quality of the deionized water was one of the sources of irreproducibility. Firstly, the nanorods generated asymmetric longitudinal plasmonic bands (as seen in Figure 2.6), probably as a consequence of contaminant traces in the water or the

change in pH.[67] In addition, the aging of the tetrachloroauric acid was the main challenge faced in the synthesis. In a fresh solution there is a high content of Cl^- coordinating the gold ions which does not yield rod-shaped nanoparticles.[89]

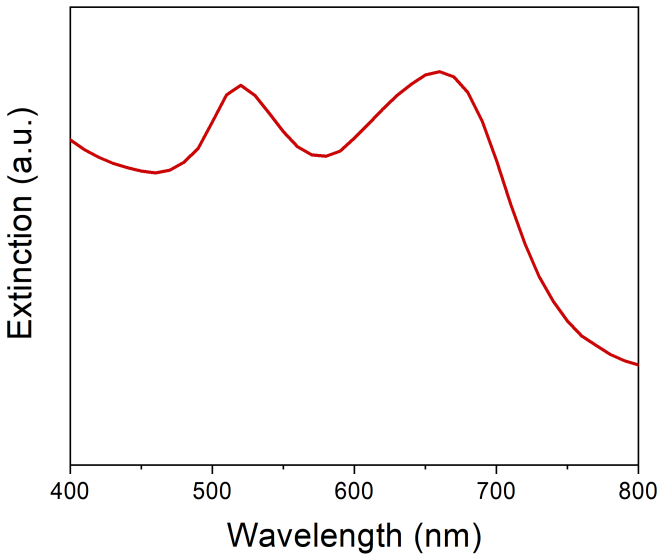

Figure 2.6 - Characterization of nanorods reproducibility. Extinction spectrum of AuNRs shows that the transverse and longitudinal plasmon bands are with close intensities, which is resulted in the high presence of spherical particles. Additionally, the longitudinal band is shown asymmetry.
Source: By the author.

2.3.5 Characterization of Mini AuNRs

Familiarized with the role of each reagent in the synthesis and the challenges of reproducibility, we started the synthesis to produce small sized AuNRs. Mini AuNRs have several advantages when compared to regular size AuNRs. By decreasing the width, there is a minimization of the scattering and the dominance of absorption cross-section, which enhances the photothermal conversion efficiency.[90] Besides, the mini AuNRs exhibit a faster clearance rate and higher uptake by cells.[73] The change in the protocol is related to the addition of hydrochloric acid in the growth solution and the addition of 20-fold more seeds as the traditional protocol. Figure 2.7 shows the optimization of mini AuNRs by changing silver nitrate and seeds volumes.

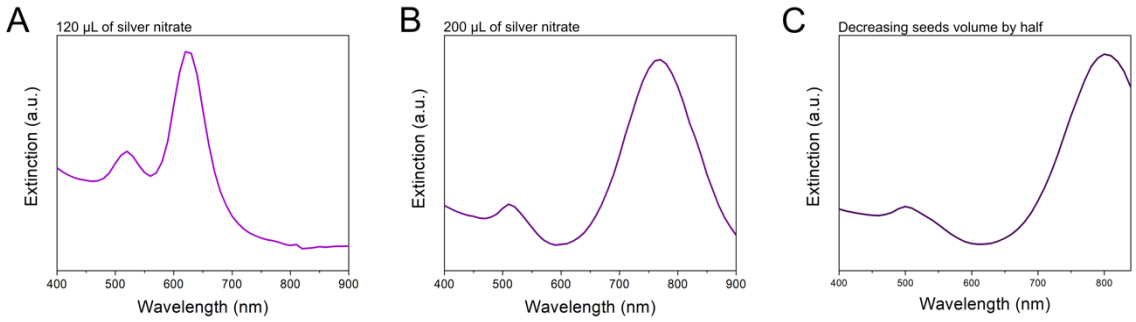

Figure 2.7 - Characterization of mini AuNRs synthesis. Extinction spectra of mini AuNRs varying silver nitrate at A) 120 µL and B) 200 µL and C) decreasing the seeds volume by half.
Source: By the author.

As expected, by increasing the concentration of silver nitrate, a shift of the longitudinal peak towards red occurs (Figures 2.7A-B). These results confirm the importance of silver in the anisotropic growth by the mechanisms proposed before. As observed for the regular size AuNRs, the proportion of seeds:Au^{3+} has an important effect on size. By increasing this ratio, there is a decrease in gold ions per seeds available to growth, affecting the thickness of the final rods. Less seeds leads to thicker AuNRs.[64] Thus, to produce mini AuNRs synthesis there is 10-20 times increase in the seeds concentration when compared to the traditional methods.[59] Contrary to regular size AuNRs, a decrease in the seeds:Au^{3+}, still with excess of seeds, the synthesis produced more elongated rods (Figure 2.7C).

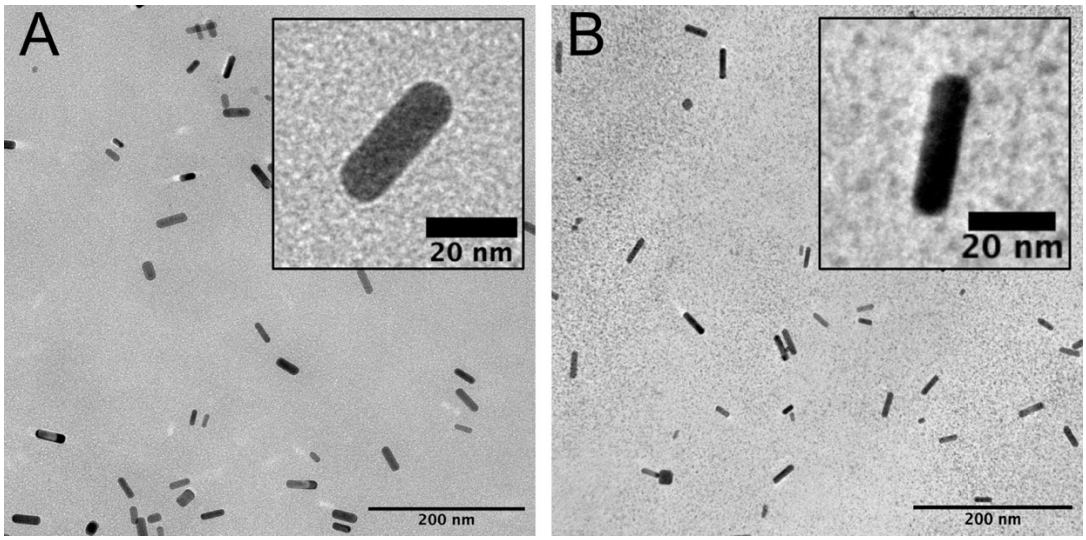

Figure 2.8 - Images mini AuNRs synthesis. A) TEM images of mini AuNR with longitudinal band close to 750 nm, using silver nitrate 200 µL as in Figure 2.7B. B) TEM images of mini AuNRs with longitudinal peak close to 810 nm, decreasing the seeds concentration by half related to the Figure 2.7C.
Source: By the author.

TEM analysis are displayed in Figure 2.8. Both syntheses showed a width bellow 10 nm. Mini AuNRs using 200 µL of $AgNO_3$ (Figure 2.8A) show an average width of 9 nm and average length of 34 nm, resulting in an aspect ratio of 3.7 (100 particles were considered). By maintaining the same concentration of silver nitrate and decreasing the seeds concentration by half, we obtained mini AuNRs with anerage width of 7 nm and length of 28 nm, thus, the aspect ratio was of 4 (Figure 2.8B, 100 particles were considered).

As stated before, gold nanorods can be applied as photothermal agents for cancer therapy, and it is known that mini AuNRs have a better performance when compared to regular size AuNRs.[90] It is essential to evaluate their photothermal response.[55] The mini AuNRs with longitudinal band close to 750 nm was chosen for photothermal conversion (Figure 2.9). The temperature increased from 25 to 90 ºC, with a total variation of 65 ºC. The maximum temperature was reached in 11.3 minutes of irradiation. The hyperthermia regime, which requires a temperature range of 41-50 ºC, was reached in 1,8 minutes.[91] When the laser is turned off, it needs approximately 30 minutes to decrease the temperature to 33 ºC, showing their strong absorption capacity.[92]

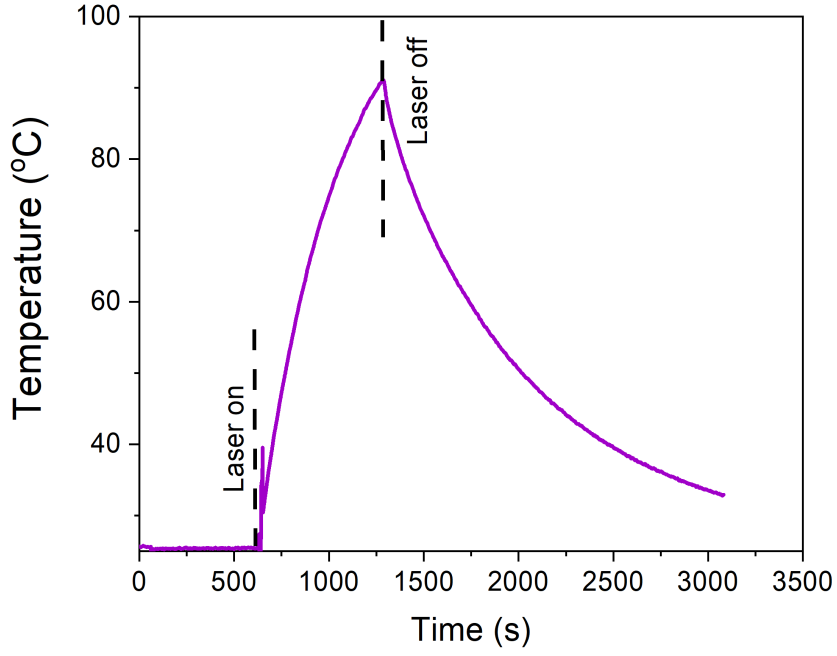

Figure 2.9 - Photothermal conversion study of mini AuNRs with longitudinal band of 750 nm. Temperature versus time plot when irradiating mini AuNRs (Optical density at 750 nm of 0.4, diluted 1:10 in PBS) using irradiated continuous wavelength at 808 nm, with power of 1.5 W cm^{-2}. After is reached 90 ºC the laser was turned off to evaluate the first photothermal cycle.
Source: By the author.

2.4 CONCLUSIONS

We have presented the synthesis and characterization of two sizes of gold nanorods, and their LSPR dependence on parameters as size and composition. Both gold nanorods were synthesized by seed-mediated growth method in the presence of CTAB. The main difference between the regular size compared to mini AuNRs is related to their width, in which traditional AuNR have a width above 10 nm and mini AuNRs bellow 10 nm. In the mini AuNRs synthesis there is the addition of hydrochloride acid and a 10x higher concentration of seeds. Silver nitrate, in both methodologies, increased the aspect ratio of AuNRs, when in higher concentrations. Seeds concentration influenced differently. Large AuNRs had higher aspect ratios upon increasing the seeds amount. On the contrary for mini AuNRs decreased seeds amount resulted in increased aspect ratio. TEM analysis confirmed the size changes related to LSPR observed in extinction spectra. Finally, the optical properties interesting for biomedical applications were evaluated. Regular size AuNRs showed a non-linear luminescence. Additionally, mini AuNRs had an excellent performance as photothermal agents, being able to reach temperatures above the hyperthermia regime. Understanding the synthesis methodology and the plasmonic properties of AuNRs is a key step to their evolution in cancer therapy.

3 THE FATE OF GOLD NANORODS FUNCTIONALIZED WITH EXTRACELLULAR VESICLES AND CELL MEMBRANE: A COMPARISON STUDY

3.1 INTRODUCTION

Gold-based nanomaterials have gained attention due to their plasmonic properties combined with their high stability and low citotoxicity.[93] Among these, rod-shaped nanostructures, or nanorods (NRs), have received attention since their plasmonic surface resonance band is divided into two bands when compared to one band profile of the gold nanoparticles, due to the coherent movement of the electron conduction band along the two directions of the particle. The transverse band occurs in the visible region, while the longitudinal band can be tunable near the infrared region.[79] These tunable characteristics implies in several applications, such as photothermal therapy and diagnosis.[79,94]

Although the exponential progress that has been reported in the tunability of metallic nanomaterials, it is known that only 0.7% of the administered dose of nanoparticles *in vivo* reaches solid tumors.[16] For that, nanoparticles functionalization with polyethylene glycol (PEG) has been used to prolong their *in vivo* half-life. Despite considered the gold-standard for applications, PEG-derived nanoparticles have been known to activate immune system responses.[95] Thus, new strategies to functionalize nanomaterials have been developed, with special attention to the use of cell membrane materials to cover the nanoparticles.[53,96] This strategy has proved to be an interesting alternative to camouflage and to increase the circulation time of theparticle when compared to nanoparticles coated with PEG.[20] Besides the prolonged circulation time advantage, cell membrane-coated nanoparticles endow the properties of the source cell. For example, cancer cell membrane-coated nanoparticles actively target tumor sites due to the homologous adhesion, however their capability to escape the immune cells is limited.[97] Macrophages cell membrane nanoparticles was proven to escape the immune system and target tumor cell lines.[98-99]

Recently findings demonstrated that extracellular vesicles (EVs) can also be employed as excellent carriers for drug delivery.[28,100-102] EVs are classified by their

size and have received increased attention. Small extracellular vesicles, once known as exosomes, with sizes between 50-150 nm, have been shown to support communication between cells.[103] The EVs characteristics, as size and long distant communication, are related to their biogenesis and the type of the source cell. Most of the small EVs are generated with the membrane folding inward, creating intraluminal vesicles that mature into multivesicular bodies, and are released by the cells by fusion with the plasma membrane (Figure 1.A).[104-105] Tumor-based EVs are capable of targeting cancer cells, being used as an alternative for treatment of cancer, once they have shown high stability and long distant communication.[30,106] Macrophage derived EVs play an important role in immunoregulation.[28,107]

All of the cell-derived nanoparticles have the premise of 'do not eat me' signaling for an enhanced delivery.[28,100,108] A molecule often associated with cell-derived improved delivery is the integrin CD47, an immunosuppressive signaling molecule. This molecule is commonly overexpressed in cell surface on cancer and red blood cells, which bind to SIRPα and regulates phagocytosis. The interaction with CD47 and SIRPα release the 'do not eat me signal'. The presence of CD47 in nanoparticles is responsible to increase the half-life of the vesicles and homologous targeting in cancer cells.[35] Thus, evaluation of the expression of these protein and understand the 'eat me/don't eat me' approach is a paramount step.[100] Upon understanding how they work can provide solid basis for development of theranostic materials, that combine detection and treatment in a single application.[109]

In this chapter we show the development of AuNRs covered with macrophage-derived EVs and cell membrane nanoparticles and examined their interaction with cancer cell lines. AuNRs were chosen due to their prospects in photothermal therapy application as a theranostic nanomaterials.[53] Our goal was to compare in vitro outcomes of two broadly used cell-derived vesicles when coating AuNRs. Our results suggest the importance of CD47 as the 'do not eat me' signal in the cell membrane-derived nanoparticles being able to reach the tumor cells more efficiently than EVs-based gold nanorods, due to differential fate in their internalization processes. This comparative study has significant advances towards the understanding on the role of EVs in the cellular communication for their use as delivery tools, when compared to classical cell membrane nanoparticles.

3.2 METHODOLOGY

3.2.1 Synthesis of gold nanorods

The synthesis of gold nanorods is based on the seed-mediated growth in the presence of the surfactant cetyltrimethylammonium bromide (CTAB, Sigma Aldrich).[59] First, we prepare the gold seeds by mixing 9.75 mL of 0.1 mol L^{-1} CTAB with 250 µL of 0.01 mol L^{-1} $HAuCl_4$ (Sigma Aldrich) and left under stirring for one minute. Then, 600 µL of cold 0.01 mol L^{-1} $NaBH_4$ (Sigma Aldrich) was added quickly and left under stirring for 10 minutes. This suspension was maintained at 25 ºC for 1.5 hours before being used to release the hydrogen produced in the reduction.

Then, 2 mL of 0.01 mol L^{-1} $HAuCl_4$ was mixed with 36 mL of 0.1 mol L^{-1} CTAB. To the mixture, 120 µL of 0.01 mol L^{-1} $AgNO_3$ (Sigma Aldrich), 800 µL of 1 mol L^{-1} HCl (Synth) and 320 µL of 0.1 mol L^{-1} ascorbic acid (Sigma Aldrich) were added sequentially. Finally, 4 mL of previously prepared gold seeds were added. The system was maintained at room temperature for at least 24 hours and then centrifuged at 1500 g for 5 minutes to remove excess CTAB solid in solution by repeating this process 5 times.

The resulting nanorods were later functionalized with citrate, due to CTAB cytotoxicity for biological studies.[110] For this, 20 mL of CTAB_AuNRs were centrifuged three times (16000 g, 85 minutes), to remove excess of surfactant.

The CTAB_AuNRs pellets were redispersed in 0.15 wt% Na-PSS (Sigma Aldrich) to a final volume of 20 mL and left to stand for at least 2 hours before the next step. This sample was submitted to two centrifugation steps (16000 g, 85 minutes) redispersed in 0.15 wt% of Na-PSS to a final volume of 10 mL. The latter step ensures efficient removal of the CTAB. Finally, the sample was centrifuged with the same parameters established before being redispersed in 20 mL of sodium citrate (Sigma Aldrich) at 5 mmol L^{-1}, keeping at rest for at least 12 hours. The dispersion was subjected to a second cycle of centrifugation, with a final volume of 5 mL dispersed in 5 mmol L^{-1} of sodium citrate. For the functionalization studies, the

NRs were submitted to a third cycle of centrifugation and resuspended in phosphate buffered saline (PBS) 1X.

For viability studies, AuNRs_PEG were produced by the following procedure: after removing the excess of CTAB, PEG-SH (Sigma Aldrich) was added to the gold nanorods dispersion in a final concentration of 200 μmol L^{-1} and sonicated for 30 minutes. The nanoparticles were left overnight in a gentle shaking at room temperature and then centrifuged to remove the excess of free polymer.

3.2.2 Cell lines culture

Macrophage Abelson murine leukemia virus transformed (RAW264.7, American Type Culture Collection, ATCC), healthy fibroblasts (L929, ATCC), rat hepatoma (HTC, BCRJ) and healthy mouse liver (FC3H, BCRJ) cells were cultured in Dulbecco's Modified Eagle Medium (DMEM, Vitrocell, Brazil) supplemented with 10 % (v/v) of fetal bovine serum (FBS, Vitrocell, Brazil), and 1% (v/v) L-Glutamine at 37 °C in a humidified atmosphere with 5% CO_2. Metastatic breast cancer (4T1, from Bank Cell Rio de Janeiro, BCRJ) were cultured in Roswell Park Memorial Institute Medium (RPMI, Vitrocell, Brazil) supplemented with 10 % (v/v) of fetal bovine serum (FBS, Vitrocell, Brazil) at 37 °C in a humidified atmosphere with 5% CO_2.

3.2.3 Extracellular vesicles isolation

RAW264.7 cells were culture in 175 cm^2 flasks (Greiner). After 70% confluence of cells, culture media was replaced by DMEM supplemented with 1% (v/v) L-Glutamine and 10% (v/v) FBS depleted of exosomes (Thermo Fisher Scientific). Cell culture medium was collected between 24 – 48 hours and centrifuged at 800 g for 4 minutes at room temperature to remove detached cells. In order to avoid contamination by larger vesicles, such as apoptotic bodies, supernatant was submitted to filtration with membrane with pore size of 0.22 μm.[111] Filtered supernatant was ultracentrifuged at 100,000 g for 2 hours at 4 °C. The pellet was washed with (PBS) followed by a second ultracentrifugation step at 100,000 g for 2 hours at 4 °C using an Optima MAX-XP ultracentrifuge (Beckman Coulter, TLA 110

rotor). The pellet was collected and resuspended in PBS containing SIGMAFAST™ protease inhibitor cocktail tablets prepared/diluted according to product/manufacturer specifications. For long-term storage the EVs were stored at -80 °C and used within 1 month after isolation.

3.2.4 Cell membrane extraction

RAW264.7 cells in 70% confluence (175 cm^2 flasks), were detached from the flask using a cell scraper and subsequently centrifuged at 800 g for 5 minutes at room temperature. The pellet was centrifuged (800 g, 5 minutes) and washed at least two times/twice with PBS. Then, the pellet was resuspended with hypotonic buffer (10 mM Trisbase, 1.5 mM $MgCl_2$, 10 mM NaCl, pH 6.8, all Sigma Aldrich), and after 5 minutes, sedimentation was performed by centrifugation at 800 g, for 5 minutes, at 4 ºC. The pellet was resuspended in lysis buffer (0.25 M sucrose, 10 mM HEPES, 100 mM succinic acid, 1 mM EDTA, 2 mM $CaCl_2$, 2 mM $MgCl_2$, pH 7.4, all Sigma Aldrich), and the final solution was homogenized 70 times (1400 revolution / minute) in a VIRTUS PII glass homogenizer. The homogenate was centrifuged at 10,000 g, for 20 minutes, at 4 ºC to remove cell debris. Finally, the supernatant was ultracentrifuged at 100,000 g, for 2 hours, at 4ºC, using an Optima MAX-XP ultracentrifuge (Beckman Coulter, TLA 110 rotor). The ultracentrifuged pellet containing the membranes was resuspended in 1x PBS with protease inhibitor cocktail (SIGMAFAST™). For long-term storage the cell membrane extracts were stored at -80 °C and used within 1 month of extraction.[111]

3.2.5 Functionalization of nanoparticles with cell membrane and EVs

After extraction, cell-derived membranes, isolated EVs and gold nanorods were sonicated, separately, in an ultrasonic bath for 15 minutes at 4 ºC at 37 Hz with 80% power (Elmasonic P). For functionalization of the nanoparticles, cell membrane or EVs (100µl, $1x10^{11}$ particles mL^{-1}) were added to 1000 µL of citrate-AuNRs (optical density at 700 nm = 0.4) and sonicated with the same parameters as above. Subsequently, the nanoparticles were extruded 15 times through 200-nm pore polycarbonate membrane (Avanti Lipids) using Avanti mini-Extruder.

In order to study the differences in functionalization of the NRs coating the cellular uptake, extracellular vesicles and cell membranes coated gold nanorods (eAuNRs and mAuNRs, respectively) were labelled with 3,3-Dioctadecyloxacarbocyanine perchlorate (DiO, Sigma Aldrich). The nanoparticles were incubated, after extrusion, for 1 hour at 37 ^{o}C with DiO at 5 μg mL^{-1}, to dye the lipid bilayer of the EVs and cell membranes coating the AuNRs. The samples were dialyzed overnight to remove excess of unbound fluorescent probe. Zeta potential and size distribution (DLS) measurements of all the nanoparticles were performed using Zetasizer Nano ZS, Malvern. The concentration of the vesicles and the nanoparticles was evaluated with nanotracking analysis (NTA), Nanosight NS300, Malvern.

3.2.6 Transmission electron microscopy

For transmission electronic microscopy (TEM), 3 μL or 10 μL of the samples were deposited on copper grids for 60 seconds and dried with filter paper. Samples were stained with 3 μL of 2% uranyl acetate for 30 seconds and again dried with filter paper. CryoTEM, cryogenic transmission samples were prepared by depositing 3 μL of the sample on a copper grid, the excess was dried for 3 seconds with filter paper and the grid was dipped in liquid ethane. The procedure was performed by Vitrobot Mark. The images were obtained in JEOL 1400 and JEM-2100 Transmission Electron Microscopes.

3.2.7 Fourier-transform infrared spectroscopy (FTIR)

Samples were prepared by drop-casting 10 μL of the samples diluted in PBS 1x onto clean silicon substrates and dried under reduced atmosphere. The spectrum was collected using an Infrared spectrometer Nicolet 6700/GRAMS Suite, with 128 scans per sample with 4 cm^{-1} resolution from 4000 to 400 cm^{-1}.

3.2.8 Cell viability

Cell viability was investigated by MTT assay after 24 hours of incubation with the samples. All the cells were seeded at a density of 2x10^{3} cells per well in 96-well

plates and grown for 24 hours. Prior incubation, media was removed and 100 µL of the nanoparticles in different concentrations ($1x10^8$, $5x10^8$, $1x10^9$ and $5x10^9$ particles mL^{-1}) were incubated in DMEM supplemented with 10% (v/v) FBS were added to each well. For 4T1 the nanoparticles were resuspendend in RPMI 10% FBS. After 24 or 48 hours, the nanoparticles were removed, cells were washed with 1X PBS and 100 µL at 0.5 mg mL^{-1} 3-(4,5-dimethylthiazol-2-yl)-2,5-diphenyltetrazolium bromide (MTT, Sigma) was incubated for 3 hours. Further, formazan crystals were dissolved in 100 µL of dimethyl sulfoxide (DMSO, Synth) per well and left under orbital agitation for at least 15 minutes. Measurements were performed at 570 and 630 nm using a microplate reader SpectraMax M3 (Molecular Devices). Cell viability was calculated compared to controls without treatment as described in Equation 1.

$$cell\ viability\ (\%) = \frac{\left(A_{570sample} - A_{630sample}\right)}{A_{570control} - A_{630control}}\ x\ 100 \qquad (3.1)$$

where $A_{570sample}$ is the absorbance at 570 nm and $A_{630sample}$ at 630 nm of treated samples, while $A_{570control}$ and $A_{630control}$ represent the absorbance of non-treated samples or controls. Data analysis was performed using Origin 2020.

3.2.9 Reactive Oxygen Species (ROS) assays

Reactive oxygen species (ROS) assay was done using 2',7'-dichlorodihydrofluorescein diacetate (H_2DCFDA) as a probe. In 96-well plates, $2x10^3$ cells per well were seeded for 24 hours. After, eAuNRs and mAuNRs were incubated for 24 hours at two concentrations ($1x10^8$ and $5x10^8$ particles mL^{-1}). Positive control was H_2O_2 (Synth) at 100µM and incubated 1 hours before the final 24 hours. Cells were rinsed with PBS and incubated with 50 µM of H_2DCFDA in cell culture media for 1 hour at 37 °C with 5% CO_2. The fluorescence was measured at excitation wavelengths of 485 nm and emission at 530 nm using a microplate reader SpectraMax M3, after washing and adding the cells with PBS (Molecular Devices). The fluorescence intensity values were normalized by the ROS from the control.

3.2.10 Cellular uptake studies

3.2.10.1 Image Xpress

In 96-well plates, $5x10^3$ cells per well (RAW264.7, 4T1 and L929) were seeded and grown for 24 hours. Medium was removed, followed by the incubation of 100 µL per well of $1x10^8$ particles mL^{-1} eAuNRs or mAuNRs (containing DiO as the fluorescent probe) for 4 hours. For inhibition studies, the agents: amiloride (100 µg mL^{-1}), nystatin (40 µg mL^{-1}), nocodazole (10 µg mL^{-1}), hydroxy-dynasore (100 µmol L^{-1}) and dansyl-cadaverine (100 µmol L^{-1}) (all Sigma Aldrich) were incubated for 30 minutes prior incubation of the nanoparticles and not removed during the nanoparticle's incubation. After incubation, cells were washed with PBS twice, fixed with 3.7% paraformaldehyde (PFA) for 10 minutes and washed again 3x with PBS. 2% (w/v) of bovine serum albumin (BSA) were added for 15 minutes. Cells were them washed 3X with PBS and incubated with 4',6-diamidino-2-phenylindole dihydrochloride (DAPI, 100µL at 2 µg mL^{-1}) for 10 minutes. The samples were washed with PBS followed with one wash with distilled water. For the measurements the cells were immerged in 100 µL of PBS.

3.2.10.2 Confocal laser scanning microscopy

RAW264.7 and 4T1 internalization of eAuNRs and mAuNRs was observed using a confocal laser scanning microscopy (CLSM). Cells were incubated in glass slides, using 24-well plate as support, at initial seeding of $5x10^4$ cells per well and grown for 24 hours. Cells were incubated with 50 µL of nanoparticles from stock solution in 500 µL for 4 hours. LysoTracker™ Deep Red (Thermo Fisher) was incubated at 75 nmol L^{-1} for one hour prior to end of the incubation of the nanoparticles. The cells were washed twice with 1X PBS and fixed with 3.7% PFA for 10 minutes. Prior to the incubation with 2 %(w/v) of BSA the cells were washed twice with PBS and then incubated for 15 minutes. DAPI was incubated at 2 µg mL^{-1} for 10 minutes, and then the slides were washed with PBS followed by distilled water.

Slides were mounted with Fluoroshield. Image acquisition was performed on Zeiss (LSM780) confocal microscope with water immersion, and analyzed using Image J.

3.2.10.3 Inductively coupled plasma mass spectrometry (ICP-MS)

RAW264.7 and 4T1 internalization of the nanoparticles were also evaluated with ICP-MS. In 12-well plate, cells were seeded at $1x10^5$ cells per well. After 24 hours, 1 mL of $5x10^8$ particles mL^{-1} in DMEM and RPMI with 10% FBS and were incubated for 4 hours. Following the incubation, the medium containing the particles was removed, cells were washed twice with PBS and trypsinized or scraped. Cells were centrifuged at 800 g for 5 minutes, resuspended in PBS and the cell concentration was evaluated with trypan blue exclusion test. Cells were again centrifuged (800 g, 5 min) and each pellet was dissolved with 500 µL of aqua regia and further diluted in 10 mL of deionized water. Finally, the samples were analyzed as received by LabExata using NexIon 2000 from Perkin Elmer.

3.2.11 Western Blot

Samples (10 µL and using $6x10^8$ particles mL^{-1}) were mixed with Laemmli sample buffer, boiled at 100 °C for 5 minutes, diluted in sample buffer, loaded onto 8% acrylamide gels and run at 100 V for approximately 1.5 hours. Gels were transferred to nitrocellulose membranes (0.45 µm, Biorad) and blocked with 5% (w/v) bovine serum albumin (BSA) in Tris-buffered saline with 0.05% (v/v) Tween 20 (TBS-T) for 1-2 hours. For identification of proteins, membranes were probed with primary antibodies anti-flotilin 1 (1:1000, BD, 610821), anti-CD47 (1:1000, Thermo Fischer PA5-81591) and anti-annexin 2 (1:1000, Sigma Aldrich QC5535), anti-ALIX (1:1000, Abcam Ab186429) and incubated overnight at 4 °C. Further, membranes were washed with TBS-T for four times (5 minutes each), and secondary antibodies were added and detected by enhanced chemoluminescence (ECL, Thermo Scientific, 32106 and 34095). For the cell lysate the cells were incubated $2x10^6$ cells per well. After 24 hours, the cells were washed twice with 1X PBS. The cells lysate was performed by adding 15 µL of lysis buffer per 10^6 cells on ice and let it rest for 2

hours. Finally, the lysate were centrifuged (10,000g, 4 °C) for 10 minutes and the supernatant was collected. Images of membranes were acquired on a molecular imager (ChemidocTM XRS; Biorad).

3.3 RESULTS AND DISCUSSION

The use of the macrophage-derived vesicles to recover nanoparticles lies in the advantage of biorecognition and protein profile to camouflage, facilitating its delivery to the target cancer cells.[112-113]

3.3.1. Extracellular vesicles and cell membrane characterization

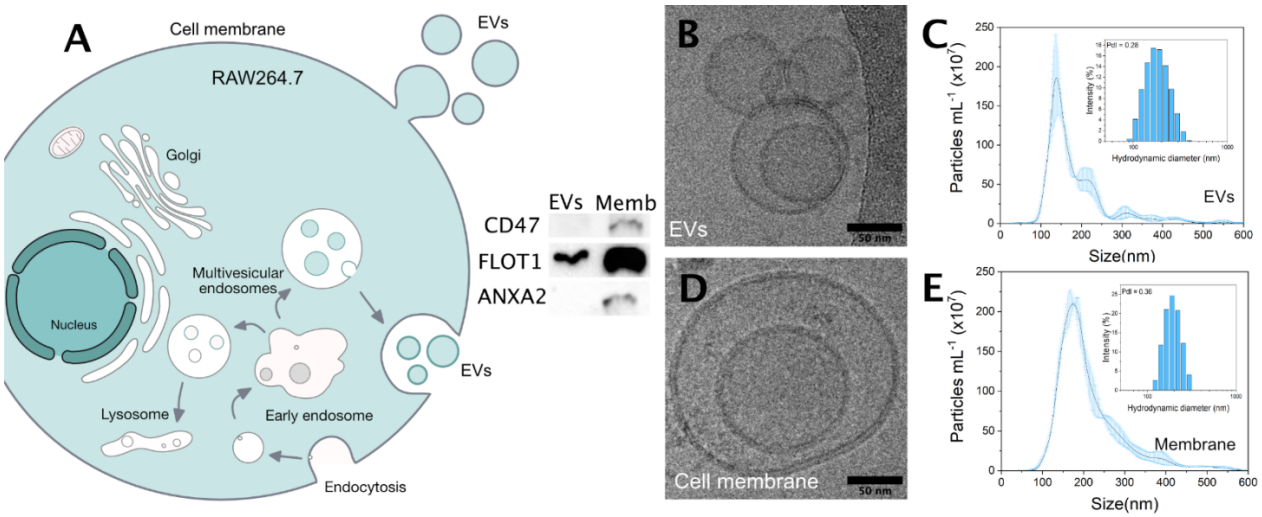

Figure 3.1 - Characterization of extracellular vesicles and membrane extract from RAW264.7 macrophages. A) Schematic of the biogenesis of EVs and Western blot analysis using anti-CD47, anti-Flotilin 1(FLOT1) and anti-Annexin 2 (ANXA2). Extracellular vesicles isolated from RAW264.7 by filtration and ultracentrifugation steps characterized by B) Cryo-TEM and C) NTA and DLS. Cell membrane extract from RAW264.7 obtained by hypotonic lysis combined with mechanical membrane disruption and ultracentrifugation were also characterized by D) Cryo-TEM and E) NTA and DLS. Scale bar: 50 nm.

Source: By the author.

EVs obtained by filtration and differential ultracentrifugation and cell membrane extract obtained by ultracentrifugation were characterized by Western Blot, Cryo-TEM, NTA and DLS (Figure 1). Protein content of EVs and membrane extract were evaluated by Western Blot to identify the presence of CD47, flotillin 1 and annexin 2 (Figure 1.A). CD47 and Annexin 2 were detected only in cell membranes. Additionally, flotillin 1 was present in both vesicles of the macrophages.

Comparing the expression levels, we highlight the presence of CD47 only in the cell membrane extract. CD47 tetraspanin is a cell surface receptor present in the membrane of tumor cells that modulates immune response and inhibits phagocytosis by immune system cells.[36,114] Its absence in EVs is related with its endosomal biogenesis, in which there is an inversion of the lipid bilayer and alteration of the expressed proteins.[115] Flotillin 1 has a crucial role in the production of EVs and is widely explored as EV marker,[33] therefore, we have the expression in the cell extracts and in the EVs.[116] Annexin 2 shows residual cytoplasmatic molecules in the cell membrane vesicles as expected, due to the protocol of isolation by hypotonic and lysis buffer.[117] Iatroscan analysis showed differences in lipid composition, where there is an enrichment in the phospholipid in the cell membrane when compared to the EVs, implying that the majority of the EVs are from endosomal biogenesis (Figure S3.1, Appendix A).[118-119]

Figure 3.1.B shows Cryo-TEM images of EVs isolated from RAW264.7 in which clear lipid bilayers can be observed within a size range with mean of 145.1 ± 37.5 nm, according to NTA and DLS measurements (Figure 3.1.C). Likewise, Figure 3.3.D displays bilayers vesicles obtained from RAW264.7 membrane extracts and their size distribution with NTA of 233 ± 16.8 nm also similar to DLS (Figure 3.3.E). These results showed that the UC does not changed their vesicular characteristic. Particle concentration measured in NTA for isolated EVs and cell membrane extract, was (2.1 ± 1.2)x10^{11} and (1.2 ± 1.1)x10^{11} particles mL^{-1}, respectively, in which indicates a high yield isolation for both vesicles.

3.3.2 eAuNRs and mAuNRs characterization

After vesicles extraction, the gold nanorods were functionalized by extrusion using 200-nm pore size membranes as schematic of Figure 3.2A. Fabrication of functionalized gold nanorods by extrusion was successful to set the gold NRs within the vesicles. This strategy is an elegant way to improve the performance of gold nanorods, considering its “camouflage” by cell-derived nanoplatform (See in Appendix A, Figure S3.2).[53] The quality assurance of functionalized nanoparticles was accessed by an extensive analytical characterization.

Firstly, UV-Vis spectra (Figure 3.2B) showed that the properties of functionalized nanorods changed upon their functionalization with EVs (eAuNRs) and membranes (mAuNRs). The spectra shows a typical absorbance curve for AuNRs, with a band around 520 nm and other between far-red and near-infrared region. For the functionalized NRs, there was a decrease in absorption spectra. Both, eAuNRs and mAuNRs presented a shift towards the red wavelength in the presence of the vesicles due to changes in the dielectric nature around nanorods.[120] In particular for mAuNRs, we observe a major decrease in the longitudinal peak that are not related due to loses during the synthesis once their gold content is similar from both particles (Figure S3.3, Appendix A), this is related to the gold nanorods assembly too close within the vesicles, in which we have the plasmon coupling effect.[53]

DLS and NTA measurements showed an increase in size for the rods functionalized with the vesicles (Figure 3.2.C) and a decrease in the concentration when compared to the isolated vesicles (Figure S3.3, Appendix A). Figure 3.2.C showed a size of 177.9 ± 19.3 nm for eAuNRs and 149.5 ± 9 nm for mAuNRs values close to polycarbonate membrane used in extrusion. Polydispersity indexes were 0.46 ± 0.14 for eAuNRs and 0.32 ± 0.07 for mAuNRs. The nanoparticles concentration measured by NTA is only possible, due to low aspect ratio of 3.4 and their width below the detection limits of the equipment.[121] NTA analysis showed a concentration of $1.4x10^{11} \pm 1.6x10^{10}$ and $3.4x10^{11} \pm 5x10^{10}$ particles mL^{-1} for eAuNRs and mAuNRs, respectively. The AuNRs coated with EVs are mostly covered individually and their width are less than 5 nm, which is not detectable by the equipment. For the case of mAuNRs this extrapolation is related to the assemble of nanorods inside the membrane that behaves as a larger spherical particle. NRs displayed zeta potential values of -37.5 ± 3.8 mV that shifted to -16.4 ± 2.4 mV for the eAuNRs and to -18 ± 1 mV for the mAuNRs, values close to the values of isolated membranes (-27.3 ± 2 mV) and EVs (-20.7 ± 2 mV), indicating the successful functionalization (Figure3. 2.D).

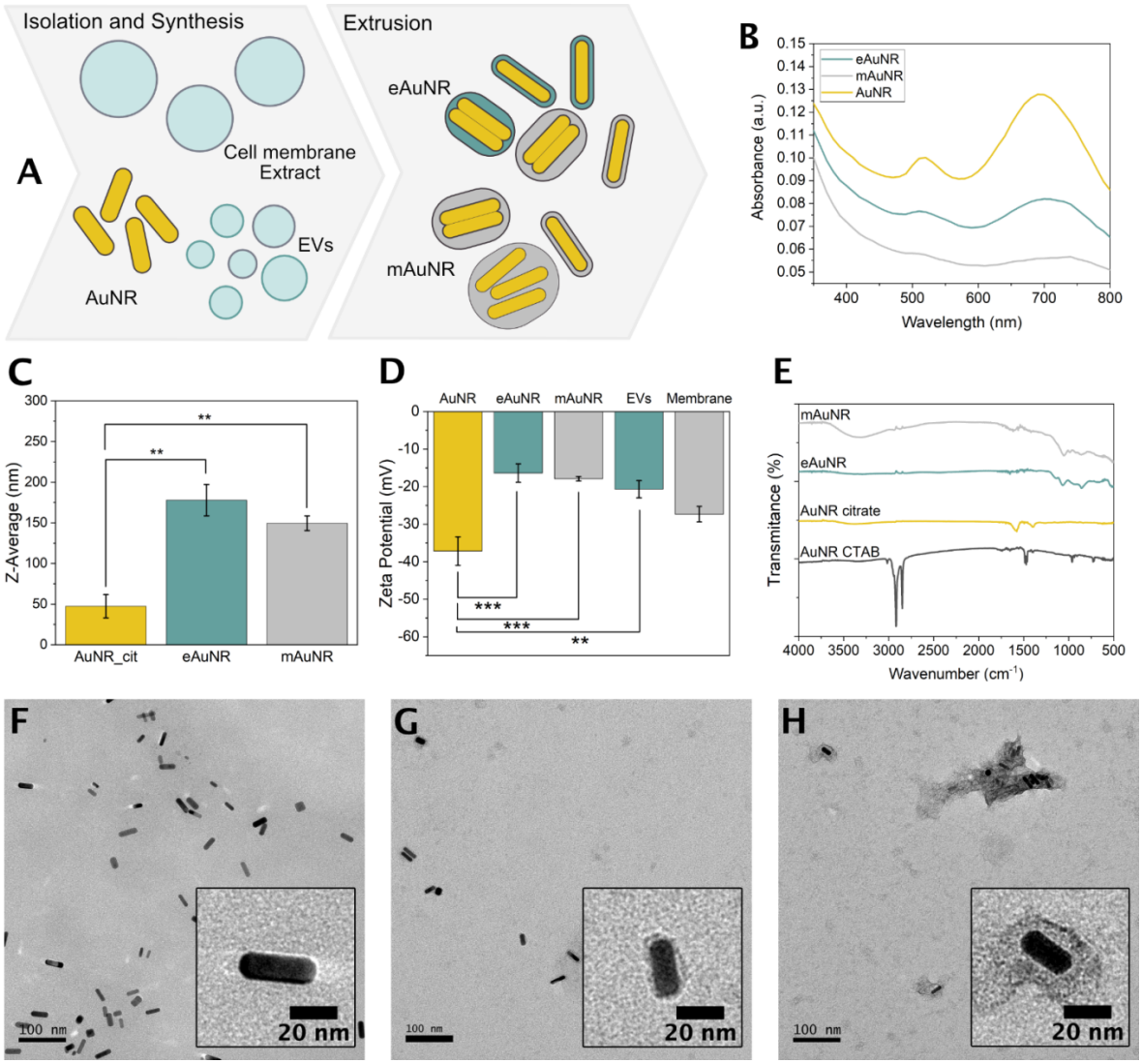

Figure 3.2 - Characterization of gold nanorods coated with cell membrane (mAuNRs) and extracellular vesicles (eAuNR) by extrusion with a 200 nm pore size membrane. A) Schematic view of the functionalization that resulted different protein and lipids pattern at nanoparticles surface. B) UV-Vis spectra, C) Z-average analysis in one-way ANOVA with Tukey's comparisons with three independent syntheses, D) zeta potential, and E) FTIR spectra of eAuNRs and mAuNRs. TEM images with negative staining of F) AuNR citrate G) eAuNRs and H) mAuNRs. Scale bar: 100 nm and 20 nm (The measurements are represented by average and error bars represent the standard error of three independent synthesis, *p<0.05; **p<0.01; ***p<0.001).

Source: By the author.

Figure 3.2E shows FTIR analysis of the AuNRs associated with the start material CTAB (AuNRs_CTAB), citrate (AuNRs_cit), EVs (eAuNRs) and cell membrane extract (mAuNRs). CTAB exchange to sodium citrate can be confirmed by the decrease of the two intense bands at 3000 and 2800 cm^{-1} that correspond to the symmetric and asymmetric stretching of the methylene chains present in CTAB structure. Additionally, the presence of two bands around 1500 cm^{-1}, correlated to the

stretching of carboxylate groups, confirms the presence of citrate (AuNRs citrate). After extrusion of AuNRs with EVs and cell-derived membranes, the infrared spectra showed bands between the range of 1500 and 1350 cm^{-1} that correspond to the deformation modes of CH_2 and CH_3 from lipids. Around 1700-1500 cm^{-1} we observed peaks corresponding to amide I and II bands. A band in 3400 cm^{-1} was found more prominent in mAuNRs sample, that is related to the presence of -OH groups. This might be related of the hydration level of the membrane, which the samples were prepared to minimize free water spectrum influence.[122]

eAuNRs and mAuNRs showed differences when between 1500 and 1350 cm^{-1}, 1700-1500 cm^{-1} and 3400 cm^{-1} characteristics of lipids, proteins and hydration respectively. The last band is more intense in mAuNR might be related of the hydration level of the membrane, which the samples were prepared to minimize this.[122] Also this band might be related to lipid stretching direct dependent on the lipid composition of the vesicles, where the cell membrane is enriched with phospholipids (Figure S3.1, see in Appendix A) allowing this movement.[123]

To better investigated the morphology and size, nanomaterials were evaluated by TEM, using negative staining (Figures 3.2F-H). As shown in TEM images of the functionalized NRs (Figure 3.2G and 3.2H), there is a visible layer surrounding the rods in both systems. mAuNRs TEM images reveal more AuNRs assembled together with irregular shape, when compared with the eAuNRs images that shows a more individual coating. The assemble of the gold nanorods when functionalized with cell membrane in the TEM images, confirms the plasmonic effects observed in Figure 3.2B.

3.3.3 Toxicity studies of eAuNR and mAuNR

In vitro studies were performed to analyze the effect of different functionalization of the AuNRs on the cell viability. Cell viability of three cellular types, macrophage-like cells (RAW 264.7), breast tumor cell (4T1) and fibroblasts (L929), was assessed by MTT assay with 24 hours incubation (Figure 3.3). mAuNRs, eAuNR sand citrate showed high toxicity in the source cell (Figure 3.3A). AuNRs_PEG showed no reduction in viability based on the fact that PEG prevents identification by cells of immune system.[95] The high toxicity is related to the intrinsic characteristic of

macrophages to internalize more nanoparticles, that can be tuned for biomedical applications.[97]

In the case of 4T1, the results for 24 hours incubation showed a statistical difference between AuNRs_cit and AuNRs_PEG (Figure 3.3B), with an increase in the mitochondrial activity for citrate AuNR. The cell viability of metastatic breast cancer cell did not reduced with the cell-derived nanoplatforms and the only difference was an increase in the mitochondrial activity when incubated with AuNR citrate, as a result of citrate being a central part of the biochemistry pathway in cells energy production, and highly used in tumor cells for rapid growth.[124] All the formulations showed no statistically significant reduction in viability of L929 fibroblasts, only a tendency of mAuNRs to decrease sightly the viability (Figure 3.3C).

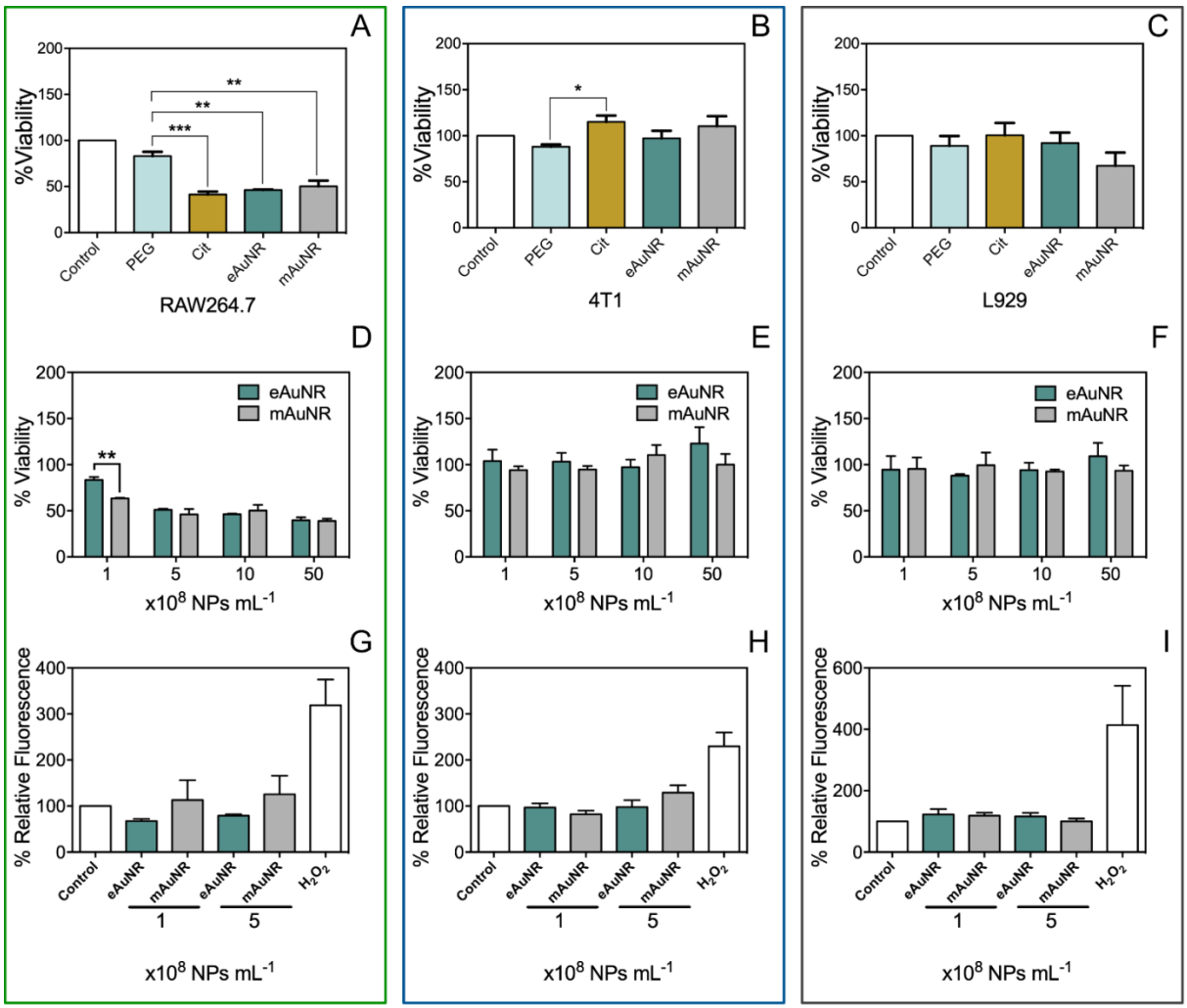

Figure 3.3 - Toxicity studies of the nanoparticles in source, metastatic cancer and healthy cell lines. Cell viability of A) RAW 264.7 (green, n=3), B) 4T1 (blue, n=3) and C) L929 (black, n=3) of 24 hours by MTT of the nanomaterials functionalized with PEG, citrate, EVs and cell membrane at a concentration of $1x10^9$ particles mL^{-1}. MTT viability assay of the nanomaterials functionalized with exosomes and membrane varying the concentrations from $1x10^8$ to $5x10^9$ particles mL^{-1} for D) RAW264.7, E) 4T1 and F) L929. ROS studies to evaluate, at the 2 lowest concentrations, the stress caused by the rods in all the G) source, H) cancer and I) healthy cell lines. (Statistical analysis in one-way ANOVA with Tukey's comparisons, MTT measurements are represented by average and error bars represent the standard error, ROS measurements are represented the average normalized with the control and error bar by standard error, * $p<0.05$; ** $p<0.01$; *** $p<0.001$).

Source: By the author.

Concentration-dependent assays were performed to analyze differences between the groups eAuNRs and mAuNRs. For RAW264.7 cells, at the lowest concentration of $1x10^8$ particles mL^{-1}, mAuNR caused a higher toxicity when compared with eAuNR (Figure 3.3D), an indicative of different pathways in uptake.[125] The higher concentrations of both nanomaterials decreased the viability

approximately in 50%. 4T1 and L929 (Figures 3.3E and 3.3F) viability was not affected by either concentration or functionalization changes.

Intracellular ROS detection, using $1x10^8$ particles mL^{-1} and $5x10^8$ particles mL^{-1} of nanoparticles showed that there was no oxidative stress in all cells (RAW 264.7, 4T1 and L929) upon treatment with nanorods functionalized with PEG, citrate, EVs or cell membrane (Figure 3.G-I). Some cells when exposed to gold nanorods only increase ROS production because of irradiation and photothermal therapy.[53,126] Finally, all the nanorods were also not toxic for the cancerous and non-cancerous hepatic cell lines and uptake studies showed low internalization rates for both cell lines (Figures S3.4 and S3.5, Appendix A).

3.3 Cellular uptake assays

To elucidate the coating differences (EVs, cell membranes) that could be responsible for different toxicity profile amongst cell lines, endocytosis mechanisms were assessed by pharmacological inhibitors of the main endocytic pathways of nanoparticles (Figure 3.4). Cellular uptake was investigated using fluorescence-based techniques, the nanoparticles were labelled with DiO, a fluorescent probe that internalizes in the lipid bilayer of the vesicles. As uptake inhibitors we used nystatin, amiloride, hydroxi-dynasore, nocodazole and dansyl-cadaverine inhibits caveolae, macropynocitosis, dynamin, microtubules and clathrin-dependent endocytosis, respectively.

For eAuNRs (Figures 3.4A-C), the internalization was driven by dynamin-dependent endocytosis independent by cell type.[127] This endocytic pathway is mediated by several cell surface receptors for example heparan sulfate proteglycan and galectin-5.[127-128]

For RAW264.7 cells, by inhibiting the clathrin-dependent endocytosis (Figure 3.4A), the uptake of the eAuNRs increased, showing a cross-regulation between the endocytic mechanisms.[129] Additionally, eAuNRss interacted more with the source in comparison to other cell lines. Figure 3.4E, showed the mAuNR endocytosis in the source cell was driven by macropinocytosis, dynamin and microtubules pathways, related to amiloride, hydroxy-dynasore and nocodazole inhibitors, respectively. Clathrin-dependent inhibition slightly increased for this mAuNRs as a cross-

regulation mechanism from the macrophage to compensate the deformations in the cell membrane.[129]

In particular for metastatic breast cancer cells (Figure 3.4B), macropinocytosis was also shown to be an important endocytosis pathway for eAuNR.[130] Importantly, the internalization of these mAuNRs by 4T1 cells (Figure 3.4F) suggested other endocytic pathway.[131] The healthy cell line endocytoses the eANR and mAuNR via dynamin and clathrin-depended, respectively (Figure 3.4C-G).

Pathways differences can be explained by the differences in protein expression in cells (Figure 3.4D). The main difference between the nanoparticles analyzed is the lack of expression of CD47, the 'do not eat me' signaling in the EVs, which corroborates to the increased uptake of the eAuNRs by the macrophage source cell.[100] Another interesting result obtained in Western Blot is the high expression of CD47 in 4T1, in comparison to the other cell lines. This results is in agreement to the tetraspanin driven pathway to internalize mAuNRs, as a homotypic cell adhesion, which has been shown to be dependent on actin filaments.[131] This homotypic adhesion is one of the mechanism of metastatic tumor development and commonly used in cell membrane nanoparticles.[39,132-133] ALIX expression in cells is known to preferentially characterize internalization of molecules via a clathrin independent endocytosis.[134] Additionally, this marker is used as characterization for small EVs because it is related to endosomal pathways.[33] In our inhibition assays, the clathrin-mediated endocytosis only accounts for a small portion of internalization in L929 for mAuNRs, and ALIX expression is similar for all cell lysates.

ICP-MS analysis (Figure 3.4H) showed that the functionalization of gold nanorods with the vesicles decreased the uptake by the macrophages at the same nanoparticles concentration, however no statistical differences were observed between eAuNRs and mAuNRs.[135] These results corroborates to the viability assay and at concentrations above $5x10^8$ particles mL^{-1} the toxicity is the same once it delivers the same concentration of gold.

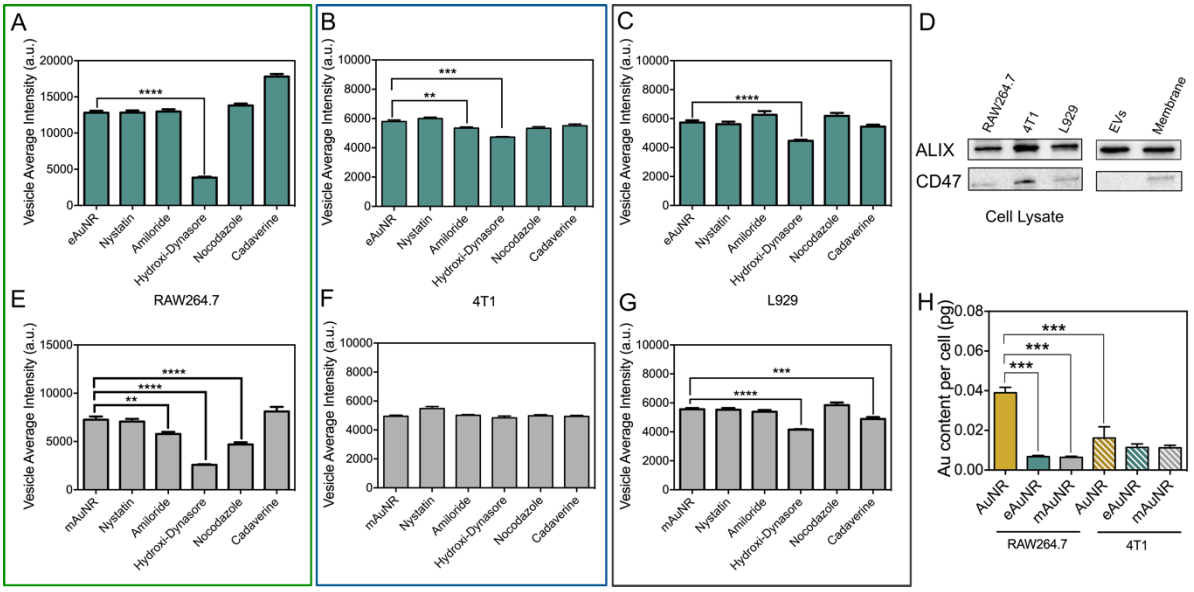

Figure 3.4 - Cellular uptake analysis of the eAuNRs and mAuNRs. Endocytosis studies of eAuNR at $1x10^8$ particles mL^{-1} labelled with DiO after 4 hours incubation with A) RAW264.7 (green, n=3), B)4T1 (blue, n=3) and C) L929 (black, n=3) cells at 37 °C in atmosphere with 5% CO_2. Internalization studies mAuNR at $1x10^8$ particles mL^{-1} also labelled with DiO after 4 hours incubation with E) RAW264.7 (green, n=3), F) 4T1 (blue, n=3) and G) L929 (black, n=3) cells at 37 °C in atmosphere with 5% CO_2. The concentration used for amiloride, nystatin, nocodazole, hydroxi-dynasore and cadaverine, were 100 μg mL^{-1}, 40 μg mL^{-1}, 10 μg mL^{-1}, 100 μmol L^{-1}, 100 μmol L^{-1} respectively. D) Protein content of EVs and membrane extract with cell lysates by Western Blot to identify the presence of CD47 and ALIX. H) ICP-MS internalization analysis by gold content in RAW264.7 and 4T1 incubating the nanoparticles at $5x10^8$ particles mL^{-1} for 4 hours (Statistical analysis in one-way ANOVA with Tukey's comparisons, measurements are represented by average and error bars represent the standard error, * $p<0.05$; ** $p<0.01$; *** $p<0.001$; **** $p<0.0001$).

Source: By the author.

Internalization studies were done by confocal laser scanning microscopy (Figure 3.5). eAuNRs and mAuNRs were incubated with RAW264.7 and 4T1 cells at the same initial fluorescence intensity per well, for 4 hours. Confocal analysis showed that AuNR are capable to internalize (Figures S3.8 and S3.9). The images show a preferential uptake of eAuNRs rather than mAuNRs in the source cell, and the opposite occurs when comparing the nanoparticles in the breast cancer cell line. In 4T1 we observe an increased uptake of mAuNRs than eAuNRs and a tendency to colocalize with Lysotracker, also shown in Figure 3.5.

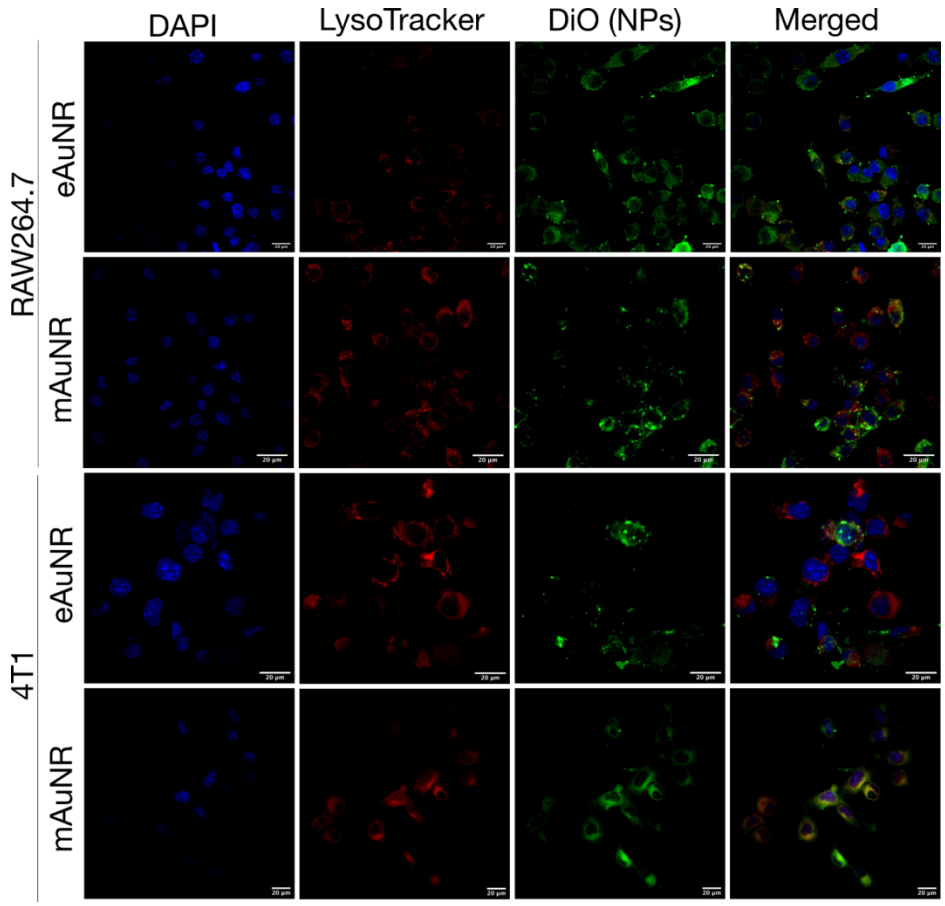

Figure 3.5 - Cellular uptake analysis by confocal laser scanning microscopy of RAW264.7 and 4T1 treated with eAuNR and mAuNR with DiO at the same initial fluorescence intensity for 4 hours. The images were taken with a 60x water immersion objective lens.
Source: By the author.

Several studies indicate that EVs play a role in the microenvironment of tumour[113,136-137] and are shown to be useful tool for drug delivery.[101,137] Also, cell membrane nanoparticles have been extensively reported to be an excellent delivery tool to active target the tumor site. However, no article so far has compared these coatings to evaluate which is better to cancer therapy. The presence of CD47, indeed, proved to be a crucial marker for the main difference observed in the uptake assays.

These differences are related to the switch on of the CD47-SIRPα present in mAuNRs for ‘do not eat me’ in macrophages and ‘eat me’ for metastatic tumor cells by homotypic binding (Figure 3.6).[100] Another important difference between the vesicles is their lipid content, that might contribute to the results, once a similar comparative study showed that delivery from microvesicles was better than from EVs. These microvesicles are cell membrane released particles, with the same

characteristcs as a cell membrane extract. Their biogenesis by plasma membrane vesicles release, with the same content as the cell membrane extract. In this study the expression of CD47 was not evaluated.[27] A previous study has evaluated EVs from different source cells, and showed the differences in the CD47 expression as it happened in our study and *in vitro* results showed the switch on and off from CD47. [100] However, the authors did not evaluate the lipid content differences between the samples.[100] In a cancer microenvironment, cell membrane vesicles interacted more with tumoral cells than the EVs, however, the gold content delivery did not changed probing that they have differential fate which might lead to the same outcome in toxicity studies. These results have significant implications to better understand the role of EVs in cellular communication and to develop efficient EVs as coatings for gold nanorods in cancer therapy.

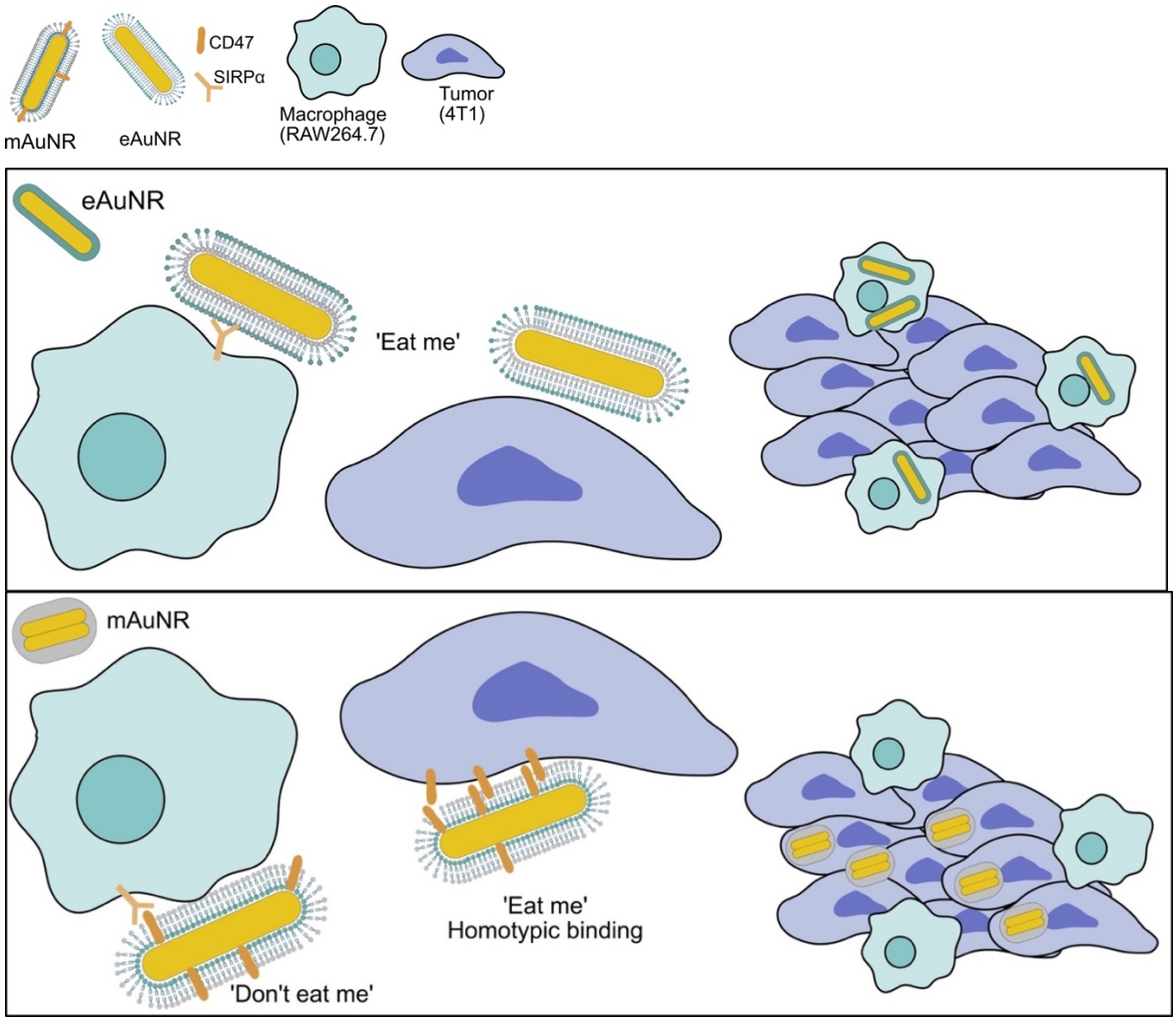

Figure 3.6 – Schematic of internalization pathway and differences in the eAuNR and mAuNR interaction for cancer treatment.

Source: By the author.

3.5 CONCLUSIONS

Here we developed successfully theranostic nanomaterials using gold nanorods coated with extracellular vesicles and cell membranes from macrophages. Several characterization techniques were employed to evaluate their differences. Lipid content analyses showed that eAuNRs have less phospholipids than mAuNRs. Protein expression levels revealed the absence of CD47, a ‘do not eat me’ signal for immune cells, in eAuNRs. Their interactions with *in vitro* models were evaluated using cells from tumor microenvironment. Viability results showed a higher toxicity of eAuNRs and mAuNRs with the source cell, and almost absence toxicity for the breast metastatic cancer and the fibroblast cells. For all cell lines, intracellular ROS was not significant. Uptake studies results revealed differences of viabilities, showing that eAuNRs had an increased internalization for RAW264.7 while the mAuNRs were more internalized in 4T1, related to CD47 expression levels in cells and in the nanoparticles. Cellular uptake of eAuNRs was driven mainly by dynamin dependent in all cell lines. Internalization pathways of mAuNRs differed between cells and showed that the CD47 played an important role in the internalization pathway probably driven by tetraspanin for the metastatic cell line. Our results contribute to a better understanding of the use of EVs in cancer therapy and how are their performance when compared to a classical cell membrane nanoparticle. To the best of our knowledge, this is the first study that compares two commonly used cell-derived coatings and shows that, for cancer therapy, cell membrane coating outperform the EVs-coating gold nanorods, interacting more with metastatic cancer cell.

4 PACLITAXEL ENCAPSULATED IN POLYMERIC NANOPARTICLES AND COATED WITH METASTATIC CELL MEMBRANE VESICLES

4.1 INTRODUCTION

Breast cancer is the most diagnosticated cancer among women and accounts for 25% of cancer deaths.[2-3] Up 30% of women diagnosed in earlier stages develop metastasis.[4-5] Despite the advances in traditional treatments (chemotherapy and radiotherapy), the main problem is still poor selectivity.[140] Among the current treatments, paclitaxel (PTX) the main promise for the treatment of solid tumors, and commonly indicated to breast and ovarian carcinomas.[141] The mechanism of action of PTX is the inhibition of the cell replication by disrupting the microtubules system in phases G_2 and M of the cell cycle.[142] Although PTX is widely used, the drug suffers with the poor selectivity, low water solubility and poor intestinal permeability, besides it might cause anaphylactic reactions due to their intravenous administration using a mixture of alcohol and oil to improve biodistribution.[141,143]

Among the innumerous nanoplatforms, that have been used for drug delivery, poly lactic-co-glycolic acid (PLGA) nanocarriers (NCs) are a well-known delivery system for their biocompatibility, biodegradability and versatility.[144] Additionally, they had been already approved to use by the US Food and Drug Administration (FDA).[145] However, the EPR effect advantage relies on the vascularization of the tumor, which hinders the treatment of unvascularized metastatic cells clusters.[138] Thus, the development of NCs to target the primary and second sites of the tumor is crucial.[133]

Cell membrane-based NCs are an emerging platform for the active drug delivery.[23] The advantage of these NCs is to inherit cell properties and prolong the circulation time.[20] Cancer cell membrane-coated NCs inherit the endothelium-targeting by heterotypic binding and homotypic binding of the adhesion molecules, conferring the NCs to reach distant sites.[146] Adhesion molecules already recognized by the homotypic interaction are epithelial-cadherin (E-cadherin), Thomsen-Friedenreich Antigen and epithelial adhesion molecule (EpCAM).[146-148] Additionally, tetraspanin CD47 overexpressed in cancer cells also contribute to the escape from the immune system and to the homotypic binding.[100] Recently, our research group used pancreatic cancer cell membrane nanoparticles to encapsulate PTX and

gemcitabine for a synergistic treatment of pancreatic cancer.[97] Results showed the importance of combined drugs, and the nanoparticles showed higher efficacy for cancer treatment when compared to the free drugs.[97]

Studies on cell membrane-nanoparticles often investigate their homotypic binding in epithelial cells.[24,133,149] Cancer cells develop a beneficial microenvironment for their development and proliferation, from polarized macrophages to cancer associated fibroblasts.[150] So far, few studies investigated cell membrane-coated NCs interaction with stroma cells.[22,151] Further studies are needed to understand the role of homotypic and heterotypic binding of cell membrane-based NCs in the cancer microenvironment.

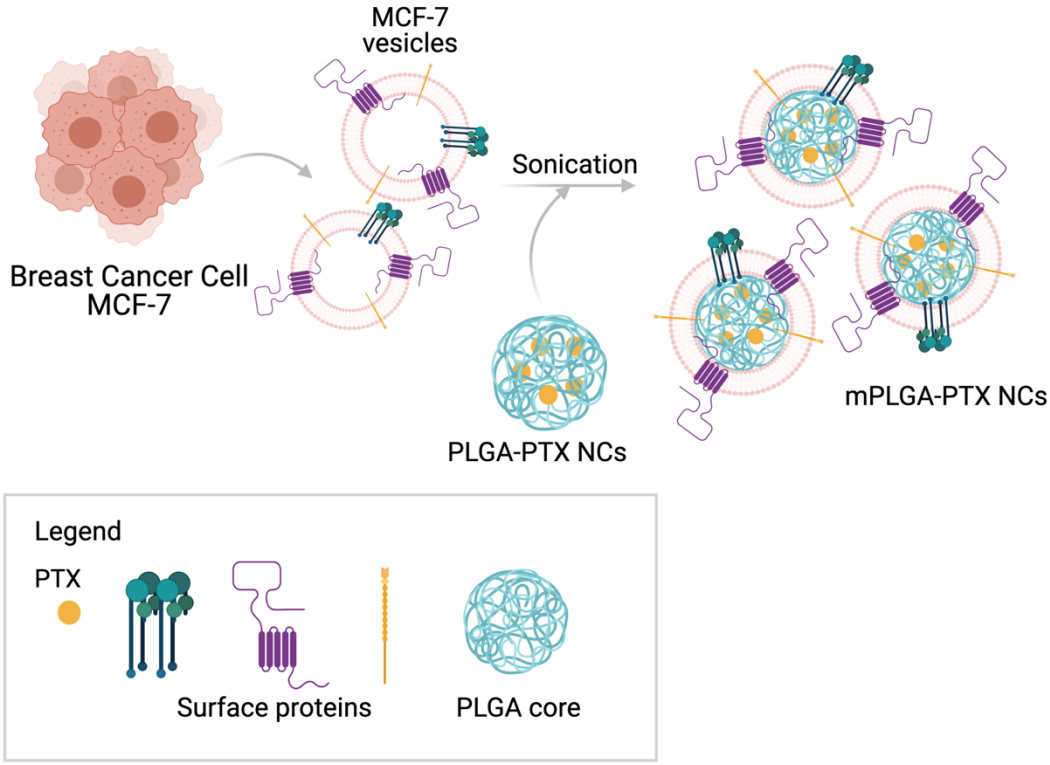

Figure 4.1 - Schematic representation for the fabrication of metastatic cancer cell membrane-coated PLGA-PTX NCs (mPLGA-PTX NCs). MCF-7 cell membrane was obtained by hypotonic lysis to remove intracellular content and isolated by ultracentrifugation. PLGA-PTX NCs were synthesized by nanoprecipitation. The functionalization of the NCs were performed by sonication for 15 minutes (80% of power, 37 Hz).
Source: By the author created with biorender.com.

In this chapter we report the functionalization of PLGA NCs containing PTX, with cell membrane derived from an invasive breast ductal carcinoma (MCF-7, as seen in Figure 4.1). Internalization studies, using dye-loaded PLGA and membrane-

coated dye-loaded PLGA NCs (mPLGA NCs) revealed higher levels of interaction of mPLGA NCs for cancerous and non-cancerous epithelial cells lines. Toxicity studies showed that mPLGA-PTX NCs improved NCs specificity and efficacy against the breast cancer cell, however, it was not effective against lung cancer and non-tumorigenic breast cell lines. Also, mPLGA-PTX NCs highly interacted with human dermal fibroblasts probing to be more toxic than free PTX.

4.2 METHODOLOGY

4.2.1 Synthesis of PLGA nanocarriers

PLGA nanocarriers were synthesized by the nanoprecipitation method with solvent evaporation.[152] Shortly, 160 µL of PTX (0.8 mg, 5 mg mL^{-1}) in acetonitrile was added in 2 mL of 10 mg mL^{-1} PLGA solution (acid terminated Resomer 503H 50:50 MW 24000-38000, Sigma-Aldrich) in acetone and it was kept under magnetic stirring at room temperature. In sequence, 6 mL of Pluronic-F127 (10 mg mL^{-1}, Sigma-Aldrich) was added at once to the previous solution (organic phase) still under magnetic stirring. After 5 minutes of magnetic stirring, acetone was evaporated in a desiccator. The NCs were centrifuged (10,000 g, 20 minutes, 15°C) prior to use and resuspended in the appropriated solvent according to use.

Fluorescein (Sigma-Aldrich) or curcumin-loaded NCs were prepared as above. Briefly, 1mg of fluorescein were dissolved in acetone and added to the organic phase containing the polymer. For curcumin loaded NCs, 2 mg of curcumin dissolved in DMSO were mixed with the organic phase. After evaporating the organic phase using a desiccator, the NLR and curcumin loaded NCs were centrifuged and resuspended in ddH_2O. After centrifugation, the NCs were placed in dialysis for 2 days in ddH_2O, using a dialysis membrane (12kDa cutoff, Sigma-Aldrich), to remove dye excess. The NCs were collected, centrifuged and resuspended in 1x PBS. These particles were employed to obtain the confocal images and flow cytometry experiments.

4.2.2 Cell lines culture

Invasive breast ductal carcinoma (MCF-7, from Bank Cell Rio de Janeiro - BCRJ), adenocarcinomic human alveolar basal epithelial (A549, BCRJ) and human dermal fibroblasts, neonatal (HDFn, BCRJ) cells were culture in Dulbecco's Modified Eagle Medium (DMEM, Vitrocell or Gibco) with 10 % (v/v) FBS. Healthy breast cells (MCF-10A, BCRJ), were cultivated in Mammary Epithelial Cell Growth Basal Medium (MEBM, Lonza) supplemented with 100 ng mL^{-1} cholera toxin (Sigma-Aldrich) and Mammary Epithelial Cell Growth Medium SingleQuotsTM Kit (MEGM, Lonza) at 37 °C in a humidified atmosphere with 5% CO_2. For confocal samples MCF-10A cells were cultivated in DMEM/F12 (Thermo Fisher) supplemented with 5 % (v/v) horse serum (HS, Thermo Fisher), 20 ng mL^{-1} epidermal growth factor (EGF, Peprotech), 0.5 mg mL^{-1} hydrocortisone (Sigma-Aldrich), 100 ng mL^{-1} cholera toxin (Sigma-Aldrich), 10 µg mL^{-1} insulin (Sigma-Aldrich) and 1 % (v/v) penicillin/ streptomycin.

4.2.3 Cell membrane extraction

MCF-7 cells in 90% confluence (175 cm^2 flasks), were detached by trypsinization and centrifuged at 800 g for 5 minutes at room temperature. The pellet was washed twice with 1X PBS. The washed pellet was resuspended in 5 mL hypotonic buffer (10 mM Trisbase, 1.5 mM $MgCl_2$, 10 mM NaCl, pH 6.8, all Sigma Aldrich). After 5 minutes, centrifugation was performed at 800 g, for 5 minutes, at 4 ºC. The pellet was resuspended in 5 mL of lysis buffer (0.25 M sucrose, 10 mM HEPES, 100 mM succinic acid, 1 mM EDTA, 2 mM $CaCl_2$, 2 mM $MgCl_2$, pH 7.4, all Sigma Aldrich), and homogenized 70 times (1400 rev min^{-1}) in a VIRTUS PII glass homogenizer. To remove cell debris, the solution was centrifuged at 10,000 g, for 20 minutes, at 4 ºC. The supernatant, containing the cell membrane vesicles, was ultracentrifuged at 100,000 g, for 2 hours, at 4ºC, using an Optima MAX-XP ultracentrifuge (Beckman Coulter, USA). The pellet was resuspended in 100 µL in 1x PBS with protease inhibitor cocktail (SIGMAFAST™) and stored at -80 °C.

4.2.4 Functionalization of nanoparticles with cell membrane

PLGA-PTX NCs were centrifuged and resuspended in 1X PBS followed by 15 minutes sonication. Cell membrane vesicles were also sonicated for 15 minutes. After, cell membranes and PLGA-PTX NCs were mixed (100 µL membrane:100 µL NCs) completing with 800 µL of 1X PBS and sonicated for more 15 minutes (80% of power, 37 Hz). Size, distribution and zeta potential of all nanocarriers and membrane extract were analyzed using Zetasizer Nano ZS, Malvern. The number of particles per mL as well as particle size distribution was estimated by Nanoparticle Tracking Analysis (NTA) using a Nanosight NS300, Malvern.

4.2.5 Transmission electron microscopy (TEM) and Scanning electron microscopy (SEM)

For TEM, 3 µL of PLGA-PTX, mPLGA-PTX NCs and MCF-7 vesicles were drop-casted on copper grids for 60 seconds and dried with filter paper. Following, samples were stained with 3 µL of 2% uranyl acetate for 30 seconds and again dried with filter paper. The staining was done twice. Cryogenic transmission electron microscopy samples were prepared by depositing 3 µL of the dispersions on a copper grid, the excess was dried for 3 seconds with filter paper and the grid was dipped in liquid ethane. The procedure was performed by Vitrobot Mark, Thermo Fisher. The microscopies used were JEOL 1400 and JEM-2100 TEM. The mean size of cryo-TEM images was evaluated analyzing 100 and 93 particles using Image J for PLGA-PTX and mPLGA-PTX NCs, respectively. For negative staining TEM the mean size was evaluated using 100 particles for mPLGA-PTX NCs and 66 particles for PLGA-PTX NCs.

Field-emission Scanning Electron Microscopy (FE-SEM) was also employed to observe PLGA-PTX NCs size distribution and morphology. Samples were prepared by drop-casting 10µL of the sample diluted in deionized H_2O onto clean silicon substrates and dried in a desiccator. Prior to the analysis, the samples were coated to conduct by platinum plasma spraying. Images were collected using a ZEISS SIGMA VP FE-SEM.

4.2.6 Fourier-transform infrared spectroscopy (FTIR)

FTIR was used to analyze the differences between NCs. 10 µL of the samples diluted in PBS 1x were deposited onto clean silicon substrates and dried under reduced atmosphere. The spectra were collected with 128 scans per sample with 4 cm^{-1} resolution from 4000 to 400 cm^{-1} using an Infrared spectrometer Nicolet 6700/GRAMS Suite.

4.2.7 Cellular uptake studies

4.2.7.1 Flow cytometry

In 24-well plates, $2x10^5$ cells per well were seeded and grown for 24 hours. Medium was removed, followed by the incubation of $5x10^{10}$ particles mL^{-1} of non-coated PLGA NCs and MCF-7 cell membrane-coated PLGA NCs, containing curcumin as the fluorescent probe. After 4 hours of incubation, cells were washed twice with 1X PBS and detached by trypsinization. Finally, the samples were centrifuged (500 g, 5 minutes) and resuspended in Sheath Fluid (BD Bioscience) supplemented with 0.5% (w/v) bovine serum albumin (BSA) and kept on ice prior flow cytometry measurements. All measurements were done using BD FACSCalibur™ measuring the fluorescence of using channel FL1 (530/30). Data analysis was performed using FlowJo V10 software and Prism.

4.2.7.2 Confocal laser scanning microscopy (CLSM)

MCF-7 and MCF-10A internalization with coated and non-coated NCs was observed using Leica TSC SP2 confocal microscope using a 63x/1.32 immersion oil objective. $1x10^4$ cells per chamber were incubated in eight-well LabTek® chamber slide grown for 20 h at 37 °C, 5% CO_2. Prior to incubation, cells were washed once with 1X PBS and $5x10^{10}$ NCs-NLR were incubated per well for 4 hours. LysoTracker™ Red DND-99 (Thermo Fisher #L7528) was incubated at 75 nmol L^{-1} for one hour with the NCs as well as Hoechst for 30 minutes at 1 µg mL^{-1}. After, cells were washed twice with 1X PBS, fixed with 3.7% paraformaldehyde (PFA) for 10

minutes and washed again with 1X PBS. Slides were mounted with PBS:glycerol (50:50) and a cover slip was carefully placed over the samples.

4.2.8 Cell viability

Cell viability was analyzed by MTT assay after 48 hours of incubation with the samples. In 96, wells plate, cells were seeded at a density of $2x10^3$ cells per well grown for 24 hours. In sequence, media was removed and 200 µL of the nanoparticles or free drug in different concentrations (0.15, 0.75, 1.5, 7.5 ng mL^{-1} of PTX) were incubated for 48 hours. After this, the nanoparticles were removed, washed 1X PBS and 3-(4,5-dimethylthiazol-2-yl)-2,5-diphenyltetrazolium bromide (MTT, Sigma Aldrich) was incubated 100 µL at 0.5 mg mL^{-1} for 3 hours. Formazan crystals were dissolved in 100 µL of dimethyl sulfoxide (DMSO, Synth) per well and left under orbital agitation for 5 minutes. Measurements were performed at 570 and 630 nm using a microplate reader SpectraMax M3 (Molecular Devices). Cell viability was calculated compared to controls without treatment as described in Equation 3.1. Data analysis was performed using Origin 2020 and Prism. PTX concentration in NCs was estimated using NTA and concentrations from $1x10^8$ to $1x10^{10}$ NCs per mL and using the encapsulation efficiency.

4.3 RESULTS AND DISCUSSION

First noticed in 2011,[20] cell membrane-based nanoparticles have used different core platforms from polymeric to plasmonic nanoparticles, adding photothermal to chemotherapy agents.[153] This chapter is aimed at the developing cancer cell membrane-coated PLGA NCs containing paclitaxel to improve treatment effectiveness and reduce drug resistant by homotypic adhesion. The interaction of the NCs with cells lines from tumor microenvironment is also evaluated.

4.3.1. PLGA-PTX NCS and mPLGA-PTX NCs characterization

Polymeric nanoparticles have been used to release drugs in a controlled manner, improving stability of the actives and increase the cellular uptake.[154] These characteristics are directly related to the synthesis methodology, type of polymer and

the drugs of interest to be encapsulated. PLGA has been widely used for NCs formation due to its biodegradability, low toxicity and for being approved by FDA.[145] As PTX is a hydrophobic compound, there are two common approaches to encapsulate it: the emulsification solvent evaporation and the nanoprecipitation techniques.[145,154] The emulsification route is based on the mixture of a non-miscible solvent in an aqueous phase by using a high shear force. The main disadvantage of this method is the use of high shear force could affect the stability, making it difficult the standardization.[155] Thus, nanoprecipitation was used to synthesize Paclitaxel-containing PLGA NCs. The latter technique generates nanoparticles by one step , using a miscible organic phase.[152] The encapsulation efficiency of PTX by nanoprecipitation was high, with a value of 98 ± 1%, as analyzed by High-performance liquid chromatography (HPLC), using three different batches (as seen in Figure S4.1, Appendix B). Dynamic light scattering measurements showed a Z-average of 195 nm and a polydispersity index (PdI) of 0.125, in accordance with the narrow population with a center in 200 nm, shown in Figure 4.2A. Nanosight analysis revealed that the synthesis yields a high mean concentration of $8.3x10^{12}$ particles mL^{-1} and confirmed the size distribution around 200 nm (Figure 4.2B). Pure MCF-7 vesicles, extracted by hypotonic lysis, showed a broader size population of 200 nm (Z-average of 181 nm) when compared to PLGA-PTX NCs (Figure 4.2C) with a PdI of 0.228 and a concentration of $1.5x10^{11}$ particles mL^{-1} with similar size distribution in NTA (Figure 4.2D) and DLS.

There are two main approaches to functionalize the PLGA nanoparticles with cell membrane vesicles, by extrusion or by sonication.[153] The first studies on membrane coatings used physical co-extrusion through polycarbonates membranes.[20,156] Despite the success in the coating, this method resulted in material loss.[53] Sonication has been recently used to overcome this problem.[157] PLGA-PTX NCs were coated by sonication, once it coats nanoparticles as extrusion without wasting too much material.[153,157] The fusion process of the MCF-7 membrane vesicles and the PLGA nanoparticles were performed in a 1:1 v/v proportion. It was observed an increase in size and surface charge which indicates NCs functionalization with membrane extract (Figure 4.2).[133] The MCF-7 cell membrane-coated PLGA-PTX NCs (mPLGA-PTX NCs) exhibited an increase in the hydrodynamic diameter with an average size of 293 nm with PdI of 0.235 (Figure 4.2E). Size distribution observed by NTA showed the main population close to 150

nm with a significantly asymmetric peak towards bigger sizes and a concentration of $8.1x10^{11}$ particles mL^{-1} (Figure 4.2F).

Zeta-potential analysis showed an increase in the surface charge when PLGA-PTX NCs are combined with MCF-7 membrane by sonication from -5 to -24 mV (Figure 4.2G), also indicating the functionalization of the NCs with MCF-7 membranes vesicles. Although the surface charge is not similar to the pure vesicles (with a charge value of -15 mV), the ad of the membrane is mainly governed by electrostatic repulsion of the surface of the membrane and the particles size. This repulsion favors the attraction of the negative surface of the NCs with the less negative intracellular side of the membranes.[108] This is only possible due to the asymmetric distribution of proteins and lipids on a cell membrane.[118]

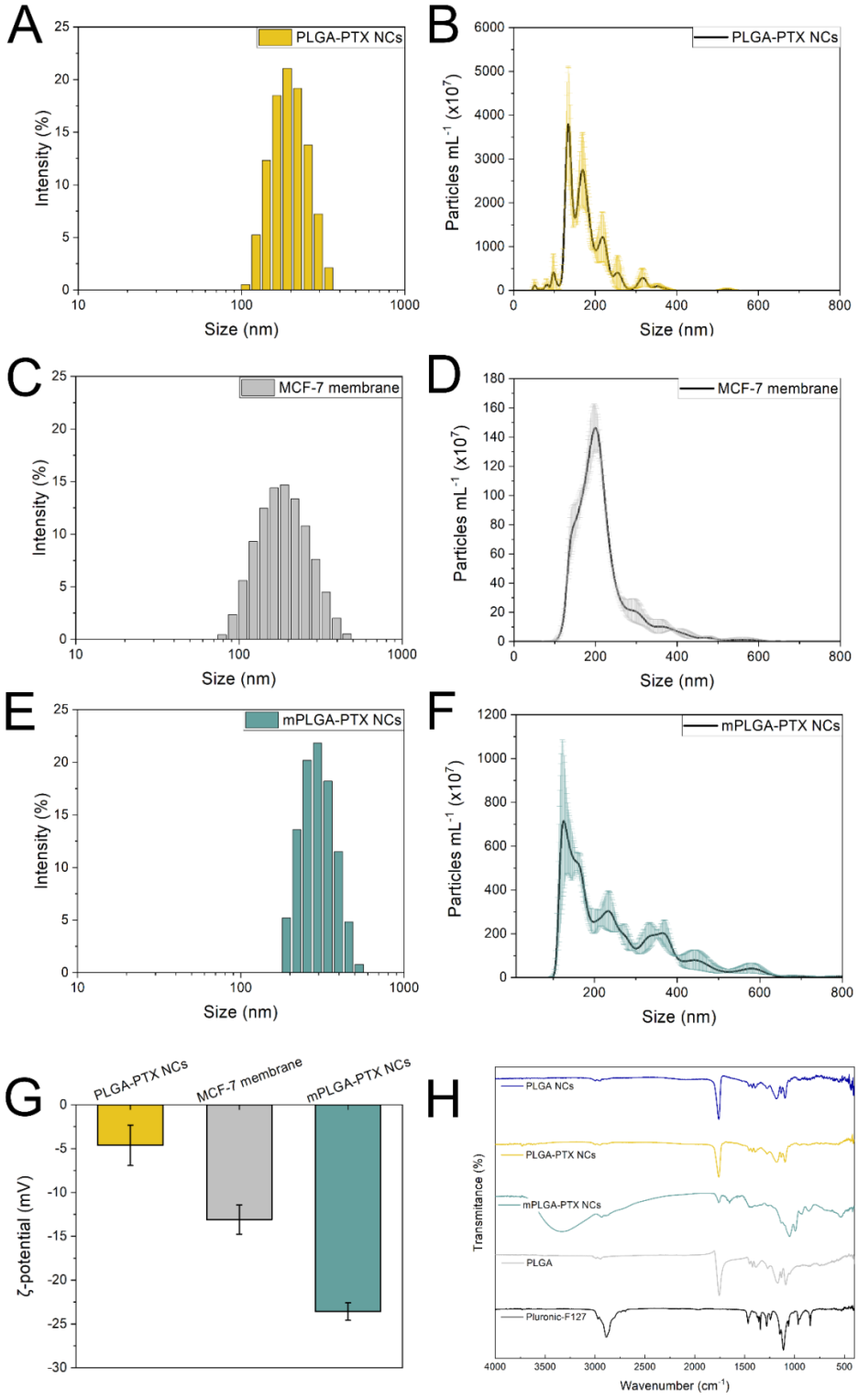

Figure 4.2 - Size distribution, zeta potential and FTIR characterization of PLGA-PTX NCs, MCF-7 vesicles and mPLGA-PTX NCs. PLGA-PTX NCs characterization by A) dynamic light scattering (DLS) and B) Nano tracking analysis (NTA). MCF-7 vesicles size distribution by C) DLS and D) NTA. Finally, mPLGA-PTX NCs analysis by E) DLS and F) NTA. G) Zeta Potential of the nanocarriers of mean and standard deviation of three independent synthesis, MCF-7 vesicles are representative of one batch. E) FITR analysis of the NCs (Measurements are represented by average and error bars by standard error)

Source: By the author.

FTIR analyses of PLGA-PTX NCs, their components and mPLGA-PTX NCs was performed as shown in Figure 4.2.H. PLGA NCs, PLGA-PTX NCs, Pluronic F 127 and PLGA polymer presented the symmetrical and asymmetrical stretching bands of CH_2 and CH_3 groups between 2980 and 2850 cm^{-1}. The asymmetrical deformation of CH_2 and CH_3 between 1450 and 1375 cm^{-1} also appeared in all the sample's spectra. Additionally, it was observed a well-defined band at 1760 cm^{-1} from C=O stretching, in PLGA containing samples, due to glycolic and lactic acid. The main difference in mPLGA-PTX and PLGA-PTX NCs is the presence of amide I band in 1650 cm^{-1} related stretching of peptide bonds, indicative for proteins. A broad peak at 3400 cm^{-1} of -OH stretching, might be related to the hydration level that plasma membrane carries, being difficult to eliminate using the same setup, as nanoparticles without biological content. [122] The spectral range from 1250 to 1000 cm^{-1} are related to the presence of carbohydrates and phosphate, due to the presence of PBS, it is not discussed here.

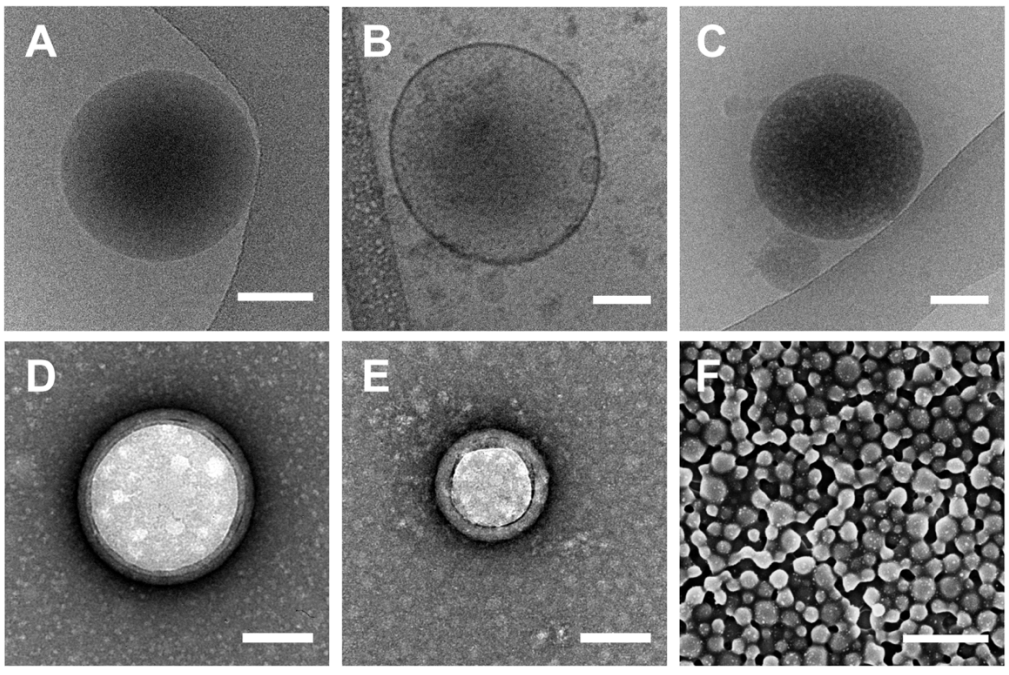

Figure 4.3 - Microscopic characterization of the NCs. CryoTEM images of A) PLGA-PTX, B) MCF-7 extracted membranes and C) (MCF-7)-membrane-coated PLGA-PTX measured in 0.1 x PBS (pH 7.4). Scale bars represent 100 nm. Negative staining transmission electron microscopy (TEM) of D) PLGA-PTX NCs and E) mPLGA-PTX NCs where scale bars represent 100 nm. F) Scanning electron microscopy (SEM) image of PLGA-PTX NCs where scale bar represents 500 nm.

Source: By the author.

Cryogenic transmission electron microscopy images were obtained to evaluate the vesicular properties of the cell membrane extract and differences in morphology of PLGA-PTX NCs and mPLGA-PTX NCs. Figures 4.3A shows the spherical geometry of PLGA-PTX NCs in with an average size of 168.6 nm, corresponding to the DLS and NTA measurements. The isolation of the MCF-7 cell membrane maintained their vesicular shape, as shown in Figure 4.3B. Cell membrane-coated nanoparticles mPLGA-PTX NCs (Figures 4.3C) images showed a mean size of 177 nm, but it did not enable a clear membrane visualization in the surface of PLGA NCs, probably due to the thick ice formation in the images as shown in Figure S4.2. An irregular layer in the surface of the polymeric nanoparticles was observed (Figure S4.2, Appendix B), indicating that the coating was not uniform forall particles.[158] It is important to note is that no lack of spare membrane vesicles was seen in all data acquisition, evidencing the interaction and colocalization of the membrane on PLGA surface.[108,158-159] Cryo-TEM images showed similar sizes as DLS and NTA, as expected, once this technique allows the analysis in liquid.[160] Negative staining TEM showed means sizes of 188 and 221 nm for PLGA-PTX and mPLGA-PTX NCs, respectively. The negative staining shows a higher particle size than Cryo-TEM, due to flattening caused by the drying process.[161] SEM imagens show the monodisperse characteristic of PLGA-PTX NCs sample as shown in Figure 4.3.F, in accordance with it had been seen in a broad area shown in Cryo-TEM (Figure S4.3, Appendix B). Additionally, in a larger scale, we observed the deformation of some PLGA-PTX.

4.3.2. (MCF-7)-membrane-coated PLGA NCs preferential cellular uptake

Cell membrane coating enables the active targeting of the nanoparticles and their interaction with cells is dependent of heterotypic and homotypic bindings between cancer cell membranes.[151] Flow cytometry assays were performed to evaluate the cellular uptake of theNCs (Figure 4.4). The results demonstrated that mPLGA-PTX NCs have an increased interaction with all cells, which indicates the occurrence of homotypic and heterotypic interactions (Figures 4.4), with stronger interaction for the source cell. This is due to the same composition of the nanoparticle with the source cell line. Fang and colleagues also observed the increased interaction of the cancer cell membrane NCs with the source cell by

homotypic binding.[151] The second strongest interaction of the mPLGA-PTX NCs was with the fibroblasts (HDFn). These results suggest the presence of common membrane antigens, e.g. EpCAM, expressed in normal epithelia and dermal fibroblasts.[162] NCs interacted less with lung cancer cell line (A549). Additionally, A549 and MCF10a cells showed a similar uptake rate of PLGA-PTX NCs

It is known that tumor cells crosstalk with fibroblasts and generates a cancer associated fibroblast (CAF) cascade to develop the best stroma scenario for tumor development. Nevertheless, this activation cascade was shown to be related with E-Cadherin and Ep-CAM adhesion molecules.[163] MCF-7 vesicles endows these molecules that increase the interaction with the primary fibroblast due to the crosstalk in tumor growth, to increase the expression of myofibroblastic markers.[22,163-164]

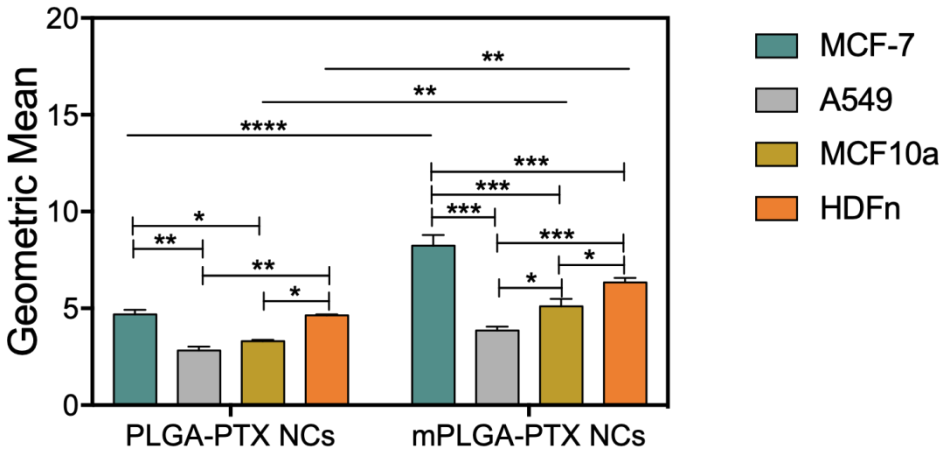

Figure 4.4 - Cellular uptake comparison between PLGA-Curcumin NCs and mPLGA-Curcumin NCs incubated for 4 hours in by MCF-7, A549 lung, MCF10a and HDFn. Measurements are average ± standard error of three independent experiments. Data was analyzed by analysis of variance (ANOVA) and Tukey's test (Measurements and error bars are represented by average and standard error. Significances are indicated with * p-value < 0.05, ** p-value < 0.01, *** p-value < 0.001 and **** p-value<0.0001)
Source: By the author.

Flow cytometry is an important tool to evaluate the cellular uptak of the NCs. However, this technique does not differentiate cellular uptake from nanoparticles in the surface of the cells.[165, 166] Thus, confocal microscopy analysis was performed to evaluate cellular uptake, due to the confocal capacity to produce optical sections capable of differentiate the uptake and surface interaction.[167] Thus, the PLGA-fluorescein and mPLGA-fluorescein NCs were incubated for 4 hours in MCF-7 and MCF-10A cells, and the images displayed here are a section in the middle of the cells (Figure 4.5). Results showed that the

presence of the membrane coating affects the internalization of PLGA NCs in both cancerous and non-cancerous cell types, being slightly more pronounced in MCF-7 cells, in accordance with flow cytometry results.

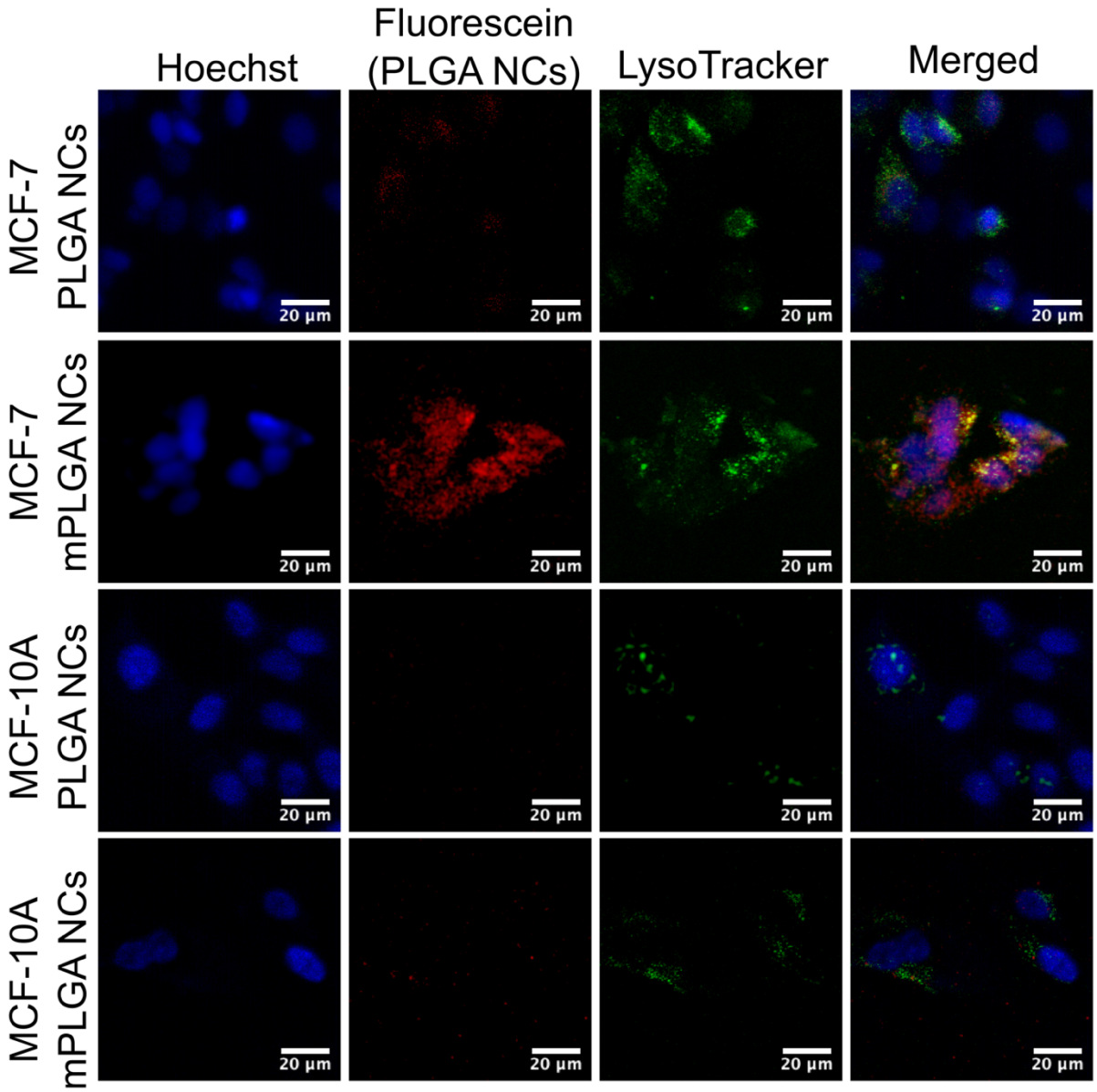

Figure 4.5 - Cellular uptake comparison between PLGA-fluorescein NCs and mPLGA-fluorescein NCs incubated for 4 hours in MCF-7 and MCF10a by confocal analysis.
Source: By the author.

4.3.3 In vitro evaluation of MCF-7 membrane-coated PLGA-PTX NCs

Proving the mPLGA-PTX NCs preferential uptake with breast cancer. The therapeutic efficiency of PTX in PLGA-PTX NCs and mPLGA-PTX NCs was

compared with the free drug by performing viability tests in health and cancer cells, shown in Figure 4.6.

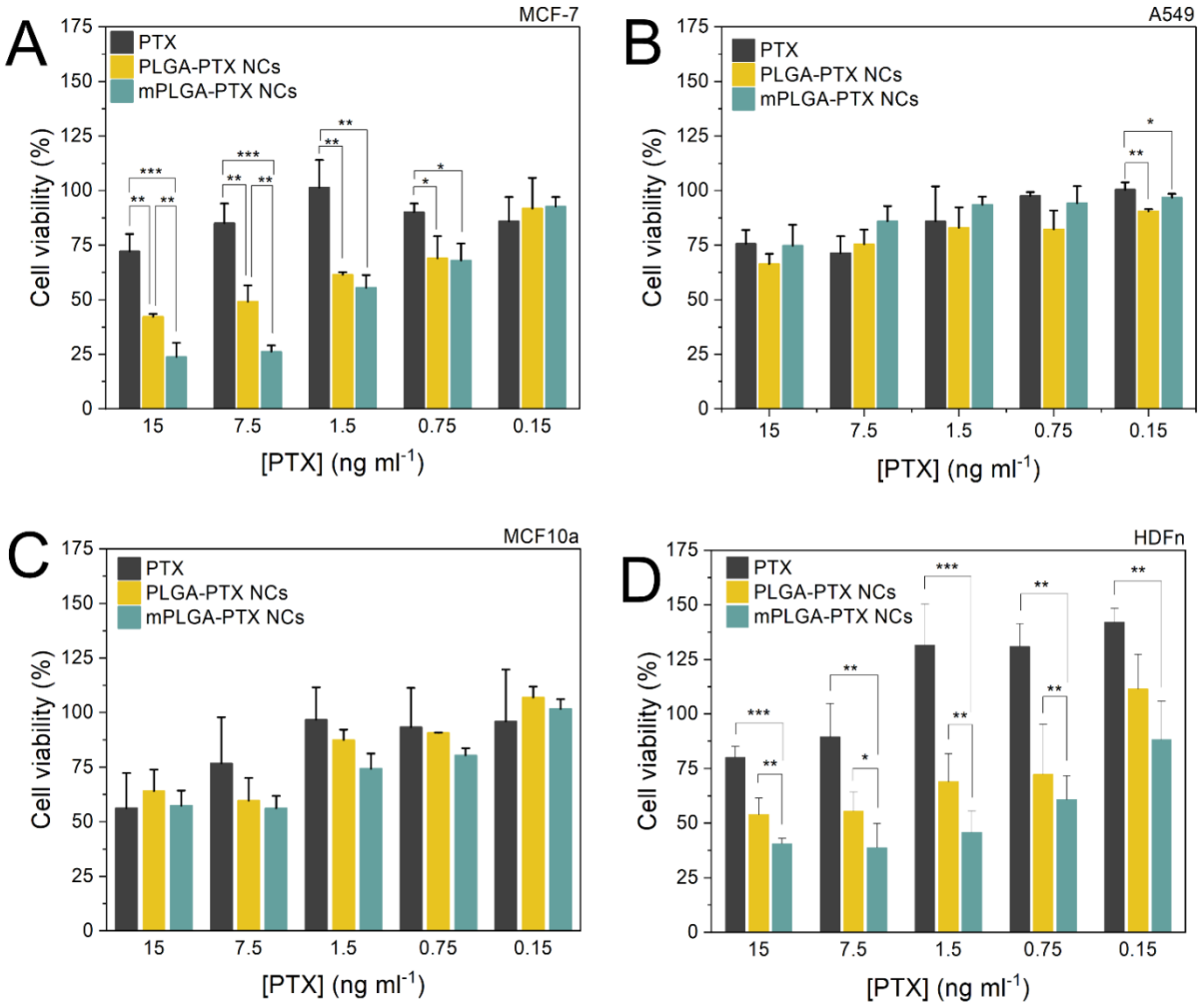

Figure 4.6 - Cellular viability of A) MCF-7, B) A549, C) MCF10A and D) HDFn after 48 hours using different concentration of PTX as free drug, PLGA-PTX, mPLGA-PTX by MTT assay. Statistical analysis using two-way ANOVA (* p-value < 0.05, ** p-value < 0.01, *** p-value < 0.001).
Source: By the author.

After 48 hours of incubation, mPLGA-PTX NCs significantly decreased in the viability of MCF-7 cells (Figure 4.6A) compared to PLGA-PTX NCs and the free drug, especially at higher concentrations (15 ng mL^{-1}) that showed a reduction of 25% in viability when comparing to PLGA-PTX NCs. With the higher levels of cellular uptake as observed in flow cytometry and confocal analyses, more PTX is available intracellularly reflecting in the toxicity. The viability of A549 was also investigated (Figures 4.6B) and no differences were observed between the NCs and free PTX and

only at the lowest concentration the viability showed statistical relevance. It is known that A549 has a multidrug resistant system to survive, and this mechanism prevented the PTX action when released in the cells.[168] Viabilities of MCF10A (Figure 4.6C) exposed to NCs and PTX were not significantly different between the samples in the timeline of the assay. Results of cell viability from HDFn showed that in all concentrations of PLGA-PTX and mPLGA-PTX NCs improved the toxicity of PTX (Figure 4.6D). Fibroblasts viability reduced by at least 50% in the 15, 7.5 and 1.5 ng mL^{-1} of PTX NCs. At these concentrations, mPLGA-PTX NCs showed an enhance in toxicity when compared to non-coated nanocarriers. As a consequence of the cross-talk with tumor cells and fibroblasts, the mPLGA-PTX NCs, significantly interacts with HDFn and improved the delivery of PTX.[151,163]

4.5 CONCLUSIONS

Here we successfully synthesized breast cancer cells-coated nanocarriers and characterized their morphology, size and charge. The presence of the membrane coating of MCF-7 increased the interaction with the source cell because of the homotypic binding between cancer cells, reflecting as a better targetability and improving the treatment. Adhesion seems to also play a role in the interaction between A549, MCF-10A and HDFn cell lines, once the interaction levels of membrane-coated NCs are superior to the ones observed for non-coated NCs. However, this interaction does not provide a toxicity neither for lung cancer nor for non-tumorigenic epithelial cell line. Our results provide a better understanding on the role of cancer cell membrane-coated NCs to improve the effectiveness of free drugs and to interfere with cancer cell-stromal cells for tumor regression.

5 COMPARING EXTRACELLULAR VESICLES ISOLATION BY CULTURE PARAMETERS AND ISOLATION METHODS

5.1 INTRODUCTION

Extracellular vesicles (EVs) are membrane-bound vesicles naturally released by various cells, ranging from 50-10,000 nm.[33] EVs have been recognized by their role in cellular communication mediating several physiological[117] and pathological[30, 169] processes. EVs are classified by size as small (50-200 nm), medium (200-1000 nm), and large extracellular vesicles (1-10 μm).[33] The small subset is the most involved EVs in communication between cells. Their size and role in communication are related to their biogenesis. Most of the small EVs (sEVs) are generated with the membrane folding inward creating intraluminal vesicles that mature into multivesicular bodies, which are released by the cells by fusion with the plasma membrane (Figure 5.1).[170] Due to the biogenesis, sEVs are known by the expression of proteins from multivesicular bodies as CD9, CD63, ALIX[33] and, also carry proteins and nucleic acids related to the donor cell.[171] Since the cargo and protein expression are donor-dependent, EVs from different origins endows different functions.[172]

Tumor cell-derived EVs are related to angiogenesis maintenance,[173] tumor progression,[174] immune scape[175] and chemotherapy resistance.[176] For example, EVs from multidrug-resistant cells showed to transfer the P-glycoprotein into drug-sensitive cells.[176] Immune cell-derived EVs are also known to communicate and slow down cancer progression. Dendritic cell-derived EVs have been shown to increase the proliferation of natural killer cells reducing lung metastases *in vivo*.[177] Also, tumor-associated macrophages cell-derived EVs facilitate an immune-suppressive tumor microenvironment for tumor progression.[178] The capability of EVs to interact with recipient cells by endocytosis and release their cargo, shows that EVs are a promising tool for the delivery of agents in cancer therapy.[28,101,179-180]

Despite several advances reported in the literature using EVs as carriers, no consensus on which method of EVs isolation increases yield and improves sample quality.[181-183] Ultracentrifugation, size exclusion chromatography, polyethylene glycol precipitation and filtration are the most reported methods in the literature.[181] The

ultracentrifugation is considered the standard-gold protocol and the technique more commonly used. Based on serial centrifugation, it begins with a centrifugation step to remove cells alive or dead and cellular debris, followed by two steps of ultracentrifugation, one to isolate the EVs and another for washing. The main limitation of this technique is the small volume that is possible to extract using the ultracentrifuge and not being accessible as point of care.[111,184] Filtration is a technique based on the exclusion by size, using membrane filters with defined sizes to isolate the EVs from the cellular solution. The advantage of filtration is the processing of large volumes, however, due to the high pressure values used in this protocol, deformation of vesicles may occur.[185]

Finally, the precipitation of EVs is an alternative to processes with several steps. It is based on the addition of a polymer, usually polyethylene glycol (PEG), to the medium that contains EVs, altering the solubility and the dispersivity of the medium, and using simple centrifugation one may obtain the EVs. Although the simplicity of the method, the final product is based on a set of EVs with high quantities of contaminants, such as aggregated protein.[185-186]

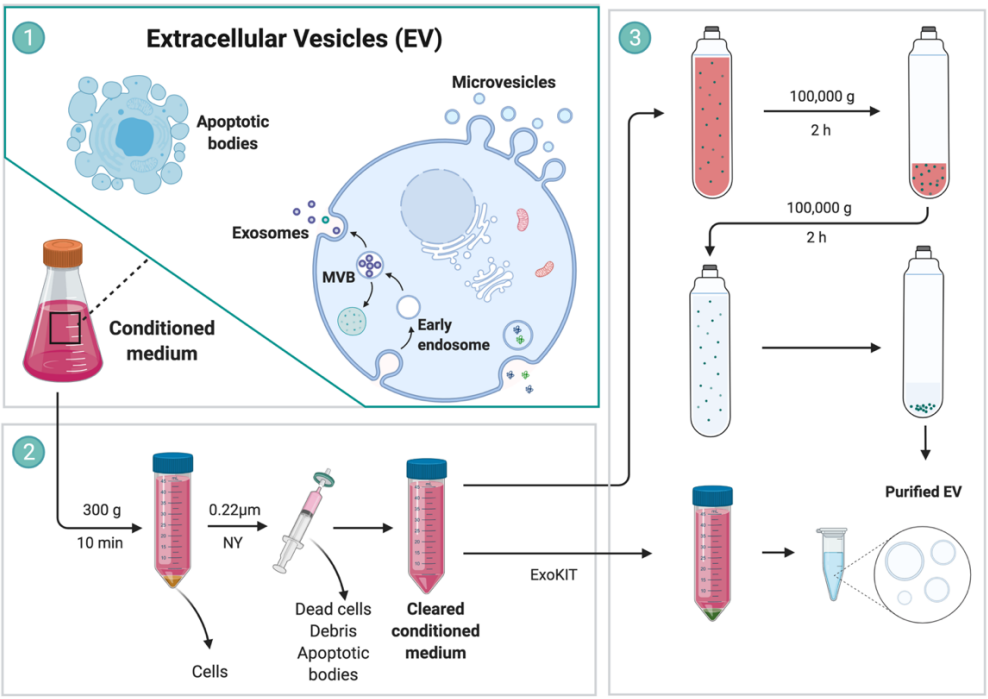

Figure 5.1 - Schematic representation of the isolation methods compared in this thesis. 1) The conditioned medium was prepared when incubating the cells with medium and 10% of FBS EVs-depleted. 2) The conditioned medium was harvest after a period and further centrifugated and filtered to eliminate cells, debris, and apoptotic bodies. 3) EVs were isolated using two approaches PEG precipitation and ultracentrifugation.
Source: By the author created with biorender.com.

In this chapter, we analyzed the parameters to improve the yield of extracellular vesicles isolation using several parameters as volume, time, and source cell. To optimize these parameters we evaluated two methods for isolation: PEG precipitation and ultracentrifugation. Anticipating, we showed that the cell concentration has a nonlinear dependence with EVs production. At lower densities, there is a slight tendency to improve EVs production. Additionally, the precipitation method outperformed the ultracentrifugation in yield in two different cells. However, with the high yield, there was a loss in purity. Finally, by decreasing the volume incubated to 15 mL, no drastic changes were observed in size distribution, and a 10-fold improvement in EVs concentration was achieved.

5.2 METHODOLOGY

5.2.1 Cell lines culture

Rat hepatoma (HTC, Sigma Aldrich) and Macrophage Abelson murine leukemia virus-transformed (RAW264.7, American Type Culture Collection, ATCC) cells were culture in Dulbecco's Modified Eagle Medium (DMEM, Vitrocell or Gibco) with 10 % (v/v) FBS at 37 °C in a humidified atmosphere with 5% CO_2.

5.2.2 Extracellular vesicles isolation by ultracentrifugation

HTC was cultured in 175 cm^2 flasks (Greiner) seeded at $5x10^6$ cells mL^{-1}. After 24 h, culture media was replaced by DMEM supplemented with 10% (v/v) FBS depleted of EVs (Thermo Fisher Scientific). Cell culture medium was collected at different times of 0, 12, 24, 48, and 72 hours and centrifuged at 800 g for 4 minutes at room temperature to remove detached cells. The supernatant was submitted to filtration with a membrane with a pore size of 0.22 µm (Corning, Nylon), to remove cell debris, and large EVs.[111] Cleared conditioned medium was ultracentrifuged (Optima MAX-XP, Beckman Coulter, TLA 110 rotor) at 100,000 g for 2 hours at 4 °C. The pellet was washed with 1X phosphate buffered saline (PBS) followed by a second ultracentrifugation step at 100,000 g for 2 hours at 4 °C. The pellet was collected and resuspended in 1X PBS containing SIGMAFAST™ protease inhibitor

cocktail and promptly analyzed. The cells were counted using a Neubauer chamber and trypan blue stain.

RAW264.7 were also cultured in 175 cm^2 flasks (Greiner) seeded at $1x10^6$ cells mL^{-1}. After 24 hours, culture media was replaced by DMEM supplemented with 10% (v/v) FBS depleted of EVs (Thermo Fisher Scientific). Conditioned culture medium was collected after 24 hours and centrifuged at 800 g for 4 minutes at room temperature to remove detached cells. The following steps were done using the same steps as for HTC cell-derived EVs.

5.2.3 Extracellular vesicles isolation by PEG precipitation

HTC and RAW264.7 were seeded at $5x10^6$ cells mL^{-1} and $1x10^6$ cells mL^{-1}, respectively in 175 cm^2 flasks. The medium was removed and centrifuged (800g, 5 minutes) to remove detached cells. The supernatant was filtered using the same parameters as above. Samples were transferred to a falcon and the reagent, from Total Exosome Isolation kit for cell culture (Thermo Fisher), added in a 1:3 ratio, agitating vigorously until a homogeneous solution was formed and incubated overnight in the refrigerator. After, the final media was centrifuged 10,000g for 1 hour at 4°C. The pellet was resuspended in a 1X PBS containing SIGMAFAST™. The isolated EVs were characterized immediately.

5.2.4 Characterization of the extracellular vesicles

Nano sight Analysis (NTA). The concentration and size distribution of EVs was measured using a dilution of 1:100 or 1:1000 in 1X PBS (the dilution was decided to measure from 50 to 100 particles per frame) using two independent samples. Three cycles were performed capturing 60 frames in 3 different regions. The equipment used was Nanosight NS300, Malvern.

Transmission Electron Microscopy (TEM). The images were obtained in JEOL - 2100 TEM. Samples were prepared drop-casting 3µL on copper grids for 60 seconds and dried with filter paper. To fix the sample 3 µL of uranyl acetate 2% for 30

seconds was used, followed by drying. TEM images were obtained by JEOL 2100 and Talos Artica.

5.3 RESULTS AND DISCUSSION

5.3.1 EVs production depends on cell's concentration

EVs are potential carriers for biomedical applications.[28] However, differences in protocols isolation delays their use in the clinics.[184] Therefore, basic culture parameters were evaluated. Figure 5.2 shows the results for the HTC cell-derived EVs yields related to the incubation time with EV-depleted medium.

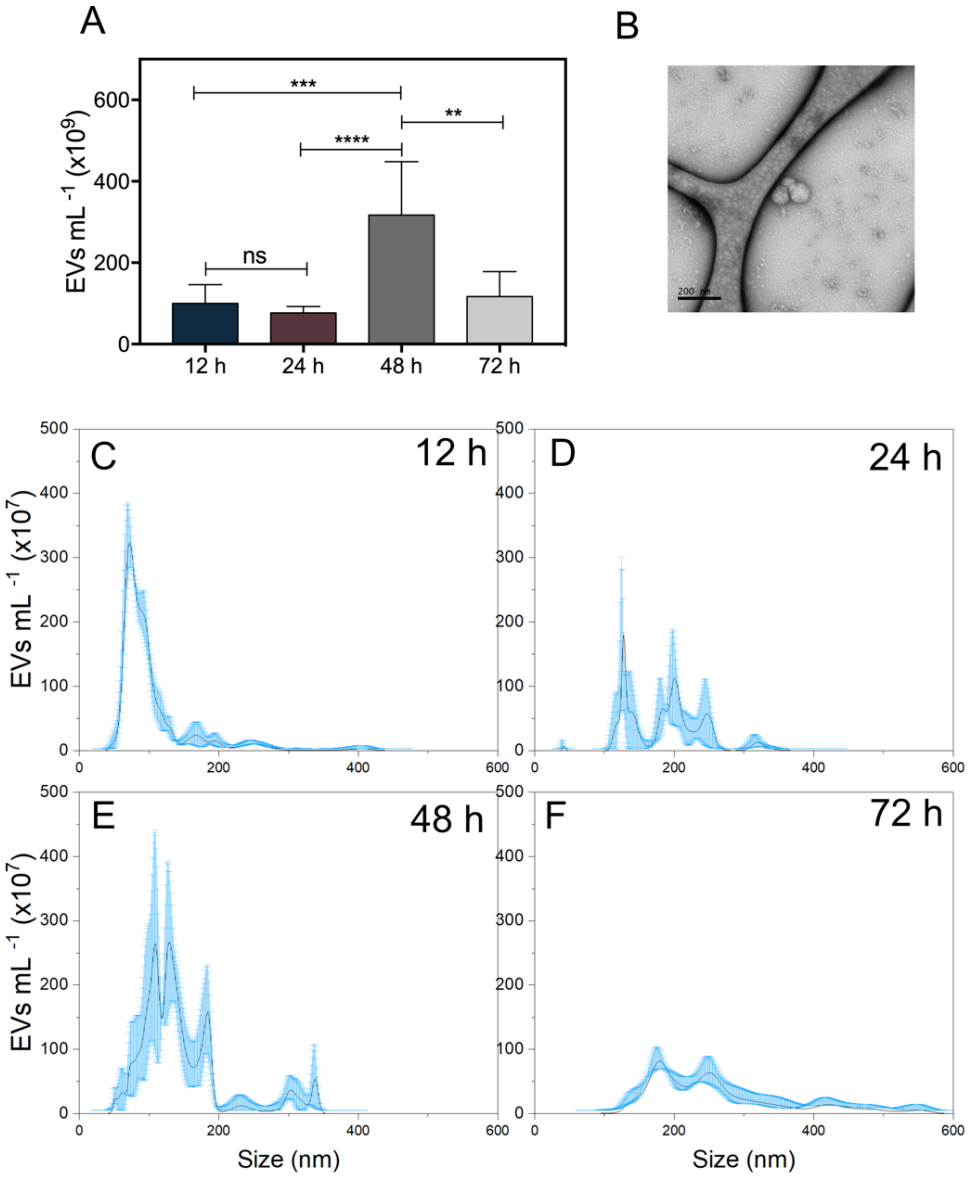

Figure 5.2 - EVs yield of HTC cells at different time points by ultracentrifugation. A) Total Concentration in EVs per mL of HTC derived EVs varying the time of isolation from 12 to 72 hours. The results are represented by average ± standard error. B) Negative staining image of EVs isolated in 24 hours showing their vesicular property. Size distribution of the EVs at different times C) 12 hours D) 24 hours E) 48 hours F) 72 hours. Black line is the average of three measurements and blue errors are represented by standard deviation. Data was analyzed by analysis of variance (ANOVA) and Tukey's test (Significances are indicated with ns, non-significant, * p-value < 0.05, ** p-value < 0.01, *** p-value < 0.001 and **** p-value<0.0001).

Source: By the author.

Upon increasing the incubation time of the media with EVs-depleted FBS, a significant increase in the concentration occured only for 48 hours. Between 12 and 24 hours, no relevant differences were observed (Figure 5.2A). After 72 hours, there

is a decrease in EVs production. These results are related to the cell's concentration as shown in Table 5.1. For 48 hours, the highest cells concentration is observed, thus, a higher EVs production. Adding more 24 hours to the process, we observed the death of cells and decrease in EVs isolation. Cells in processes to die usually release large vesicles as apoptotic bodies, in which our protocol does not apply.[187] For 12 hours, it might be noticed a slight tendency to increase the EVs concentration when compared to 24 hours, indicating that lower densities might lead to higher levels of EVs. The reduced cell-cell interaction may play a key role in EVs production, once it overregulates the EV generation for intercellular communications.[188] The incubation time revealed that cell's concentration is an important parameter to improve EVs production. Figure 5.2B shows the membrane-bound property of the EVs, and that the ultracentrifugation method did not deform the vesicular shape.

The size distribution of the isolation protocols used is shown in Figures 5.2C-F. For 12 hours, it is observed a narrow distribution with centered at 100 nm. By increasing the incubation time, a broadening of the peak and a translation to the center to 200 nm was observed. The 72 hours experiment produced less EVs, decreasing the intensity of the peak. The heterogeneity of the bands above 24 hours might be attributed to more EVs:EVs interaction leading to aggregation.[189]

Table 5.1 – Cell concentration at each time used for EVs isolation. The cells were counted using a Neubauer chamber with trypan blue stain for dead cells.

.

	12 hours	**24 hours**	**48 hours**	**72 hours**
Cells mL^{-1}	$1x10^7$	$1x10^7$	$1x10^8$	$2x10^7$

Source: By the author

5.3.2 Precipitation method yields more EVs than ultracentrifugation

Research on extracellular vesicles suffer from the lack of consensus in data acquisition, isolation methodologies and nomenclature. For example, NTA, as a single particle analyzers started to be recommended only in 2018.[33] Every method of isolation has pros and cons, depending on the final goal as purity or concentration.

Here we compared two different methods: the precipitation using Total Exosome Isolation kit, and ultracentrifugation. Results of isolations from HTC cells are displayed in Figure 5.3.

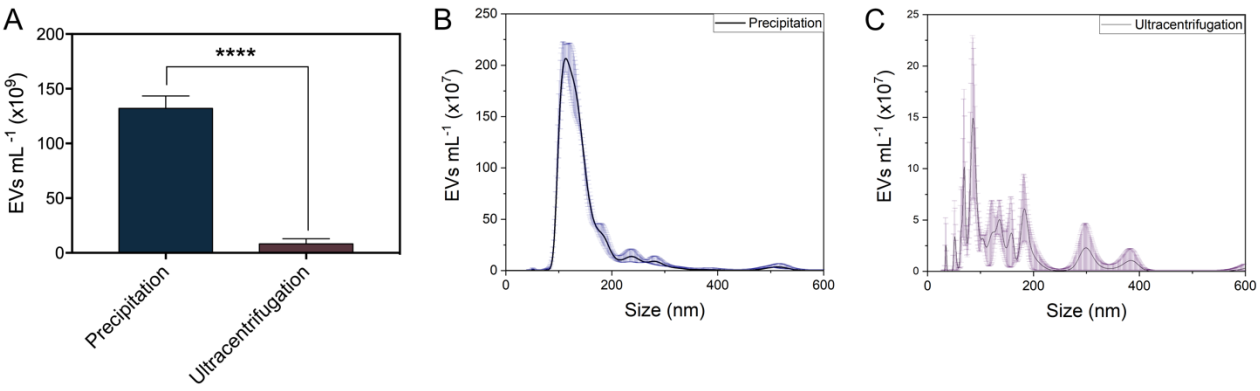

Figure 5.3 - Comparison of the isolation methodology using HTC-derived EVs yield. A) Total Concentration in EVs per mL of HTC-derived EVs using precipitation and ultracentrifugation after 24 hours. The results are represented by average ± standard error from two independent samples. B) Size distribution of the EVs isolated using the precipitation method by Total Exosome Isolation Kit .C) Size distribution of the EVs isolated by ultracentrifugation. Black line is the average of three measurements and navy and purple errors are represented by standard deviation. Data was analyzed by analysis of variance (ANOVA) and Tukey's test (Significances are indicated with * p-value < 0.05, ** p-value < 0.01, *** p-value < 0.001 and **** p-value<0.0001)
Source: By the author.

Figure 5.3A shows that the precipitation method yielded 10x higher than ultracentrifugation. The size distribution of the EVs as seen by precipitation, were more monodispersed with a center close to 150 nm (Figure 5.3B). The ultracentrifugation step provided a more disperse population (Figure 5.3C). Although the isolation kit by precipitation allowed a high EV recovery, the resuspended pellet had a light pink color, from phenol of the medium (data not shown). This implies that there were contaminants that precipitated along with EVs materials. In conclusion this technique improves yield, however, if purity is needed, the combination of methods is recommended.[190-191]

It is known that EVs functional properties and quantity are dependent on the source cells.[117,173] To investigate if the isolation method allowed similar results between two different cells, we evaluated the EVs isolation using a macrophage cell (RAW264.7) as shown in Figure 5.4.

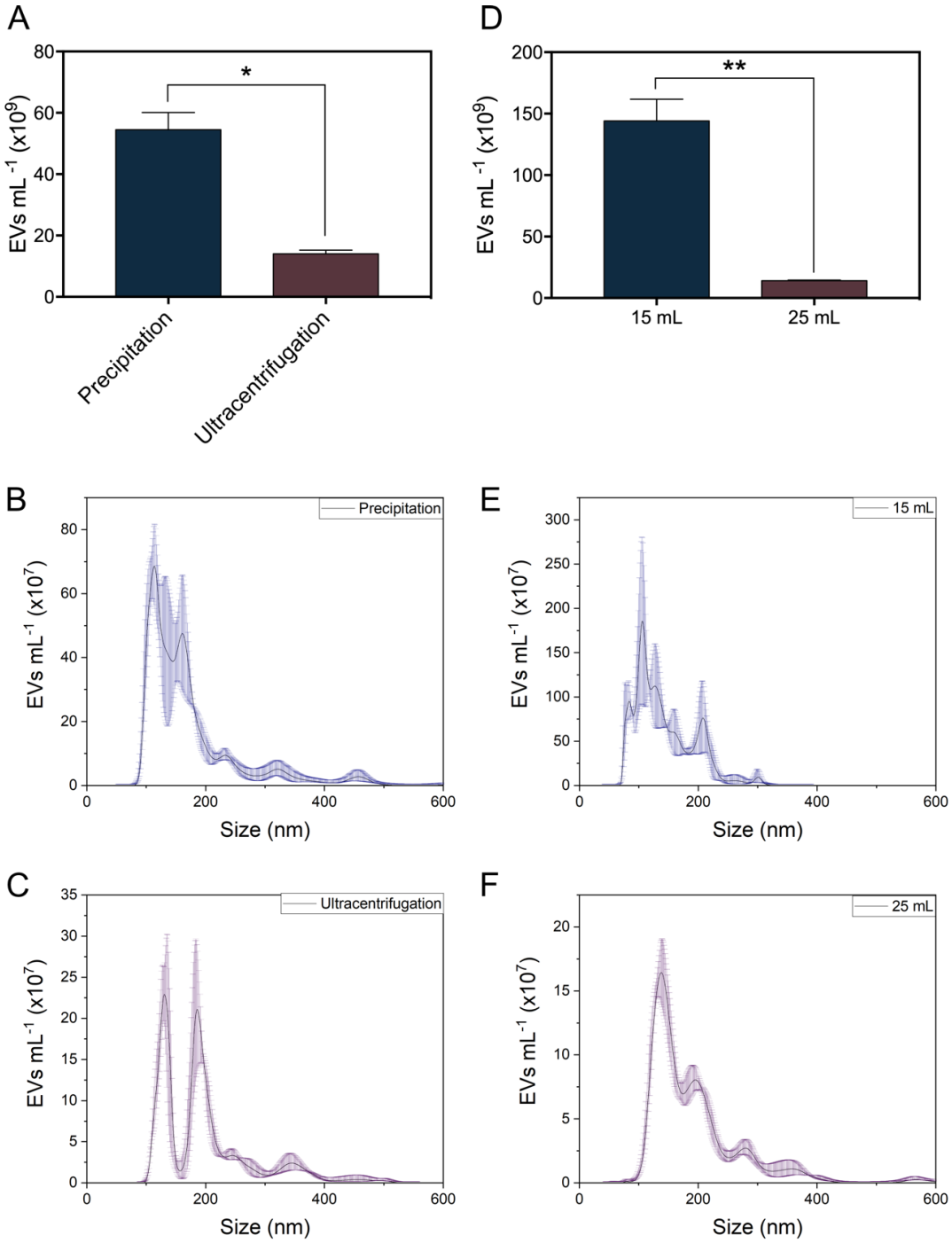

Figure 5.4 - Comparison of isolation RAW264.7-derived EVs yield by methodology and volume used. A) Total Concentration in EVs per mL using precipitation and ultracentrifugation after 24 hours. The results are represented by average ± standard error from two independent samples. B) Size distribution of the EVs isolated using the precipitation method by Total Exosome Isolation Kit. C) Size distribution of the EVs isolated by ultracentrifugation. D) Total Concentration in EVs per mL using ultracentrifugation after 24 hours and varying the volume used (15 and 25 mL). E) Size distribution of the EVs isolated using 15 mL of medium. F) Size distribution of the EVs isolated using 25 mL of medium. Black line is the average of three measurements and navy and purple errors are represented by standard deviation. Data was analyzed by analysis of variance (ANOVA) and Tukey's test (Significances are indicated with * p-value < 0.05, ** p-value < 0.01, *** p-value < 0.001 and **** p-value<0.0001)

Source: By the author.

As it can be seen from Figure 5.4, the precipitation method once more outperformed the ultracentrifugation, increasing the yield by 6x as seen in Figure 5.4A. The size distribution of the precipitation method (Figure 5.4B) showed a center at 100 nm with an asymmetric towards bigger sizes. The bimodal size distribution appeared in the ultracentrifugation method (Figure 5.4C), confirming the aggregation of EVs, similar to HTC-derived EVs.

Two volumes of the added medium were also investigated in this optimization analysis. By decreasing the volume from 25 to 15 mL, EVs concentration increased by 10x. The size distribution did not vary drastically, where samples from 15 mL showed a narrow peak in comparison to 25 mL. Also, EVs derived from macrophages showed their vesicular shape when isolated by precipitation.

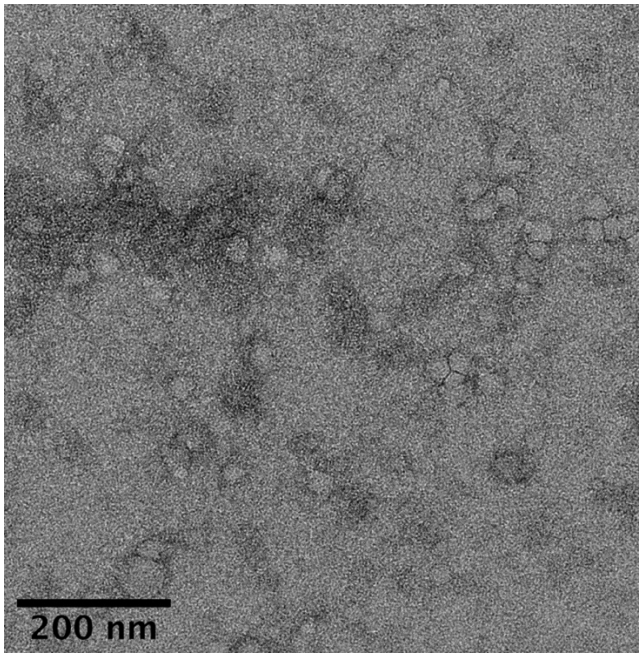

Figure 5.5 - Negative staining image of RAW264.7 EVs isolated by Total Exosomes Isolation kit.
Source: By the author.

4.5 CONCLUSIONS

We investigated the basic culture parameters and isolation methods by EVs concentration and size distribution. Results showed that the cell concentration influences the EVs yield: the higher the amount of cells per mL, the higher the EVs concentration. Additionally, two isolation methods were evaluated. The precipitation method increased at leat 5-fold the yield for both cell types, when compared to the

ultracentrifugation. By decreasing the volume of the medium, we observed a 10-fold increase of EVs concentration. More studies of the EVs functionality *in vitro* are required to check any differences in their applications by means of isolation methods.

6 CONCLUSION

Nanomaterials are shown to be promising platforms for cancer therapy. Nevertheless, it is essential to investigate the cellular response when interacting with these nano-sized materials to properly translate their use to clinical applications. Cell-derived nanomaterials represent a new uprising technology for cancer therapy. However, it has been 10 years since the first report using cell membrane was published, and there are still a lot of studies needed to understand how their structures are related to the cell's response outcomes. In this thesis, we have presented the fabrication of novel biomimetic nanoparticles for cancer therapy.

First, the synthesis of gold nanorods were investigated. Gold nanorods were synthesized by using the seed-mediated method in the presence of CTAB, and with minimum variations in the protocol we were able to synthesize AuNRs with two different aspect ratios. The longitudinal plasmon band shifted towards near infrared when increasing the amount of silver nitrate in the synthesis. Additionally, AuNRs with width above 10 nm increased the aspect ratio upon increasing seeds concentration. AuNRs with width bellow 10 nm showed an increased the aspect ratio, upon decreasing the seeds volume. TEM analysis confirmed the influence synthesis parameters on the AuNRs size and consequentially on the surface plasmon band. These fine tunability of the AuNRs properties resulted in non-linear luminescence for AuNRs with width>10 nm, and an excellent photothermal conversion for mini AuNRs with width<10 nm.

We have successfully biointerfaced the gold nanorods using extracellular vesicles and cell membranes from macrophages. The differences in the coatings were evaluated using cells models for tumor microenvironment. The presence of CD47 in the cell membrane-coated nanorods is crucial for the interaction by homotypic binding with the metastatic cell line. Extracellular vesicles-coated gold nanorods did not expressed CD47 and interacted more with the source cell. Fibroblasts did not interact significantly with the nanomaterials. Finally, toxicity studies showed that the rods were highly toxic for the macrophages, regardless their coating.

We also developed biomimetic polymeric nanoparticles with metastatic cancer cell membrane coatings for the active delivery of paclitaxel. The presence of the cell membrane increased the interaction with all cell lines. The strong interaction of the membrane-coated NCs with the fibroblast resulted in an unwanted toxicity. This result provided evidence that adhesion molecules play a significant role in heterotypic binding. Furthermore, this study revealed the importance of studying the cancer cell membrane-coated nanocarriers interactions with stroma cells.

Finally, we investigated culture parameters and methods of extracellular vesicles isolation. These parameters were evaluated by size distribution and concentration, using Nanotracking analysis. Cells concentration versus EVs yield showed a linear dependency. The precipitation method outperformed the ultracentrifugation method increasing the yield by at least 5x regardless the cell type. Ultracentrifugation yielded extracellular vesicles purer due to the washing step. Basic culture parameters optimization showed that is possible to decrease the volume of the medium without compromising the size quality of the EVs.

REFERENCES

1 ROY, A.; LI, S. D. Modifying the tumor microenvironment using nanoparticle therapeutics. **Wiley Interdisciplinary Reviews**: nanomedicine and nanobiotechnology, v. 8, n. 6, p. 891–908, 2016.

2 SHAH, A. N. *et al*. Hormone receptor–positive/human epidermal growth receptor 2–negative metastatic breast cancer in young women: emerging data in the era of molecularly targeted agents. **Oncologist**, v. 25, n. 6, p. 900–908, 2020.

3 SIEGEL, R. L.; MILLER, K. D.; JEMAL, A. Cancer statistics, 2019. **CA:** a cancer journal for clinicians, v. 69, n. 1, p. 7–34, 2019.

4 QUAIL, D. F.; JOYCE, J. A. Microenvironmental regulation of tumor progression and metastasis. **Nature Medicine**, v. 19, n. 11, p. 1423–1437, 2013.

5 FIDLER, I. J. The pathogenesis of cancer metastasis: the “seed and soil” hypothesis revisited. **Nature Reviews Cancer**, v. 3, n. 6, p. 453–458, 2003.

6 LIU, Q. *et al*. Factors involved in cancer metastasis: a better understanding to “seed and soil” hypothesis. **Molecular Cancer**, v. 16, n. 1, p. 1–19, 2017.

7 COMEN, E.; NORTON, L.; MASSAGUÉ, J. Clinical implications of cancer self-seeding. **Nature Reviews Clinical Oncology**, v. 8, n. 6, p. 369–377, 2011.

8 ZHANG, Z. *et al*. Tumor microenvironment-derived NRG1 promotes antiandrogen resistance in prostate cancer. **Cancer Cell**, v. 38, n. 2, p. 279- 296, 2020.

9 WHITESIDE, T. L. The tumor microenvironment and its role in promoting tumor growth. **Oncogene**, v. 27, n. 45, p. 5904–5912, 2008.

10 CHEN, Q. *et al*. Remodeling the tumor microenvironment with emerging nanotherapeutics. **Trends in Pharmacological Sciences**, v. 39, n. 1, p. 59–74, 2018.

11 PARK, J. Y.; SHIN, M.-S. Inhibitory effects of pectic polysaccharide isolated from diospyros kaki leaves on tumor cell angiogenesis via VEGF and MMP-9 regulation. **Polymers**, v. 13, n. 1, p. 64, 2020.

12 SHI, Y. *et al*. The EPR effect and beyond: strategies to improve tumor targeting and cancer nanomedicine treatment efficacy. **Theranostics**, v. 10, n. 17, p. 7921–7924, 2020.

13 KANG, H. *et al*. Size-dependent EPR effect of polymeric nanoparticles on tumor targeting. **Advanced Healthcare Materials**, v. 9, n. 1, p. 8–15, 2020.

14 DING, Y. *et al*. Investigating the EPR effect of nanomedicines in human renal tumors via ex vivo perfusion strategy. **Nano Today**, v. 35, p. 100970, 2020. DOI:

10.1016/j.nantod.2020.100970.

15 BISSO, S.; LEROUX, J. C. Nanopharmaceuticals: a focus on their clinical translatability. **International Journal of Pharmaceutics**, v. 578, p. 119098, 2020. DOI: 10.1016/j.ijpharm.2020.119098.

16 WILHELM, S. *et al*. Analysis of nanoparticle delivery to tumours**. Nature Reviews Materials**, v. 1, 2016. DOI: 10.1038/natrevmats.2016.14

17 NEL, A. E. *et al*. Understanding biophysicochemical interactions at the nano-bio interface. **Nature Materials**, v. 8, n. 7, p. 543–557, 2009.

18 SALVATI, A. *et al*. Transferrin-functionalized nanoparticles lose their targeting capabilities when a biomolecule corona adsorbs on the surface. **Nature Nanotechnology**, v. 8, n. 2, p. 137–43, 2013.

19 FANG, R. H. *et al*. Cell membrane coating nanotechnology. **Advanced Materials**, v. 30, n. 23, p. 1–34, 2018.

20 HU, C.-M. J. *et al*. Erythrocyte membrane-camouflaged polymeric nanoparticles as a biomimetic delivery platform. **Proceedings of the National Academy of Sciences**, v. 108, n. 27, p. 10980–10985, 2011.

21 ZHANG, Q. *et al.* Cellular nanosponges inhibit SARS-CoV-2 infectivity. **Nano Letters**, v. 20, n. 7, p. 5570–5574, 2020.

22 JIN, J. *et al.* Human cancer cell membrane-coated biomimetic nanoparticles reduce fibroblast-mediated invasion and metastasis and induce T-Cells. **ACS Applied Materials and Interfaces**, v. 11, n.8, p. 7850-7861, 2019.

23 RAO, L. *et al*. Cancer cell membrane-coated nanoparticles for personalized therapy in patient-derived xenograft models. **Advanced Functional Materials**, v. 29, n. 51, p. 1–10, 2019.

24 CHEN, Z. *et al.* Erythrocyte-cancer hybrid membrane-camouflaged melanin nanoparticles for enhancing photothermal therapy efficacy in tumors. **Biomaterials**, v. 192, p. 292–308, 2019. DOI: 10.1016/j.biomaterials.2018.11.021.

25 SUN, H. *et al*. Cancer-cell-biomimetic nanoparticles for targeted therapy of homotypic tumors. **Advanced Materials**, v. 28, n. 43, p. 9581–9588, 2016.

26 TKACH, M.; THÉRY, C. Communication by extracellular vesicles: where we are and where we need to go. **Cell**, v. 164, n. 6, p. 1226–1232, 2016.

27 KANADA, M. *et al.* Differential fates of biomolecules delivered to target cells via extracellular vesicles. **Proceedings of the National Academy of Sciences**, v. 112, n. 12, p. E1433 LP-E1442, 24 mar. 2015.

28 NIE, W. *et al*. Responsive exosome nano-bioconjugates for synergistic cancer therapy. **Angewandte Chemie International Edition**, v. 59, n. 5, p. 2018–2022,

2020.

29 LARA, P. *et al.* Gold nanoparticle based double-labeling of melanoma extracellular vesicles to determine the specificity of uptake by cells and preferential accumulation in small metastatic lung tumors. **Journal of Nanobiotechnology**, v. 18, n. 1, p. 1–17, 2020.

30 KAMERKAR, S. *et al*. Exosomes facilitate therapeutic targeting of oncogenic KRAS in pancreatic cancer. **Nature**, v. 546, n. 7659, p. 498–503, 2017.

31 LARA, P. *et al.* Exploiting the natural properties of extracellular vesicles in targeted delivery towards specific cells and tissues. **Pharmaceutics**, v. 12, n. 11, p. 1–25, 2020.

32 YUAN, L. *et al*. Exosomes derived from microrna-148b-3p-overexpressing human umbilical cord mesenchymal stem cells restrain breast cancer progression. **Frontiers in Oncology**, v. 9, p. 1–14, 2019. DOI: 10.3389/fonc.2019.01076.

33 THÉRY, C. *et al*. Minimal information for studies of extracellular vesicles 2018 (MISEV2018): a position statement of the International Society for Extracellular Vesicles and update of the MISEV2014 guidelines. **Journal of Extracellular Vesicles**, v. 7, n. 1, 2018. DOI: 10.1080/20013078.2018.1535750.

34 ANTONYAK, M. A.; CERIONE, R. A. Emerging picture of the distinct traits and functions of microvesicles and exosomes. **Proceedings of the National Academy of Sciences of the United States of America**, v. 112, n. 12, p. 3589–3590, 2015.

35 HU, C. M. J. *et al.* “Marker-of-self” functionalization of nanoscale particles through a top-down cellular membrane coating approach. **Nanoscale**, v. 5, n. 7, 2013. DOI: 10.1039/c3nr00015j.

36 OLDENBORG, P. A. *et al*. Role of CD47 as a marker of self on red blood cells. **Science**, v. 288, n. 5473, p. 2051, 2000. DOI: 10.1126/science.288.5473.2051.

37 DEUSE, T. *et al*. The SIRP α – CD47 immune checkpoint in NK cells. **Journal of Experimental Medicine**, v. 218, n. 3, 2021. DOI: 10.1084/jem.20200839.

38 CHAO, M. P.; WEISSMAN, I. L.; MAJETI, R. The CD47-SIRPα pathway in cancer immune evasion and potential therapeutic implications. **Current Opinion in Immunology**, v. 24, n. 2, p. 225–232, 2012.

39 ZHAO, H. *et al.* CD47 promotes tumor invasion and metastasis in non-small cell lung cancer. **Scientific Reports**, v. 6, p. 1–11, 2016. DOI: 10.1038/srep29719.

40 SICK, E. *et al*. CD47 update: a multifaceted actor in the tumour microenvironment of potential therapeutic interest. **British Journal of Pharmacology**, v. 167, n. 7, p. 1415–1430, 2012.

41 HOSHINO, A. *et al*. Tumour exosome integrins determine organotropic metastasis. **Nature**, v. 527, n. 7578, p. 329–335, 2015.

42 HOBSON, D. W. Commercialization of nanotechnology. **Wiley Interdisciplinary Reviews**-nanomedicine and nanobiotechnology, v. 1, n. 2, p. 189–202, 2009.

43 WALSH, E. E. *et al*. Safety and Immunogenicity of Two RNA-based Covid-19 vaccine candidates. **New England Journal of Medicine**, v. 383, n. 25, p. 2439–2450, 2020.

44 PEREZ-HERRERO, E.; FERNANDEZ-MEDARDE, A. Advanced targeted therapies in cancer: drug nanocarriers, the future of chemotherapy. **European Journal of Pharmaceutics and Biopharmaceutics**, v. 93, p. 52–79, 2015. DOI: 10.1016/j.ejpb.2015.03.018.

45 DANHIER, F. To exploit the tumor microenvironment: since the EPR effect fails in the clinic, what is the future of nanomedicine? **Journal of Controlled Release**, v. 244,Pt. A, p. 108–121, 2016.

46 SPERLING, R. A.; PARAK, W. J. Surface modification, functionalization and bioconjugation of colloidal inorganic nanoparticles. **Philosophical Transactions of the Royal Society of London A**: mathematical, physical and engineering sciences, v. 368, n. 1915, p. 1333–1383, 2010.

47 CONDE, J. *et al*. Revisiting 30 years of biofunctionalization and surface chemistry of inorganic nanoparticles for nanomedicine. **Frontiers in Chemistry**, v. 2, p. 27, 2014. DOI: 10.3389/fchem.2014.00048.

48 HUANG, X. *et al*. Gold nanorods: from synthesis and properties to biological and biomedical applications. **Advanced Materials**, v. 21, n. 48, p. 4880–4910, 2009.

49 SINGH, R. K.; KIM, H. W. Inorganic nanobiomaterial drug carriers for medicine. **Tissue Engineering and Regenerative Medicine**, v. 10, n. 6, p. 296–309, 2013.

50 RIBOVSKI, L. *et al*. Gold nanorods and poly(amido amine) dendrimer thin film for biosensing. **Journal of Solid State Electrochemistry**, v. 23, n. 5, p. 1581–1591, 2019.

51 JORI, G.; SPIKES, J. D. Photothermal sensitizers: possible use in tumor therapy. **Journal of Photochemistry and Photobiology, B**: biology, v. 6, n. 1–2, p. 93–101, 1990.

52 HUANG, X.; JAIN, P. K.; EL-SAYED, I. H. Plasmonic photothermal therapy (PPTT) using gold nanoparticles. **Lasers in Medical Science** p. 217–228, 2008. DOI: 10.1007/s10103-007-0470-x.

53 MARANGONI, V. S. *et al*. Photothermia and activated drug release of natural cell membrane coated plasmonic gold nanorods and β-Lapachone. **ACS Applied Bio Materials**, v. 2, p. 728, 2019. DOI: 10.1021/acsabm.8b00603.

54 YANG, X. *et al*. Gold nanomaterials at work in biomedicine. **Chemical Reviews**, v. 115, n. 19, p. 10410–10488, 2015.

55 JAQUE, D. *et al*. Nanoparticles for photothermal therapies. **Nanoscale**, v. 6, n. 16, p. 9494–9530, 2014.

56 GONZÁLEZ-RUBIO, G. *et al*. Disconnecting symmetry breaking from seeded growth for the reproducible synthesis of high quality gold nanorods. **ACS Nano**, v. 13, n. 4, p. 4424–4435, 2019.

57 PRESCOTT, S. W.; MULVANEY, P. Gold nanorod extinction spectra. **Journal of Applied Physics**, v. 99, n. 12, p. 123504, 2006.

58 NIKOOBAKHT, B.; EL-SAYED, M. A. Preparation and growth mechanism of gold nanorods (NRs) using seed-mediated growth method. **Chemistry of Materials**, v. 15, n. 10, p. 1957–1962, 2003.

59 CHANG, H. H.; MURPHY, C. J. Mini gold nanorods with tunable plasmonic peaks beyond 1000 nm. **Chemistry of Materials**, v. 30, n. 4, p. 1427-1435, 2018. DOI: 10.1021/acs.chemmater.7b05310

60 SAU, T. K.; MURPHY, C. J. Seeded high yield synthesis of short Au nanorods in aqueous solution. **Langmuir**, v. 20, n. 15, p. 6414–6420, 2004.

61 KIM, F.; SONG, J. H.; YANG, P. Photochemical synthesis of gold nanorods. **Journal of the American Chemical Society**, v. 124, n. 48, p. 14316–14317, 2002.

62 PLACIDO, T. *et al*. Photochemical synthesis of water-soluble gold nanorods: the role of silver in assisting anisotropic growth. **Chemistry of Materials**, v. 21, n. 18, p. 4192–4202, 2009.

63 YE, X. C. *et al*. Improved size-tunable synthesis of monodisperse gold nanorods through the use of aromatic additives. **ACS nano**, v. 6, n. 3, p. 2804–2817, 2012.

64 JIA, H. *et al*. Synthesis of absorption-dominant small gold nanorods and their plasmonic properties. **Langmuir**, v. 31, n. 26, p. 7418-7426, 2015.

65 NIKOOBAKHT, B.; EL-SAYED, M. A. Surface-enhanced raman scattering studies on aggregated gold nanorods. **Journal of Physical Chemistry A**, v. 107, n. 18, p. 3372–3378, 2003.

66 SINGH, G.; MYASNICHENKO, V. S.; GLOMM, W. R. New insights into size-controlled reproducible synthesis of anisotropic Fe 3 O 4 nanoparticles: the importance of the reaction environment . **Materials Advances**, v. 1, n. 5, p. 1077–1082, 2020.

67 SCARABELLI, L. *et al*. A tips and tricks practical guide to the synthesis of gold nanorods. **Journal of Physical Chemistry Letters**, v. 6 , n. 21,p. 4270-4279 ,2015.

68 DICKERSON, E. B. *et al.* Gold nanorod assisted near-infrared plasmonic photothermal therapy (PPTT) of squamous cell carcinoma in mice. **Cancer Letters**, v. 269, n. 1, p. 57–66, 2008.

69 BURROWS, N. D. *et al*. Understanding the seed-mediated growth of gold nanorods through a fractional factorial design of experiments. **Langmuir**, v. 33, n. 8, p. 1891–1907, 2017.

70 JIANG, W. *et al*. Nanoparticle-mediated cellular response is size-dependent. **Nature Nanotechnology**, v. 3, n. 3, p. 145–150, 2008.

71 WAN, J. *et al*. Surface chemistry but not aspect ratio mediates the biological toxicity of gold nanorods in vitro and in vivo. **Scientific Reports**, v. 5, p. 1–16, 2015. DOI: 10.1038/srep11398.

72 XIE, X. *et al.* The effect of shape on cellular uptake of gold nanoparticles in the forms of stars, rods, and triangles. **Scientific Reports**, v. 7, n. 1, p. 1–9, 2017.

73 SONG, J. *et al*. Ultrasmall gold nanorod vesicles with enhanced tumor accumulation and fast excretion from the body for cancer therapy. **Advanced Materials**, v. 27, n. 33, p. 4910-4917, 2015.

74 CHEN, Y. S. *et al*. Miniature gold nanorods for photoacoustic molecular imaging in the second near-infrared optical window. **Nature Nanotechnology**, v. 14, 2019. DOI: 10.1038/s41565-019-0392-3.

75 BERCIAUD, S. *et al*. Observation of intrinsic size effects in the optical response of individual gold nanoparticles. **Nano Letters**, v. 5, n. 3, p. 515–518, 2005.

76 GEORGIEV, P. *et al.* Dependence of plasmon spectra of small gold nanoparticles from their size: an atomic force microscopy experimental approach. **Plasmonics**, v. 15, n. 2, p. 371–377, 2020.

77 HUANG, X.; EL-SAYED, M. A. Gold nanoparticles: optical properties and implementations in cancer diagnosis and photothermal therapy. **Journal of Advanced Research**, v. 1, n. 1, p. 13–28, 2010.

78 TOMASZEWSKA, E. *et al*. Detection limits of DLS and UV-Vis spectroscopy in characterization of polydisperse nanoparticles colloids. **Journal of Nanomaterials**, v. 2013, p. 313081, 2013. DOI: 10.1155/2013/313081.

79 PÉREZ-JUSTE, J. *et al*. Gold nanorods: synthesis, characterization and applications. **Coordination Chemistry Reviews**, v. 249, n. 17-18, p. 1870, 2005

80 LIU, M.; GUYOT-SIONNEST, P. Mechanism of Silver (I) -Assisted Growth of Gold Nanorods and Bipyramids. **Journal of Physical Chemistry B,** 2005 v.109, n. 47, p. 22192-2220, 2005.

81 WALSH, M. J. *et al*. Symmetry breaking and silver in gold nanorod growth. **ACS Nano**, v. 9, n. 1, p. 715–724, 2015.

82 TONG, W. *et al*. Control of symmetry breaking size and aspect ratio in gold nanorods: underlying role of silver nitrate. **Journal of Physical Chemistry C**, v. 121, n. 6, p. 3549–3559, 2017.

83 BURROWS, N. D. *et al*. Understanding the seed-mediated growth of gold nanorods through a fractional factorial design of experiments. **Langmuir**, v. 33, n. 8, p. 1891–1907, 2017.

84 SU, G.; YANG, C.; ZHU, J. J. Fabrication of gold nanorods with tunable longitudinal surface plasmon resonance peaks by reductive dopamine. **Langmuir**, v. 31, n. 2, p. 817–823, 2015.

85 VIGDERMAN, L.; ZUBAREV, E. R. High-yield synthesis of gold nanorods with longitudinal SPR peak greater than 1200 nm using hydroquinone as a reducing agent. **Chemistry of Materials**, v. 25, n. 8, p. 1450–1457, 2013.

86 WANG, T. *et al.* Two-photon luminescence properties of gold nanorods. **Biomedical Optics Express**, v. 4, n. 4, p. 584–595, 2013.

87 WANG, H. *et al*. In vitro and in vivo two-photon luminescence imaging of single gold nanorods. **Proceedings of the National Academy of Sciences of the United States of America**, v. 102, n. 44, p. 15752–15756, 2005.

88 DURR, N. J. *et al*. Two-photon luminescence imaging of cancer cells using molecularly targeted gold nanorods. **Nano Letters**, v. 7, n. 4, p. 941-945, 2007.

89 PÉREZ-JUSTE, J. *et al*. Electric-field-directed growth of gold nanorods in aqueous surfactant solutions. **Advanced Functional Materials**, v. 14, n. 6, p. 571–579, 2004.

90 CHEN, H. *et al.* Understanding the photothermal conversion efficiency of gold nanocrystals**. Small**, v. 6, n. 20, p. 2272-2280, 2010.

91 KAUR, P. *et al*. Hyperthermia using nanoparticles - promises and pitfalls. **International Journal of Hyperthermia**, v. 32, n. 1, p. 76–88, 2016.

92 XIE, Z. *et al*. Black phosphorus-based photothermal therapy with aCD47-mediated immune checkpoint blockade for enhanced cancer immunotherapy. **Light**: science & applications, v. 9, n. 1, p. 161, 2020.

93 FALAGAN-LOTSCH, P.; GRZINCIC, E. M.; MURPHY, C. J. One low-dose exposure of gold nanoparticles induces long-term changes in human cells. **Proceedings of the National Academy of Sciences of the United States of America**, v. 113, n. 47, p. 13318–13323, 2016.

94 KANG, X. *et al*. Photothermal therapeutic application of gold nanorods-porphyrin-trastuzumab complexes in HER2-positive breast cancer. **Scientific Reports**, v. 7, 2017. DOI: 10.1038/srep42069.

95 KNOP, K. *et al*. Poly(ethylene glycol) in drug delivery: pros and cons as well as potential alternatives. **Angewandte Chemie International Edition**, v. 49, n. 36, p. 6288–6308, 2010.

96 KAUSCHER, U. *et al*. Gold nanocluster extracellular vesicle supraparticles: self-assembled nanostructures for three-dimensional uptake visualization. **Langmuir**, v. 36, n. 14, p. 3912–3923, 2020.

97 COMPARETTI, E. J. *et al*. Cancer cell membrane-derived nanoparticles improve the activity of gemcitabine and paclitaxel on pancreatic cancer cells and coordinate immunoregulatory properties on professional antigen-presenting cells. **Materials Advances**, v. 1, n. 6, 2020. DOI: 10.1039/D0MA00367K

98 ZHANG, Y. *et al*. Macrophage-membrane-coated nanoparticles for tumor-targeted chemotherapy. **Nano Letters**, v. 18, n. 3, p. 1908–1915, 2018.

99 XUAN, M. *et al*. Macrophage cell membrane camoufl aged mesoporous silica nanocapsules for in vivo cancer therapy. **Advanced Healthcare Materials**, v. 4, n. 11, p. 1645–1652, 2015.

100 BELHADJ, Z. *et al*. A combined “eat me/don’t eat me” strategy based on extracellular vesicles for anticancer nanomedicine. **Journal of Extracellular Vesicles**, v. 9, n. 1, 2020. DOI: 10.1080/20013078.2020.1806444.

101 FUHRMANN, G. *et al*. Active loading into extracellular vesicles significantly improves the cellular uptake and photodynamic effect of porphyrins. **Journal of Controlled Release**, 2015.

102 XIONG, F. *et al*. Pursuing specific chemotherapy of orthotopic breast cancer with lung metastasis from docking nanoparticles driven by bioinspired exosomes**. Nano Letters**, v. 19 , n. 5, p. 3256-3266 2019.

103 VALADI, H. *et al*. Exosome-mediated transfer of mRNAs and microRNAs is a novel mechanism of genetic exchange between cells. **Nature Cell Biology**, v. 9, n. 6, p. 654–659, 2007.

104 SUNG, B. H. *et al*. A live cell reporter of exosome secretion and uptake reveals pathfinding behavior of migrating cells. **Nature Communications**, v. 11, n. 1, p. 1–15, 2020.

105 THÉRY, C.; ZITVOGEL, L.; AMIGORENA, S. Exosomes: composition, biogenesis and function. **Nature Reviews Immunology**, v. 2, n. 8, p. 569–579, 2002.

106 YONG, T. *et al*. Tumor exosome-based nanoparticles are efficient drug carriers for chemotherapy. **Nature Communications**, v. 10, n. 1, p. 3838, 2019.

107 SEO, N. *et al*. Activated CD8+ T cell extracellular vesicles prevent tumour progression by targeting of lesional mesenchymal cells. **Nature Communications**, v. 9, n. 1, p. 1–11, 2018.

108 LUK, B. T. *et al*. Interfacial interactions between natural RBC membranes and synthetic polymeric nanoparticles. **Nanoscale**, v. 6, n. 5, p. 2730, 2014.

109 SUN, H. *et al*. Cancer cell membrane-coated gold nanocages with hyperthermia-triggered drug release and homotypic target inhibit growth and metastasis of breast cancer. **Advanced Functional Materials**, v. 27, n. 3, 2017.

110 MEHTALA, J. G. *et al*. Citrate-stabilized gold nanorods. **Langmuir**, v. 30 , n. 46, p. 13727-13730, 2014.

111 THERY, C.: CLAYTON, A.; AMIGORENA, S.; RAPOSO,G. Isolation and characterization of exosomes from cell culture supernatants. **Current Protocols in Cell Biology**, p. 1–29, 2006. DOI: 10.1002/0471143030.cb0322s30.

112 XUAN, M. *et al*. Macrophage cell membrane camouflaged Au nanoshells for in vivo prolonged circulation life and enhanced cancer photothermal therapy. **ACS Applied Materials and Interfaces**, v. 8, n. 15, p. 9610–9618, 2016.

113 ZHENG, P. *et al*. Tumor-associated macrophages-derived exosomes promote the migration of gastric cancer cells by transfer of functional Apolipoprotein E. **Cell Death and Disease**, v. 9, n. 4, p. 434, 2018.

114 KHONGKOW, M. *et al*. Surface modification of gold nanoparticles with neuron-targeted exosome for enhanced blood–brain barrier penetration. **Scientific Reports**, v. 9, n. 1, p. 1–9, 2019.

115 THÉRY, C. *et al*. Exosomes : composition , biogenesis and function. **Nature Reviews Immunology**, v. 2, n. 8, p. 569-79, 2002. DOI: 10.1038/nri855.

116 MEISTER, M.; TIKKANEN, R. Endocytic trafficking of membrane-bound cargo: a flotillin point of view. **Membranes**, v. 4, n. 3, p. 356–371, 2014.

117 MERCKX, G. *et al*. Angiogenic effects of human dental pulp and bone marrow-derived mesenchymal stromal cells and their extracellular vesicles. **Cells**, v. 9, n. 2, p. 312, 2020.

118 LLORENTE, A. *et al*. Molecular lipidomics of exosomes released by PC-3 prostate cancer cells. **Biochimica et Biophysica Acta** - molecular and cell biology of lipids, v. 1831, n. 7, p. 1302–1309, 2013.

119 SINGHTO, N.; VINAIPHAT, A.; THONGBOONKERD, V. Discrimination of urinary exosomes from microvesicles by lipidomics using thin layer liquid chromatography (TLC) coupled with MALDI-TOF mass spectrometry. **Scientific Reports**, v. 9, n. 1, p. 1–11, 2019.

120 HU, M. *et al*. Dark-field microscopy studies of single metal nanoparticles: understanding the factors that influence the linewidth of the localized surface plasmon resonance. **Journal of Materials Chemistry**, v. 18, n. 17, p. 1949, 2008.

121 MEHTALA, J. G.; WEI, A. Nanometric resolution in the hydrodynamic size analysis of ligand-stabilized gold nanorods. **Langmuir**, v. 30, n. 46, p. 13737–13743, 2014.

122 MINNES, R. *et al*. Using attenuated total reflection-fourier transform infra-red (ATR-FTIR) spectroscopy to distinguish between melanoma cells with a different metastatic potential. **Scientific Reports**, v. 7, n. 1, p. 1–7, 2017.

123 SAEEDIMASINE, M. *et al*. Role of lipid composition on the structural and mechanical features of axonal membranes: a molecular simulation study. **Scientific Reports**, v. 9, n. 1, p. 1–12, 2019.

124 ICARD, P.; POULAIN, L.; LINCET, H. Understanding the central role of citrate in the metabolism of cancer cells. **Biochimica et Biophysica Acta** - reviews on cancer, v. 1825, n. 1, p. 111–116, 2012.

125 MOROS, M. *et al*. Gold nanorods and nanoprisms mediate different photothermal cell death mechanisms in vitro and in vivo. **ACS Applied Materials and Interfaces**, v. 12, n. 12, p. 13718–13730, 2020.

126 MINAI, L.; YEHESKELY-HAYON, D.; YELIN, D. High levels of reactive oxygen species in gold nanoparticle-targeted cancer cells following femtosecond pulse irradiation. **Scientific Reports**, v. 3, p. 1–7, 2013. DOI: 10.1038/srep02146.

127 JOSHI, B. S.; ZUHORN, I. S. Heparan sulfate proteoglycan-mediated dynamin-dependent transport of neural stem cell exosomes in an in vitro blood–brain barrier model. **European Journal of Neuroscience**, 2020. DOI: 10.1111/ejn.14974.

128 BARRÈS, C. *et al*. Galectin-5 is bound onto the surface of rat reticulocyte exosomes and modulates vesicle uptake by macrophages. **Blood**, v. 115, n. 3, p. 696–705, 2010.

129 MAYOR, S.; PAGANO, R. E. Pathways of clathrin-independent endocytosis. **Nature Reviews Molecular Cell Biology**, v. 8, n. 8, p. 603–612, 2007.

130 COSTA VERDERA, H. *et al*. Cellular uptake of extracellular vesicles is mediated by clathrin-independent endocytosis and macropinocytosis. **Journal of Controlled Release**, v. 266, p. 100–108, 2017. DOI: 10.1016/j.jconrel.2017.09.019.

131 MORDUE, K. E. *et al*. CD47 surface stability is sensitive to actin disruption prior to inclusion within the band 3 macrocomplex. **Scientific Reports**, v. 7, n. 1, p. 1–14, 2017.

132 REBRES, R. A.; KAJIHARA, K.; BROWN, E. J. Novel CD47-dependent intercellular adhesion modulates cell migration. **Journal of Cellular Physiology**, v. 205, n. 2, p. 182–193, 2005.

133 SUN, H. *et al*. Cancer-cell-biomimetic nanoparticles for targeted therapy of homotypic tumors. **Advanced Materials**, v. 28, n. 43, p. 9581–9588, 2016.

134 MERCIER, V. *et al*. ALG-2 interacting protein-X (Alix) is essential for clathrin-independent endocytosis and signaling. **Scientific Reports**, v. 6, n. 26986, p. 1–15, 2016. DOI: 10.1038/srep26986

135 PARODI, A. *et al*. Synthetic nanoparticles functionalized with biomimetic leukocyte membranes possess cell-like functions. **Nature Nanotechnology**, v. 8, n. 1, p. 61–68, 2012.

136 HOSHINO, A. *et al*. Tumour exosome integrins determine organotropic metastasis. **Nature**, v. 527, n. 7578, p. 329–335, 2015.

137 NIE, W. *et al*. Responsive exosome nano-bioconjugates for synergistic cancer therapy. **Angewandte Chemie International Edition**, v. 59, n. 5, p. 2018–2022, 2020.

138 SCHROEDER, A. *et al*. Treating metastatic cancer with nanotechnology. **Nature Reviews Cancer**, v. 12, n. 1, p. 39–50, 2012.

139 REDIG, A. J.; MCALLISTER, S. S. Breast cancer as a systemic disease: a view of metastasis. **Journal of Internal Medicine**, v. 274, n. 2, p. 113–126, 2013.

140 CHEN, Q. *et al*. An imagable and photothermal “Abraxane-Like” nanodrug for combination cancer therapy to treat subcutaneous and metastatic breast tumors. **Advanced Materials**, v. 27, n. 5, p. 903–910, 2015.

141 KUNDRANDA, M. N.; NIU, J. Albumin-bound paclitaxel in solid tumors: clinical development and future directions. **Drug Design, Development and Therapy**, v. 9, p. 3767–3777, 2015. DOI: 10.2147/DDDT.S88023.

142 BANERJEE, S. *et al*. Current advances of tubulin inhibitors in nanoparticle drug delivery and vascular disruption/angiogenesis. **Molecules**, v. 21, n. 11, p. 1468, 2016.

143 DANHIER, F. *et al*. Paclitaxel-loaded PEGylated PLGA-based nanoparticles: in vitro and in vivo evaluation. **Journal of Controlled Release**, v. 133, n. 1, p. 11–17, 2009.

144 CHENG, J. *et al*. Formulation of functionalized PLGA–PEG nanoparticles for in vivo targeted drug delivery. **Biomaterials**, v. 28, n. 5, p. 869–876, 2007.

145 DANHIER, F. *et al*. PLGA-based nanoparticles: an overview of biomedical applications. **Journal of Controlled Release**, v. 161, n. 2, p. 505–522, 2012.

146 KHALDOYANIDI, S. K. *et al*. MDA-MB-435 human breast carcinoma cell homo- and heterotypic adhesion under flow conditions is mediated in part by Thomsen-Friedenreich antigen-galectin-3 interactions. **Journal of Biological Chemistry**, v. 278, n. 6, p. 4127–4134, 2003.

147 JANISZEWSKA, M.; PRIMI, M. C.; IZARD, T. Cell adhesion in cancer: beyond the migration of single cells. **Journal of Biological Chemistry**, v. 295, n. 8, p. 2495–2505, 2020.

148 JIANG, Q. *et al.* Erythrocyte-cancer hybrid membrane-camouflaged melanin nanoparticles for enhancing photothermal therapy efficacy in tumors. **Biomaterials**, v. 192, p. 292–308, 2019. DOI: 10.1016/j.biomaterials.2018.11.021

149 NIE, D. *et al.* Cancer-Cell-Membrane-Coated Nanoparticles with a Yolk-Shell Structure Augment Cancer Chemotherapy. **Nano Letters**, v. 20, n. 2, p. 936–946, 2020.

150 SAKAMOTO, H. *et al*. PAI-1 derived from cancer-associated fibroblasts in esophageal squamous cell carcinoma promotes the invasion of cancer cells and the migration of macrophages. **Laboratory Investigation**, v. 101, p. 353, 2020. DOI: 10.1038/s41374-020-00512-2

151 FANG, R. H. *et al*. Cancer cell membrane-coated nanoparticles for anticancer vaccination and drug delivery. **Nano Letters**, v. 14, n. 4, p. 2181–2188, 2014.

152 FESSI, H. *et al*. Nanocapsule formation by interfacial polymer deposition following solvent displacement. **International Journal of Pharmaceutics**, v. 55, n. 1, p. R1-R4, 1989.

153 LIU, Y. *et al*. Cell membrane coating technology: a promising strategy for biomedical applications. **Nano-Micro Letters**, v. 11, n.1, p.1-46, 2019.

154 HERNÁNDEZ-GIOTTONINI, K. Y. *et al*. PLGA nanoparticle preparations by emulsification and nanoprecipitation techniques: effects of formulation parameters. **RSC Advances**, v. 10, n. 8, p. 4218–4231, 2020.

155 GASPARINI, G. *et al*. Preparation and characterization of PLGA particles for subcutaneous controlled drug release by membrane emulsification. **Colloids and Surfaces B:** biointerfaces, v. 61, n. 2, p. 199–207, 2008.

156 GAO, W. *et al.* Surface functionalization of gold nanoparticles with red blood cell membranes. **Advanced Materials**, v. 25, n. 26, p. 3549–3553, 2013.

157 HU, C. M. J. *et al*. Nanoparticle biointerfacing by platelet membrane cloaking. **Nature**, v. 526, n. 7571, p. 118–121, 2015.

158 BERSHTEYN, A. *et al*. Polymer-supported lipid shells, onions, and flowers. **Soft Matter**, v. 4, n. 9, p. 1787–1791, 2008.

159 GARCÍA-DÍAZ, M.; FOGED, C.; NIELSEN, H. M. Improved insulin loading in poly(lactic-co-glycolic) acid (PLGA) nanoparticles upon self-assembly with lipids. **International Journal of Pharmaceutics**, v. 482, n. 1–2, p. 84–91, 2015.

160 STEWART, P. L. Cryo-electron microscopy and cryo-electron tomography of nanoparticles. **WIREs Nanomedicine and Nanobiotechnology**, v. 9, n. 2, p. e1417, 2017.

161 HACKER, C. *et al*. Nanoparticle suspensions enclosed in methylcellulose: a new approach for quantifying nanoparticles in transmission electron microscopy. **Scientific Reports**, v. 6, 2016. DOI: 10.1038/srep25275.

162 SPIZZO, G. *et al*. EpCAM expression in primary tumour tissues and metastases: an immunohistochemical analysis. **Journal of Clinical Pathology**, v. 64, n. 5, p.

415-420, 2011.

163 EBERLEIN, C. *et al*. E-Cadherin and EpCAM expression by NSCLC tumour cells associate with normal fibroblast activation through a pathway initiated by integrin αvβ6 and maintained through TGFβ signalling. **Oncogene**, v. 34, n. 6, p. 704–716, 2015.

164 HOSEIN, A. N. *et al*. A functional in vitro model of heterotypic interactions reveals a role for interferon-positive carcinoma associated fibroblasts in breast cancer. **BMC Cancer**, v. 15, n. 1, p. 1–11, 2015.

165 PRESTON, R. A.; MURPHY, R. F.; JONES, E. W. Apparent endocytosis of fluorescein isothiocyanate-conjugated dextran by Saccharomyces cerevisiae reflects uptake of low molecular weight impurities, not dextran. **Journal of Cell Biology**, v. 105, n. 5, p. 1981–1987, 1987.

166 DOS SANTOS, T. *et al.* Quantitative assessment of the comparative nanoparticle-uptake efficiency of a range of cell lines. **Small**, v. 7, n. 23, p. 3341–3349, 2011.

167 PADDOCK, S. W. Principles and practices of laser scanning confocal microscopy. **Applied Biochemistry and Biotechnology** - part b molecular biotechnology, v. 16, n. 2, p. 127–149, 2000.

168 XIE, X. *et al*. Overcoming drug-resistant lung cancer by paclitaxel loaded tetrahedral DNA nanostructures. **Nanoscale**, v. 10, n. 12, p. 5457–5465, 2018.

169 MELO, S. A. *et al*. Glypican-1 identifies cancer exosomes and detects early pancreatic cancer. **Nature**, v. 523, n. 7559, p. 177–182, 2015.

170 STOORVOGEL, W. *et al*. The biogenesis and functions of exosomes. **Traffic**, v. 3, n. 5, p. 321–330, 2002.

171 VALADI, H. *et al.* Exosome-mediated transfer of mRNAs and microRNAs is a novel mechanism of genetic exchange between cells. **Nature Cell Biology**, v. 9, n. 6, p. 654–659, 2007.

172 YÁÑEZ-MÓ, M. *et al*. Biological properties of extracellular vesicles and their physiological functions. **Journal of Extracellular Vesicles**, v. 4, n. 2015, p. 1–60, 2015.

173 LANG, H.-L. *et al*. Glioma cells enhance angiogenesis and inhibit endothelial cell apoptosis through the release of exosomes that contain long non-coding RNA CCAT2. **Oncology Reports**, v. 38, n. 2, p. 785–798, 2017.

174 COSTA-SILVA, B. *et al*. Pancreatic cancer exosomes initiate pre-metastatic niche formation in the liver. **Nature Cell Biology**, v. 17, n. 6, p. 816–826, 2015.

175 ANDREOLA, G. *et al*. Induction of lymphocyte apoptosis by tumor cell secretion of FasL-bearing microvesicles. **Journal of Experimental Medicine**, v. 195, n. 10, p.

1303–1316, 2002.

176 BEBAWY, M. *et al*. Membrane microparticles mediate transfer of P-glycoprotein to drug sensitive cancer cells. **Leukemia**, v. 23, n. 9, p. 1643–1649, 2009.

177 VIAUD, S. *et al*. Dendritic cell-derived exosomes promote natural killer cell activation and proliferation: A role for NKG2D ligands and IL-15Rα. **PLoS ONE**, v. 4, n. 3, p. e4942, 2009.

178 ZHOU, J. *et al.* Exosomes released from tumor-associated macrophages transfer miRNAs that induce a Treg/Th17 cell imbalance in epithelial ovarian cancer. **Cancer Immunology Research**, v. 6, n. 12, p. 1578–1592, 2018.

179 ARMSTRONG, J. P. K.; HOLME, M. N.; STEVENS, M. M. Re-engineering extracellular vesicles as smart nanoscale therapeutics. **ACS Nano**, v. 11, n. 1, p. 69–83, 2017.

180 GIMONA, M. et al. Manufacturing of human extracellular vesicle-based therapeutics for clinical use. **International Journal of Molecular Sciences**, v. 18, n. 6, 2017.

181 GARDINER, C. *et al*. Techniques used for the isolation and characterization of extracellular vesicles: results of a worldwide survey. **Journal of Extracellular Vesicles**, v. 5, n. 1, 2016. DOI: 10.3402/jev.v5.32945.

182 ROOD, I. M. *et al*. Comparison of three methods for isolation of urinary microvesicles to identify biomarkers of nephrotic syndrome. **Kidney International**, v. 78, n. 8, p. 810–816, 2010.

183 BUSATTO, S. *et al*. Tangential flow filtration for highly efficient concentration of extracellular vesicles from large volumes of fluid. **Cells**, v. 7, n. 12, p. 273, 2018.

184 PAGANINI, C. *et al.* Scalable production and isolation of extracellular vesicles: available sources and lessons from current industrial bioprocesses. **Biotechnology Journal**, v. 14, n. 10, 2019. DOI: 10.1002/biot.201800528.

185 LI, P. *et al.* Progress in exosome isolation techniques. **Theranostics**, v. 7, n. 3, p. 789–804, 2017.

186 LANE, R. E. *et al*. Analysis of exosome purification methods using a model liposome system and tunable-resistive pulse sensing. **Scientific Reports**, v. 5, 2015. DOI: 10.1038/srep07639.

187 BATTISTELLI, M.; FALCIERI, E. Apoptotic bodies: particular extracellular vesicles involved in intercellular communication. **Biology**, v. 9, n. 1, 2020. DOI: 10.3390/biology9010021.

188 PATEL, D. B. *et al*. Impact of cell culture parameters on production and vascularization bioactivity of mesenchymal stem cell-derived extracellular vesicles. **Bioengineering & Translational Medicine**, v. 2, n. 2, p. 170–179, 2017.

189 BOSCH, S. *et al.* Trehalose prevents aggregation of exosomes and cryodamage. **Scientific Reports**, v. 6, n. 1, p. 1–11, 2016.

190 LUDWIG, A. K. *et al*. Precipitation with polyethylene glycol followed by washing and pelleting by ultracentrifugation enriches extracellular vesicles from tissue culture supernatants in small and large scales. **Journal of Extracellular Vesicles**, v. 7, n. 1, 2018.

191 PATEL, G. K. *et al*. Comparative analysis of exosome isolation methods using culture supernatant for optimum yield, purity and downstream applications. **Scientific Reports**, v. 9, n. 1, p. 1–10, 2019.

APPENDIX A – Support information

Lipid composition by planar chromatography analysis

The lipid composition of the vesicles was assessed by planar chromatography with flame ionization (Iatroscan MK-VI, Iatron, Japan). Lipids standards HC/WE (aliphatic hydrocarbons/ester), KET (ketones), TAG (triglycerides), FFA (free fatty acids), ALC (aliphatic alcohol free), ST (sterol), AMPL (mobile polar lipids in ketone) and PL (phospholipids) were obtained from Sigma-Aldrich and all other chemicals and solvents were of analytical grade. RAW264.7 cell membranes and extracellular vesicles were resuspended in chloroform (Synth) after ultracentrifugation. The lipids samples were resolved in subsequent elution stages with an increase of solvent's polarity.

Cellular uptake by flow cytometry

In 12 or 24-well plates, $2x10^5$ cells/ well were seeded and grown for 24 hours. Medium was removed, followed by the incubation in the same parameters as the uptake studies by Image Xpress. After incubation, cells were washed once with 1X PBS and detached by trypsinization for FC3H and HTC, and by scraper for RAW264.7. Samples were collected and centrifuged (500 x g, 10 min) and washed 1x with Sheath Fluid (BD Bioscience) supplemented with 0.5% (w/v) bovine serum albumin and kept on ice prior flow cytometry measurements. All measurements were performed in a BD FACSCalibur™ equipped with one laser (488 nm) and excitation measured using channel FL1 (530 nm). Data analysis were performed using Flowing and Prisma softwares.

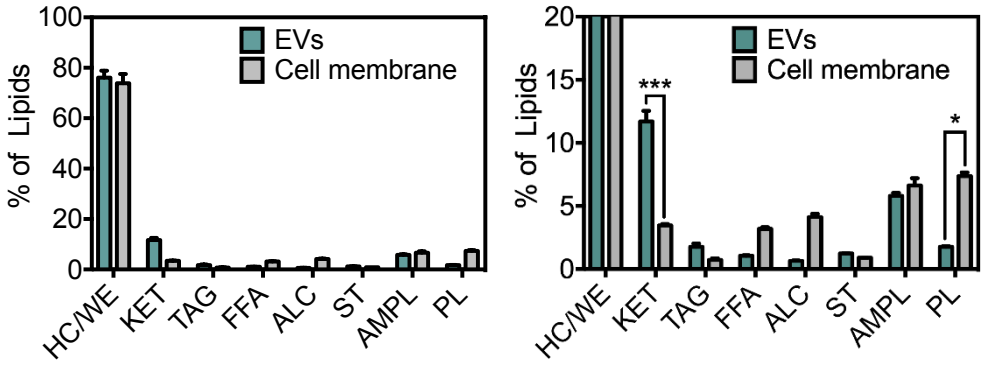

Figure S3.1 - Lipid composition analysis by Iatroscan of the isolated extracellular vesicles and cell membrane of RAW264.7. (Statistical ANOVA analysis with Tukey comparisons, error bars represent the standard error, * p<0.05; **p<0.01; ***p<0.001).

Source: By the author.

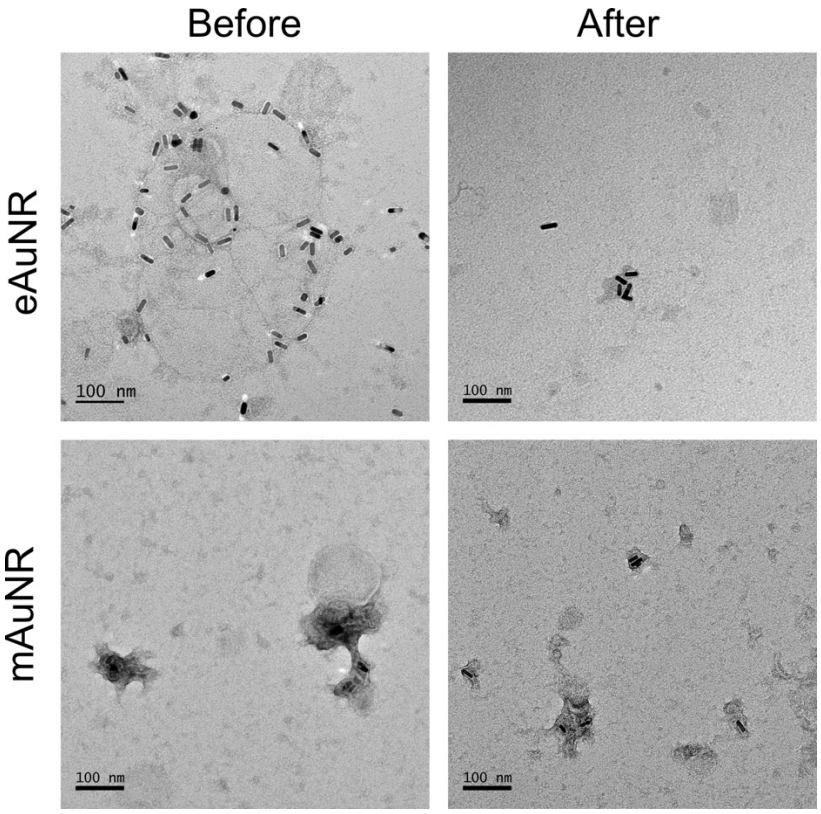

Figure S3.2 - TEM images by negative stainning before and after the extrusion, using a 200 nm pore size memmbrane, of eAuNR and mAuNR nanoparticles.

Source: By the author.

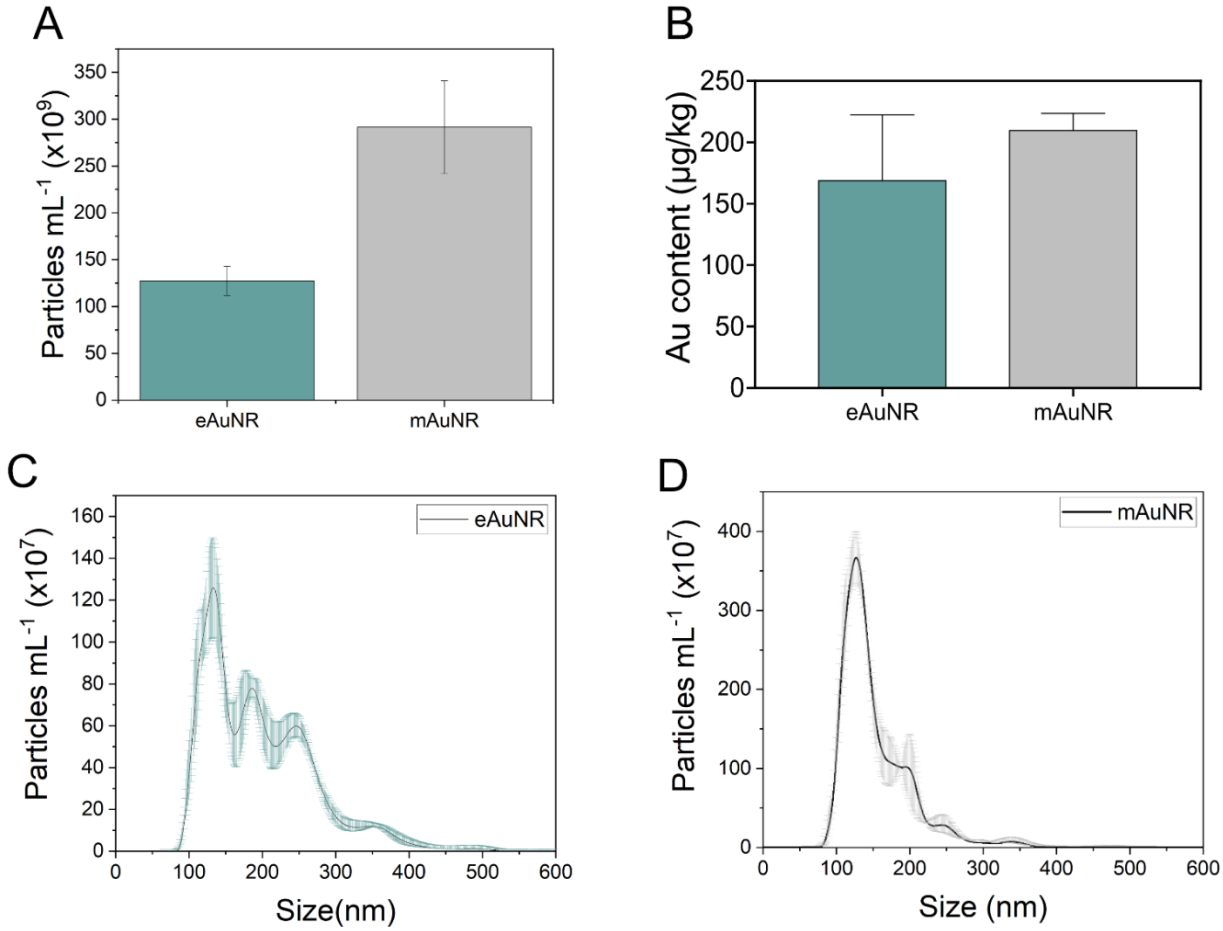

Figure S3.3 - NTA and ICP-MS analysis of eAuNR and mAuNR. A) Concentration of nanoparticles in three independent synthesis and B) gold content by ICP-MS of two independent synthesis of eAuNR and mAuNR. Size distribution by NTA of C) eAuNR and D) mAuNR.

Source: By the author.

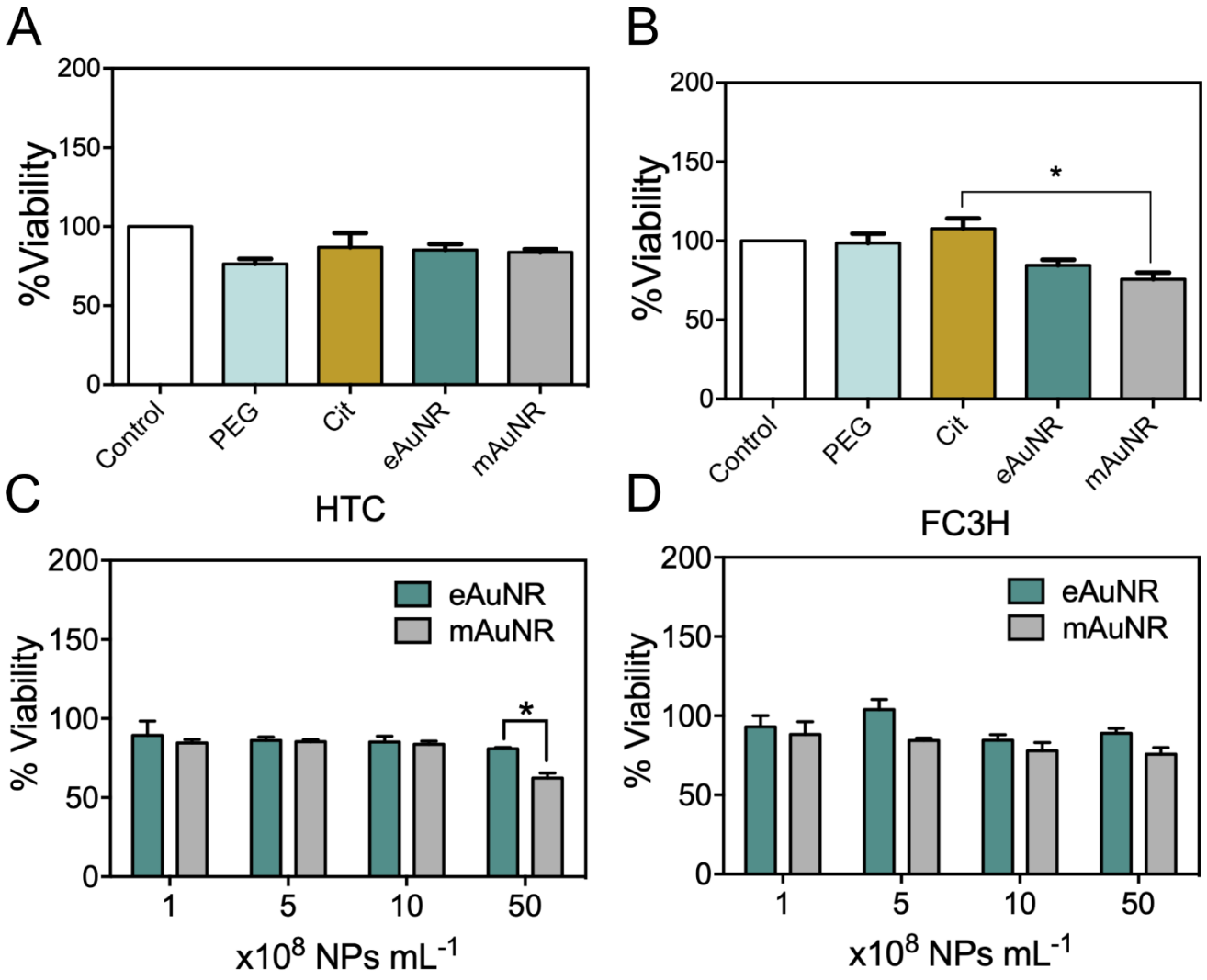

Figure S3.4 - Cell viability studies of A,C) cancer (HTC) and B,D) healthy (FC3H) hepatic cell lines exposure to the nanoparticles at 24 hours (Statistical ANOVA analysis with Tukey comparisons, error bars represent the standard error, * $p<0.05$; ** $p<0.01$; *** $p<0.001$).

Source: By the author.

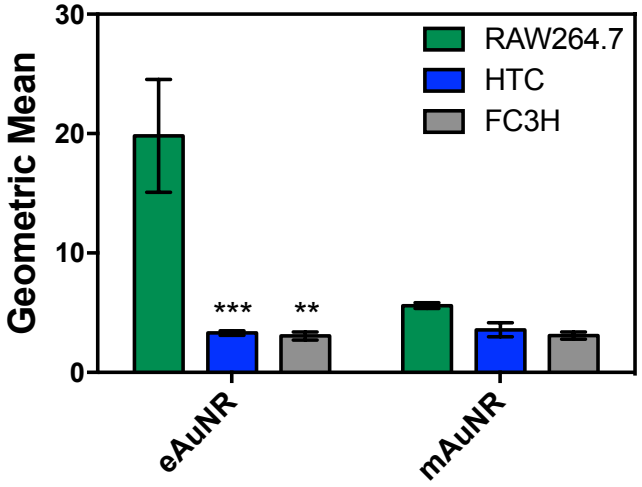

Figure S3.5 - Uptake studies of the source cell and hepatic cell lines by flow cytometry (Statistical ANOVA analysis with Tukey comparisons, error bars represent the standard error, * $p<0.05$; ** $p<0.01$; *** $p<0.001$).

Source: By the author.

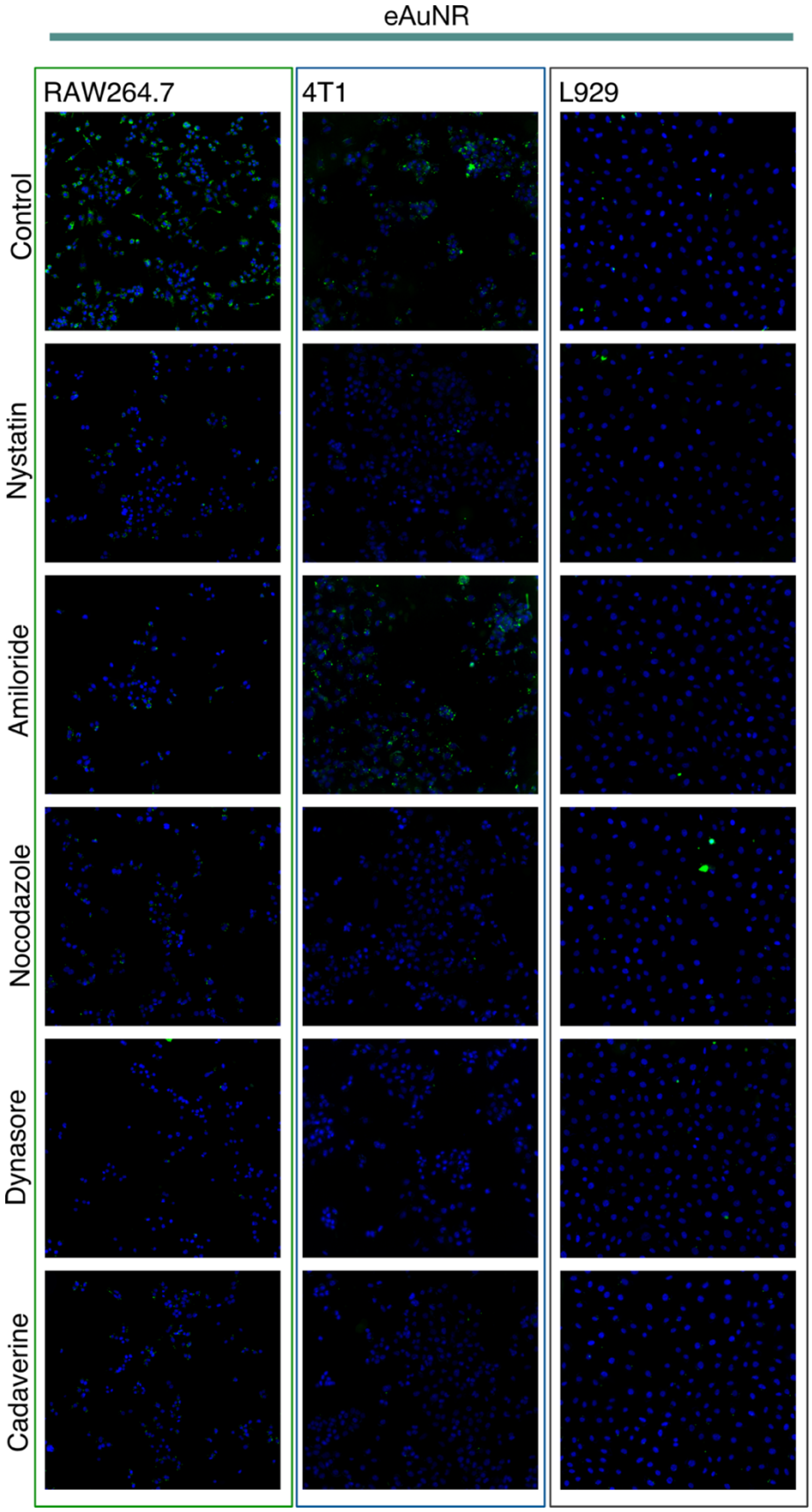

Figure S3.6 - Endocytosis studies of eAuNR in RAW264.7, 4T1 and L929 cells by automated fluorescence microscopy.

Source: By the author.

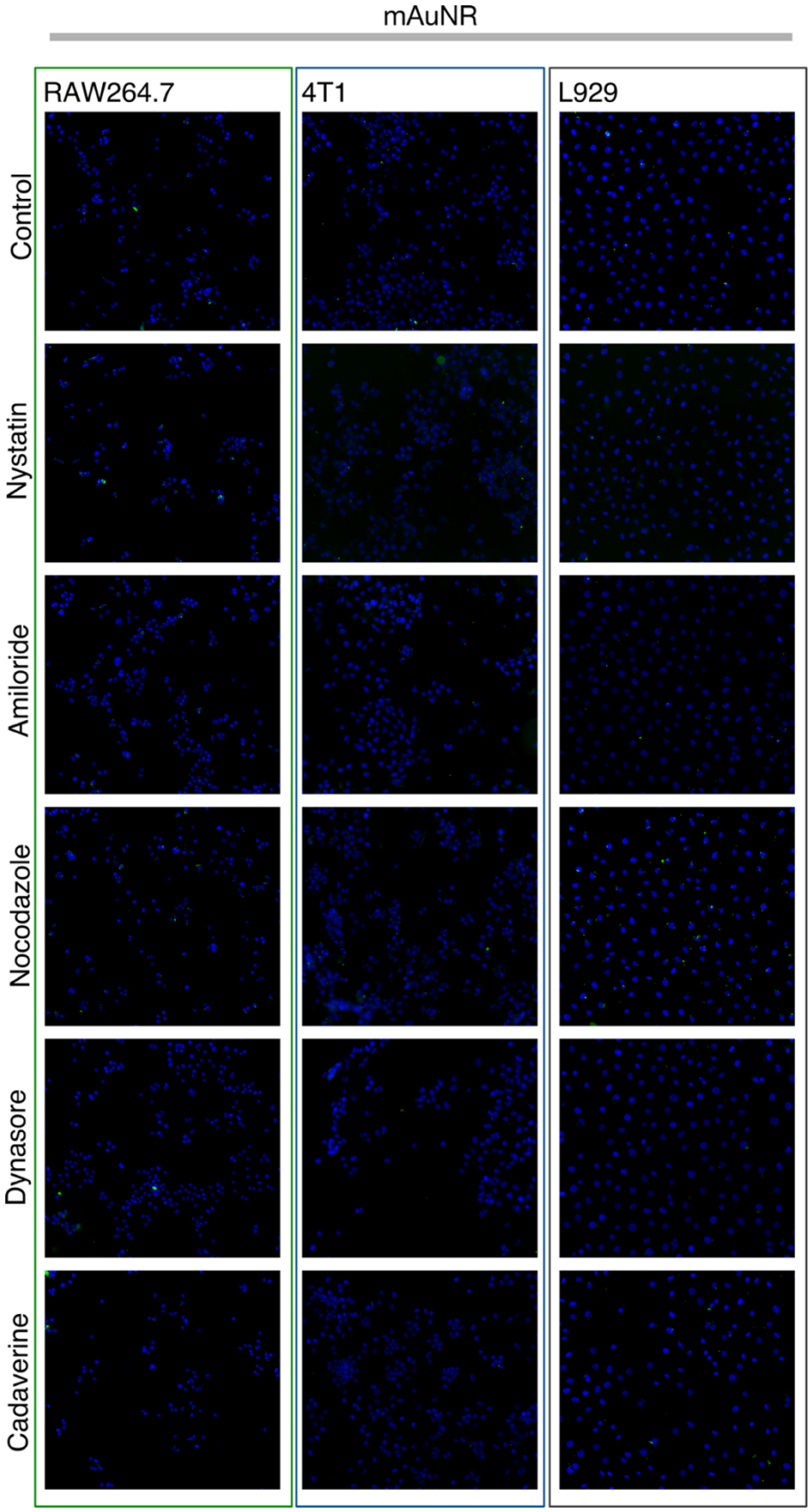

Figure S3.7 - Endocytosis studies of mAuNR in RAW264.7, 4T1 and L929 cells by automated fluorescence microscopy.

Source: By the author.

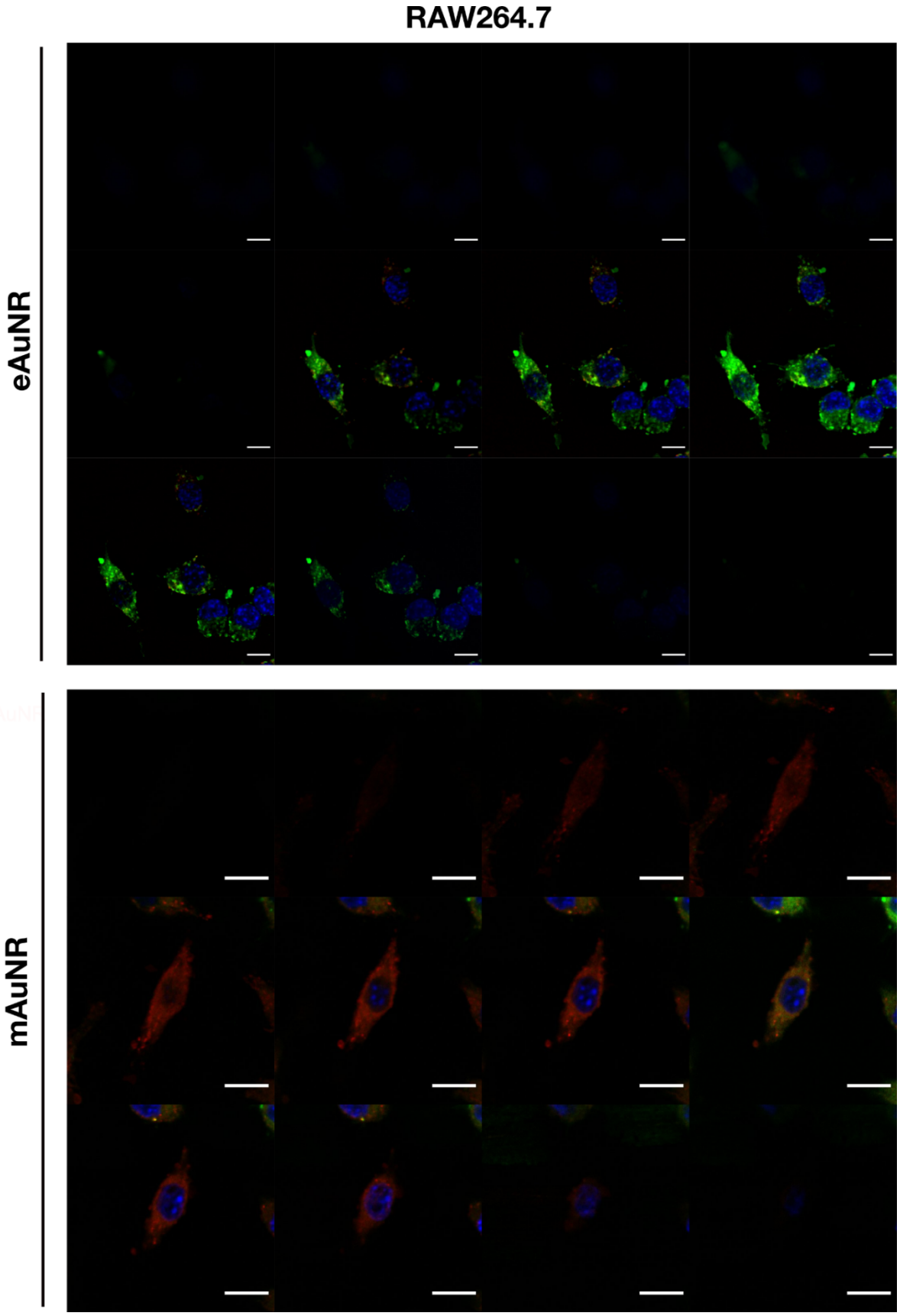

Figure S3.8 - Slices of cell uptake studies of eAuNR and mAuNR in RAW264.7 by confocal laser microscopy (Scale Bar 10μm).

Source: By the author.

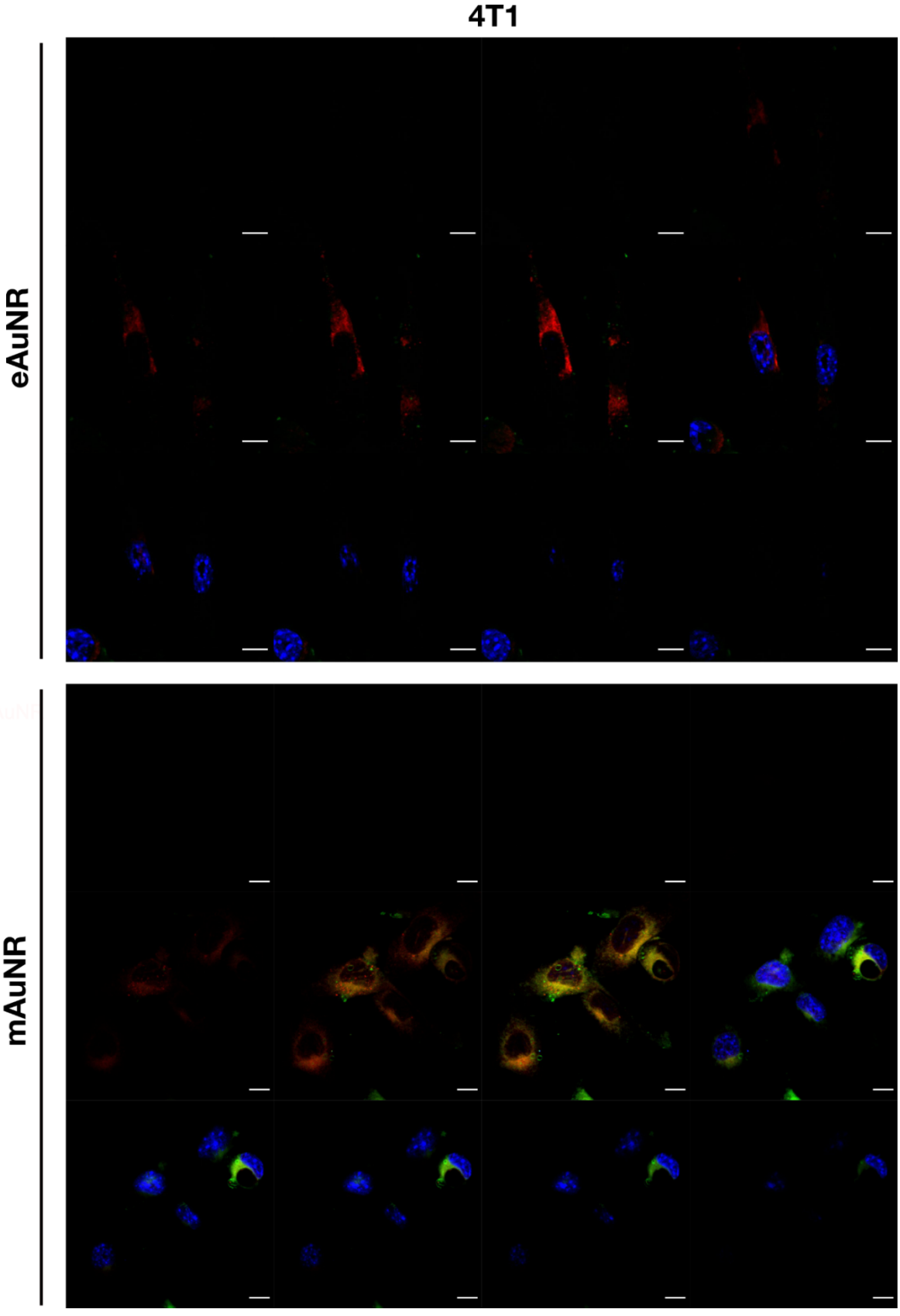

Figure S3.9 - Slices of cell uptake studies of eAuNR and mAuNR in 4T1 by confocal laser microscopy (Scale Bar 10μm).

Source: By the author.

APPENDIX B – Support information

High-performance liquid chromatography (HPLC) for paclitaxel NCs quantification

The HPLC method was validated according to the International Council for Harmonisation of Technical Requirements for Pharmaceuticals for Human Use (ICH) Q2(R1) guidelines by the European Medicines Agency (EMEA). Waters® e2695 HPLC system equipped with the 2489 UV-Visible detector using a Brownlee Analytical C8 (150 x 4.6 mm, 5 µm) and precolumn Brownlee Analytical C8 (10 x 4 mm, 5 µm) from PerkinElmer were used for the analysis of paclitaxel samples. Mobile phase was composed of (50:50, v/v) acetonitrile and ddH_2O and flow rate was 1 mL min^{-1}. Working standard solutions (paclitaxel from 0.5 to 25 µg mL^{-1}) were prepared using 1mL of mobile phase and filtered with 0.22 µm pore-size nylon filter.

Table S4.1 - Analytical parameters of the validated method using HPLC.

Parameter	Paclitaxel
Analytical curve	y = 107035.91x - 1963.10
Linear range (µg mL^{-1})	0.5 - 25
LOQ (µg mL^{-1})	0.1
Accuracy (ER%)	≤ 3.4
Precision (CV%)	0.5-3.3

Souce: By the author.

For the encapsulation efficiency (EE), a volume of NCs was ultracentrifuged (100000 g, 2 hours, 4 °C) in a Beckman Coulter Optima L-90k, rotor TLA110. Supernatant was removed from the tube and the pellet was resuspended in the same initial volume with acetonitrile. 100 µL was transferred to a new tube and acetonitrile was evaporated under dry nitrogen. The sample was resuspended in mobile phase filtered with 0.22 µm as stated before for standard samples. Three batches (n=3)

were used to determine encapsulation efficiency and calculated in the following equation:

$$EE(\%) = \frac{amount\ of\ PTX\ in\ NCs}{(amount\ of\ PTX\ in\ NCs + amount\ of\ free\ PTX)}\ x\ 100 \qquad (ß4.4)$$

Samples were prepared as described above and the EE for the three batches was (98 ± 1) % (Mean ± SD), as shown in the Figure bellow.

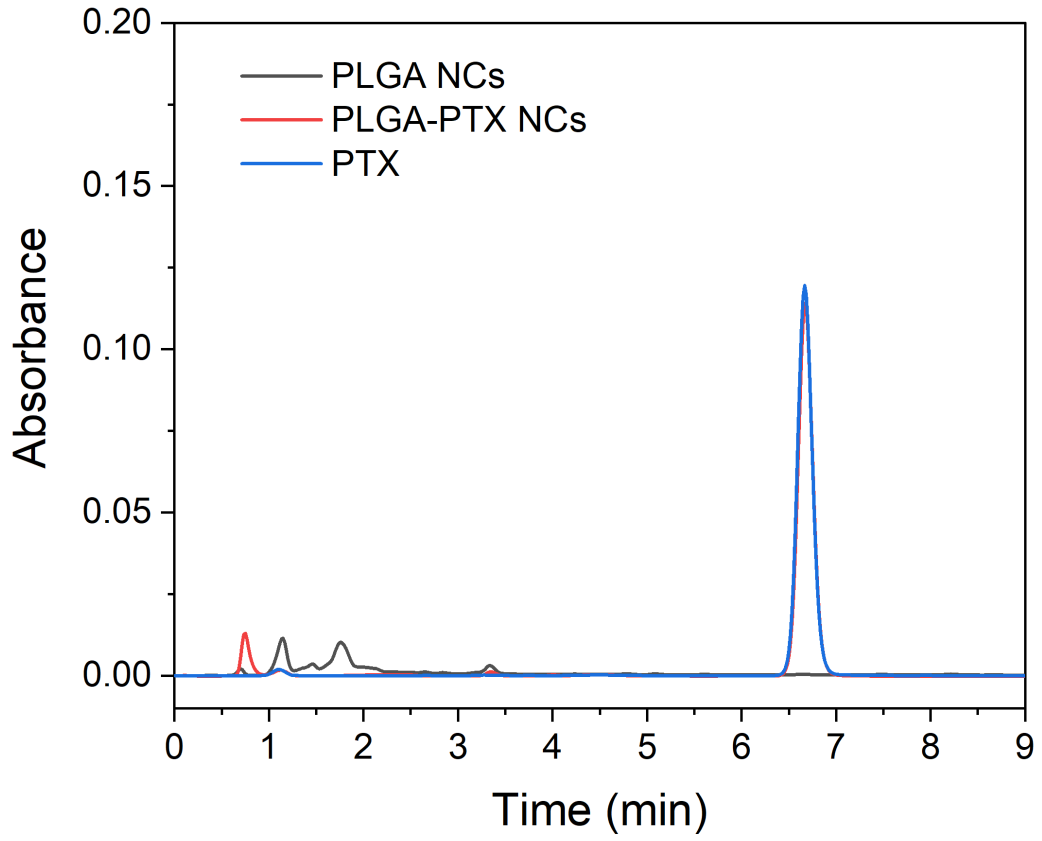

Figure S4.1 - Chromatograms to determine encapsulation efficiency of paclitaxel in PLGA NCs.

Source: By the author.

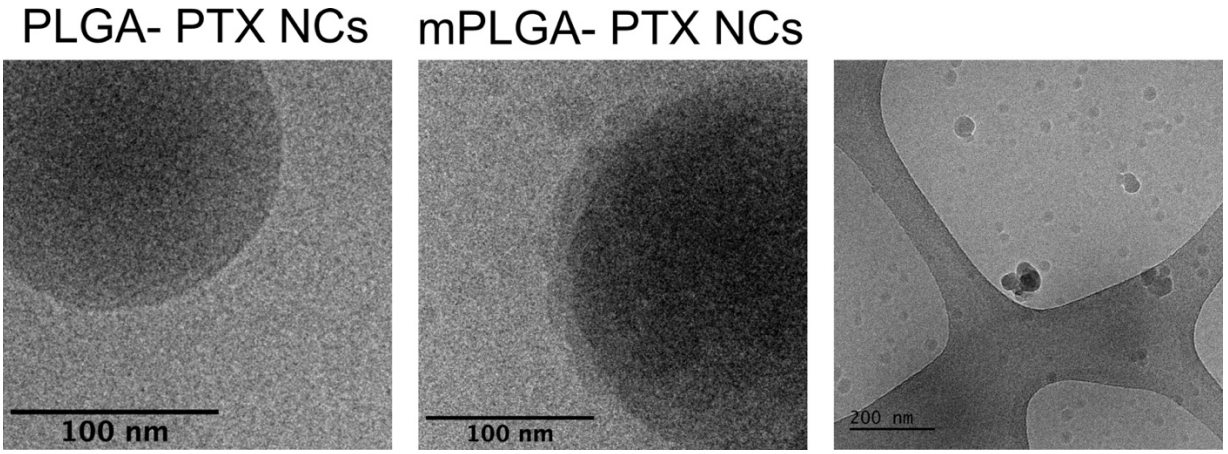

Figure S4.2 - Cryo-TEM images that was able to observe the irregular coating with cell membrane. The last image we observe the ice formation on the grid.

Source: By the author.

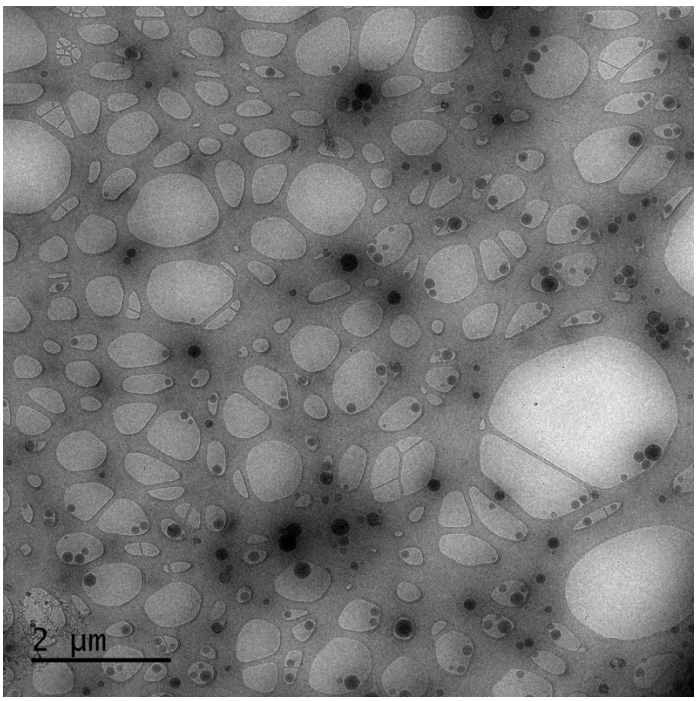

Figure S4.3 - Cryo-TEM image of PLGA-PTX NCs.

Source: By the author.